Conjugated Polymers Having Indolin-2-one Side Chains for Organic Electronics

by

Wuqi Li

A thesis

presented to the University of Waterloo

in fulfillment of the

thesis requirement for the degree of

Master of Applied Science

in

Chemical Engineering (Nanotechnology)

Waterloo, Ontario, Canada, 2021

Author's Declaration

I hereby declare that I am the sole author of this thesis. This is a true copy of the thesis, including any required final revisions, as accepted by my examiners.

I understand that my thesis may be made electronically available to the public.

Abstract

It is of great significance to develop π-conjugated semiconducting polymers for various kinds of printed organic electronics applications such as organic solar cells (OSCs) and organic field-effect transistors (OFETs). Solar energy has been regarded as crucial clean and sustainable energy resources to address the growing worldwide energy crisis and replace traditional fossil fuels to reduce the carbon emission and protect the environment. OSCs or organic photovoltaics (OPVs) that can directly convert sunlight to electricity, have shown be advantageous due to their light weight, low cost and high potential to manufacture devices with large area by solution-processable printing technologies. Recently, it has been reported that many OSCs comprised of non-fullerene acceptors (NFAs) and wide-bandgap donor polymers (WBGs) have achieved high power conversion efficiency (PCE) of over 17%. Nevertheless, there are still some issues that hinder the commercialization of OSCs. The high synthetic cost of organic semiconductor materials and the use of toxic processing solvents are problems to be solved urgently.

Indolin-2-one is a well-known π-conjugated building block, which is found in natural dyes and pigments such as indigo dye and Tyrian Purple. Recently, indolin-2-one has been used as an electron withdrawing or accepting moiety in numerous high performance polymer semiconductors for OSCs and OFETs. In this work, a series of Type II donor-acceptor polymers with electron donor backbone comprised of benzo[1,2-b:4,5-b’] dithiophene (BDT) and thiophene and electron acceptor side chains made of indolin-2-one were developed for OPVs and OFETs. Specifically, PTIBDT and its fluorinated counterpart PTIFBDT were synthesized via the Stille-coupling polymerization method, which have wide optical bandgaps around 1.9 eV, thereby achieving complementary light harvesting with an NFA material ITIC. Both polymers have a low-lying highest occupied molecular orbital (HOMO) energy level of ca. -5.6 eV, which may help achieve

high open circuit voltage (V_{oc}). As the channel semiconductor in OFETs, PTIBDT and PTIFBDT exhibited hole mobilities up to 0.0044 $cm^2V^{-1}s^{-1}$ and 0.0026 $cm^2V^{-1}s^{-1}$, respectively. When PTIBDT and PTIFBDT were used as donors with ITIC as the acceptor in OSCs, high PCEs up to 8% and 7.70% were achieved, respectively. The high PCEs were largely contributed by their high V_{oc} of 0.97 and 1.0 V, respectively, due to their very deep HOMO levels. On the other hand, the current density (J_{sc}) and fill factor (FF) of devices based on the PTIBDT:ITIC and PTIFBDT:ITIC blends were relatively low, which might be partially related to the hole trapping by the electron-rich nitrogen atom in the indolin-2-one unit. This is evidenced by the very large threshold voltage (V_{th}) of ca. -30 V, which indicates the existence of massive hole traps in both polymers. Substitution at the 5-position of indolin-2-one with the electron-withdrawing fluorine atom in PTIFBDT in order to decrease the electron density of the nitrogen atom appeared to have little effect on reducing the V_{th} or the number of hole traps in the OFETs based on PTIFBDT compared with PTIBDT. Therefore, strong electron-withdrawing acetyl and propionyl substituents were directly introduced to the nitrogen atom in the indolin-2-one unit to exert a stronger effect on lowering the electron density of the nitrogen and reducing the hole traps. The resulting two polymers, PTIABDT (having acetyl substituents) and PTIPBDT (having propionyl substituents) showed similar HOMO energy levels, but lower lowest unoccupied molecular orbital (LUMO) energy levels, leading to narrowed bandgaps of 1.83 eV and 1.84 eV, respectively. The reduced LUMO energy levels indicate a significant electron withdrawing effect of the acetyl and propionyl substituents on the overall reduction of the electron density of the nitrogen atom and the indolin-2-one side chain. As expected, OFETs based on PTIABDT exhibited very small V_{th} (less than 2 V), indicating that the number of hole traps in this polymer has been greatly reduced. The devices also showed much increased hole mobility of up to 0.015 $cm^2V^{-1}s^{-1}$. Surprisingly, OFETs based

on PTIPBDT did not show a reduction in V_{th} in comparison with PTIBDT (having methyl substituents). Thermal gravimetric analysis (TGA) of PTIPBDT revealed that the propionyl groups are thermally unstable, which started to decompose at ca. 100 °C. Since this polymer was synthesized at 90 °C for 18 hrs, some of the propionyl groups might be lost during the polymerization process. The nitrogen atoms without the propionyl substituents would act as hole traps, which might explain the large V_{th} and rather low hole mobility of 0.007 $cm^2V^{-1}s^{-1}$ compared with PTIABDT. Although the OFET performance was improved, OSCs based on PTIABDT:ITIC and PTPBDT:ITIC showed low J_{sc} and FF, resulting in rather low PCEs of 3.99% and 3.29%, respectively. Replacing ITIC with IT-4F, the OSCs based on PTIABDT:IT-4F showed a slight improvement in PCE of up to 4.48%. The poor OSC performance for both polymers might be due to the low crystallinity of polymers and poor morphology of the polymer blends.

Lastly, a water-soluble conjugated polymer based on isoindigo (ID), PIDBT, has been developed to avoid the use of toxic halogenated solvents for processing the OSCs and OFETs. It was found that introduction of butyl sulfonate group on ID could make ID monomer and the resulting PIDBT polymer water-soluble, which has the potential for fabricating OSCs and OFETs using water as the processing solvent.

Acknowledgements

I would like to show my great thanks to my supervisor, Prof. Yuning Li, for his very patient and responsible guidance on my research work. He guided me to begin my research study in very high-quality standard and always offered me valuable advice to help me push forward the research work. In addition, he also helped me a lot to improve my efficiency and the ability to get the work well planned and organized which is for sure worthy leaning process for my whole future career. In addition, it is also my great honor to invite Prof. Xianshe Feng and Prof. Michael Pope as my committee members to review my thesis, and they provided me valuable advices to improve this thesis.

I would also show my great thanks to NSERC Green Electronics Network (GReEN) for providing funding to support my research.

I am very grateful to Jenner H. L. Ngai and Dr. Arthur D Hendsbee for teaching me all laboratory skills that I require. I am also very thankful to Dr. Marwa Abd-Ellah for her wonderful organic solar cells (OSCs) characterization work and fantastic results. Special thanks to Pankaj Kumar, Xiguang Gao and Yi Yuan for their kind help to measure XRD, TGA, and DSC. I would also show many thanks to Haitao Liu and Dr. Xu Li who work in the Institute of Chemistry of Henan Academy of Sciences in China for their great help to measure HT-NMR and GPC. Additionally, I would also thank Zhifang Zhang, Zhaoyi Yin, Keqiang He, who helped me a lot during my research work. Moreover, I would like to show my thanks to all other members in our group, and I always feel honored to be part of this research group.

Finally, I would like to thank my family and friends for their encouragement full of love during this time.

Table of Contents

Author's Declaration ii
Abstract iii
Acknowledgements vi
List of Figures ix
List of Tables xiv
List of Abbreviations and Symbols xv
Chapter 1 Introduction 1
1.1 Overview of Organic Solar Cell 1
1.2 Working Principles of Organic Solar Cell 5
1.3 Non-fullerene Organic Solar Cell 8
1.4 Wide-bandgap Donor Polymers 11
1.5 Green-solvent-processable Materials for Organic Electronics 13
1.6 Characterization of Polymers 15
1.7 Objective and Structure of Thesis 18
Chapter 2 Synthesis and Characterization of PTIBDT and PTIFBDT Polymers 20
2.1 Introduction 20
2.2 Structure Simulation by Density Functional Theory (DFT) 23
2.3 Synthesis of Monomers and Polymers 25
2.4 Characterization of PTIBDT and PTIABDT 29
2.4.1 Physical Properties (GPC, TGA and DSC) 29
2.4.2 Optical and Electrochemical Properties (UV-vis and CV) 30
2.4.3 Organic Field-effect Transistor (OFET) Performances 34
2.5 Organic Photovoltaic (OPV) Performances 37
2.6 Summary and Future directions 48
2.7 Experimental Section 49
Chapter 3 Synthesis and Characterization of PTIABDT and PTIPBDT 56
3.1 Introduction 56
3.2 Structure Simulation by Density Functional Theory (DFT) 58
3.3 Synthesis of Monomers and Polymers 59

3.4 Characterization of Polymers 62
3.4.1 Physical Properties (GPC, TGA and DSC) 62
3.4.2 Optical and Electrochemical Properties (UV-vis and CV) 64
3.4.3 Organic Field-effect Transistor (OFET) Properties 67
3.5 Photovoltaic properties of PTIABDT and PTIPBDT 69
3.6 Summary and Future directions 79
3.7 Experimental section 80
Chapter 4 Design and Synthesis of Water-soluble Polymer Based on Isoindigo 85
4.1 Introduction 85
4.2 Synthesis of Monomer and Polymer 87
4.3 Summary and Future Directions 92
4.4 Experimental Section 93
Chapter 5 Summary and Future Directions 96
Bibliography 99
Appendix 118

List of Figures

Figure 1-1 Bilayer **(a)** and bulk **(b)** heterojunction of organic solar cell.[7] 2

Figure 1-2 Diagram of the structure of a typical bulk heterojunction organic solar cell. [12] 3

Figure 1-3 Schemic illustration of a conventional and inverted architecture of bulk heterojunction (BHJ) organic solar cell. [17] 4

Figure 1-4 Operation mechanism of OSC device **a**, BHJ solar cell structure **b**, (1) exciton generation; (2) exciton diffusion; (3) exciton dissociation; (4) transport of free carriers; (5) collection of free carriers at electrodes. [20] 6

Figure 1-5 Current-voltage (J-V) curve of OSC device. [3] 8

Figure 1-6 Chemical structures of C_{60} and $PC_{61}BM$. [10] 9

Figure 1-7 Chemical structures of non-fullerene acceptors. [17,36] 11

Figure 1-8 Chemical structures of BDT and PT based WBG polymers. [32] 12

Figure 1-9 Diagram of some halogenated solvents and different categories of green solvents. [48] 14

Figure 1-10 Diagram of green-solvent-processable conjugated polymers with some commonly used functional groups and side chains. [48] 15

Figure 2-1 Structures of Type I and Type II D-A polymers. [66] 20

Figure 2-2 (a) Structures and **(b)** energy levels alignment of PTIBT and ITIC **(c)** Structures of PTIBDT and PTIFBDT..... 21

Figure 2-3 Optimized geometries of PTIBDT and PTIFBDT and predicted energy levels in different configurations..... 24

Figure 2-4 Synthesis route of PTIBDT and PTIFBDT. 25

Figure 2-5 ^{1}H NMR of monomer of PTIBDT **(a)** and PTIFBDT **(b)**. 26

Figure 2-6 ^{1}H NMR spectra of M1**(a)**, and M2 **(b)** as-prepared (black) and heated at 90 ℃ for 22 hrs in chlorobenzene (red) in CDCl3. 27

Figure 2-7 ^{1}H NMR spectra of PTIBDT**(a)**, PTIFBDT **(b)** in 1,1,2,2-tetrachloroethane which was measured at 90℃. 28

Figure 2-8 High temperature GPC molecular weight distribution for **(a)** PTIBDT, and **(b)** PTIFBDT, measured using 1,2,4-trichlorobenzne as eluent at 110 ℃ with a flow rate of 1.00 $mLmin^{-1}$ 29

Figure 2-9 TGA **(a)** and DSC **(b)** curves of PTIBDT and PTIFBDT. 30

Figure 2-10 UV-vis spectra of PTIBDT, PTIFBDT and ITIC **(a)** in chloroform and **(b)** as spin-coated films at room temperature. 32

Figure 2-11 Cyclic voltammetry profiles of PTIBDT and PTIFBDT acquired in tetrabutylammonium hexafluorophosphate solution (0.1M) dissolved in acetonitrile at a scan rate of 0.1V/s. 34

Figure 2-12 Configuration of a bottom-gate bottom-contact (BGBC) organic field-effect transistor (OFET). 35

Figure 2-13 Transfer and output curves of PTIBDT annealed at 150℃ [**(a)** and **(c)**] and PTIFBDT annealed at 100℃ [**(b)** and **(d)**]. 35

Figure 2-14 Photoluminescence spectra of **(a)** PTIBDT neat film and blend film of PTIBDT: ITIC, **(b)** PTIFBDT neat film and PTIFBDT: ITIC when excitation wavelength is 500nm. 38

Figure 2-15 Photoluminescence spectra of neat film of ITIC and blend films of PTIBDT: ITIC, PTIFBDT: ITIC when excitation wavelength is 707nm. 39

Figure 2-16 (a) Illustration of inverted OSC device structure, and **(b)** energy levels for PTIBDT, PTIFBDT and ITIC. 40

Figure 2-17 (a) Current density-voltage (J-V) curves of OSCs, **(b)** External quantum efficiencies of PTIBDT:ITIC and PTIFBDT:ITIC blends. 42

Figure 2-18 Schematic of hole-only device **(a)** and electron-only device **(b)** for SCLC measurement.[89] 44

Figure 2-19 Current density-voltage (J-V) curves of **(a)** hole-only device and **(b)** electron-only device of PTIBDT and PTIFBDT. 45

Figure 2-20 AFM height [(**a**) and (**b**)] and phase [(**c**) and (**d**)] images of PTIBDT:ITIC and PTIFBDT:ITIC blend films. 46

Figure 2-21 (a) Out of plane line cutting of GIXD patterns and **(b)** images of PTIBDT and PTIFBDT films. 47

Figure 3-1 Structures of Type I, Type II D-A copolymer and PTIABDT, PTIPBDT polymer. . 56

Figure 3-2 Structures of TT-C, PBDTTT-C and PBDTTT-C-T. 57

Figure 3-3 Optimized geometries of PTIABDT and PTIPBDT and predicted energy levels in different configurations. 58

Figure 3-4 The synthetic routes to PTIABDT and PTIPBDT. 60

Figure 3-5 ^{1}H-NMR spectra of monomer of PTIABDT **(a)** PTIPBDT **(b)**. 62

Figure 3-6 High temperature GPC molecular weight distribution for (**a**) PTIABDT measured using 1,2,4-trichlorobenzne as eluent at 110 °C with a flow rate of 1.00 mLmin^{-1} and (**b**) PTIPBDT measured using chloroform as eluent at room temperature. 62

Figure 3-7 TGA **(a)** and DSC **(b, c)** curves of PTIABDT and PTIPBDT. 63

Figure 3-8 UV-vis spectra of **(a)** PTIABDT (in chlorobenzene solution and as-cast thin film at RT) and ITIC (as-cast film) **and** 65

Figure 3-9 Cyclic voltammetry profiles of PTIBDT and PTIFBDT in tetrabutylammonium hexafluorophosphate acetonitrile solution (0.1M) at a scan rate of 0.1V s^{-1}. 66

Figure 3-10 Transfer and output curves of PTIABDT annealed at 50℃ **(a, c)**, and PTIPBDT annealed at 150℃ **(b, d)**. 68

Figure 3-11(a) and (c) Photoluminescence spectra of neat films of PTIABDT, PTIPBDT and blend films of PTIBDT: ITIC, PTIFBDT: ITIC when excitation wavelength is 500nm. **(b) and (d)** neat film of ITIC and blend films of PTIBDT: ITIC, PTIFBDT: ITIC when excitation wavelength is 707nm. 70

Figure 3-12 (a) Schematic of inverted device structure for OSCs and **(b)** chemical structures of ITIC and IT-4F. 71

Figure 3-13 Current density-voltage (J-V) curves of OSCs of active layers of PTIABDT:ITIC and PTIPBDT:ITIC at room temperature. 72

Figure 3-14 74

Figure 3-15 AFM height **(a)** and phase **(c)** images of PTIABDT:ITIC blend film, and height **(b)** and phase **(d)** of PTIPBDT:ITIC blend film. 75

Figure 3-16 (a) Photoluminescence spectra of neat films of PTIABDT and blend films of PTIABDT: IT-4F when excitation wavelength is 500nm, **(b)** neat film of IT-4F and blend films of PTIABDT: IT-4F when excitation wavelength is 707nm, and **(c)** current density-voltage (J-V) curves of OSCs of active layers of PTIABDT:IT-4F. 77

Figure 3-17 AFM height **(a)** and phase **(b)** images of PTIABDT:IT-4F blend film. 78

Figure 4-1 Chemical structures of different CPEs. [48] 85

Figure 4-2 Chemical structures of isoindigo (ID) and CPE PIDBT. 86

Figure 4-3 Chemical structures of cationic and anionic ID. 88

Figure 4-4 Synthetic route 1: direct Stille-coupling polymerization with ID-Br_2-K. 89

Figure 4-5 Synthetic route 2: Stille-coupling polymerization with precursor ID-Br_2-PPh_4. 91

List of Tables

Table 2-1 Molecular weight and thermal properties of PTIBDT and PTIFBDT 30

Table 2-2 Optical and electrochemical properties of PTIBDT and PTIABDT 31

Table 2-3 BGBC OFET performances of PTIBDT and PTIFBDT at different annealing temperatures 37

Table 2-4 Summary of OSC devices performance of PTIBDT:ITIC and PTIFBDT:ITIC 41

Table 3-1 Molecular weight and thermal properties of PTIABDT and PTIPBDT 64

Table 3-2 Optical and electrochemical properties of PTIBDT and PTIABDT 64

Table 3-3 BGBC OFET performances of PTIABDT and PTIPBDT at different annealing temperatures 69

Table 3-4 Summary of OSC devices performance of PTIABDT:ITIC and PTIPBDT:ITIC 72

Table 3-5 Summary of OSC devices performance of PTIABDT:IT-4F 78

List of Abbreviations and Symbols

AFM: atomic force microscopy

BGBC: bottom gate bottom contact

CV: cyclic voltammetry

D-A: donor-acceptor

DSC: differential scanning calorimetry

FF: fill factor

GPC: gel-permeation chromatography

HOMO: highest occupied molecular orbital

I_{ON}/I_{OFF}: current ON/OFF ratio

J_{sc}: short-circuit current density

LUMO: lowest unoccupied molecular orbital

NMR: nuclear magnetic resonance

OFET: organic field effect transistor

OPV: organic photovoltaic

OSC: organic solar cell

PCE: power conversion efficiency

RMS: root mean square

TGA: thermogravimetric analysis

UV-vis: ultraviolet-visible

V_{oc}: open-circuit voltage

V_{th}: threshold voltage

μ: charge carrier mobility

XRD: X-ray diffraction

Other abbreviations and symbols are defined in the text.

Chapter 1 Introduction

1.1 Overview of Organic Solar Cell

Facing the worldwide growing energy crisis, it is of great significance to develop clean and sustainable energy sources so that the traditional fossil fuels can be replaced, and more and more attention has been focused on the usage of solar energy in order to address today's energy crisis and protect the environment. [1] Photovoltaic technology involves the capability to directly convert the sunlight into the electricity via suitable semiconducting materials. [2] Among the commercially available photovoltaic devices, silicon-based solar cells still dominate this field. Nevertheless, the high cost of silicon solar cells has limited the wide application and further commercialization of this kind of devices. Organic solar cells (OSCs) which are considered as the representative of third-generation solar cells have been investigated to be highly promising for future energy resources due to the advantages such as the light weight and easy fabrication with low cost materials. [3] Additionally, OSCs make it possible to manipulate scalable large-area devices with low cost using solution-processing printing methods.[2,4,5]

Currently, the most effective OSC devices adopt the bulk heterojunction (BHJ) architecture as illustrated in **Figure 1-1 (b)** which involves a blend film of an electron-rich donor material and an electron-deficient acceptor material with nanoscale phase separation. At the initial stage of OSCs' exploration, Tang introduced the double layers containing donor and acceptor split layers which mean a bilayer heterojunction architecture as indicated in **Figure 1-1 (a)**.[6] This simple bilayer heterojunction has been reported widely applied in small molecule solar cells,[7] and a PCE of 4% has been obtained in copper phthalocyanine and C_{60} OSC device in the bilayer configuration. [8] Nevertheless, the power conversion efficiency (PCE) in this bilayer structure is limited because the efficient charge separation can only be achieved at the donor-acceptor interface area, and thus

only excitons within a short distance of 10-20nm away can diffuse to the interface causing the loss of photon absorption. [9,10] As a result, the BHJ configuration was later developed which has been considered as the most ideal photovoltaic structure for OSC devices to overcome the primary issue caused by the bilayer structure due to the short length of exciton diffusion which seriously restricts the thickness of active layer. [11] The BHJ architecture can form a bicontinuous interpenetrating network achieving preferred separated phase state between donor and acceptor in nanoscale. Unlike the bilayer structure where the donor and the acceptor phase are thoroughly split away, the two phases are intimately intermixed,[10] so the name "bulk heterojunction" is assigned because a D/A interface can be reached within a few nanometers at any point in donor-acceptor composite.[9] This configuration consequently increases the D/A interfacial areas for the excitons, which mean the electron-hole pairs that are produced after absorption of photons, to dissociate because the required traveling distance for excitons to the D/A interface will be reduced. Consequently, the exciton dissociation at the D/A interface will be very efficient to generate enough free carriers and hence large charge photocurrent generation. [11,12] In addition, the photovoltaic effect which involves the conversion between photon energy and electrical energy can also be enhanced since the BHJ structure improves the charge collection at the electrode via providing charge transport pathways.

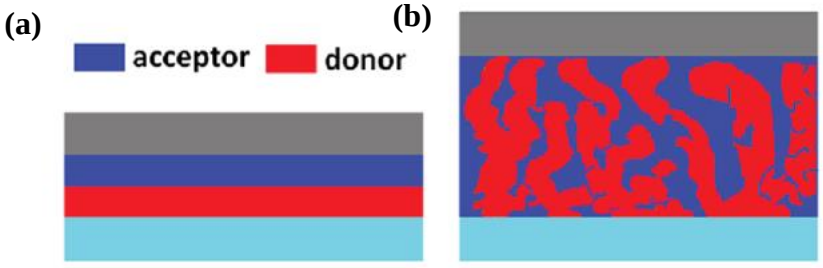

Figure 1-1 Bilayer **(a)** and bulk **(b)** heterojunction of organic solar cell.[7]

The D/A composite in BHJ solar cell can be prepared by solution processing technology which makes it possible to fabricate OSC devices with large area of active layer in large scale and low cost. [13] In such a BHJ solar cell, the D/A blend is typically packed between a transparent anode which is indium-tin-oxide (ITO) in most cases and a cathode which is typically metal. Like shown in **Figure 1-2**, a representative scheme is presented, where a poly(3,4-ethylenedioxythiophene)-poly(styrenesulfonate) (PEDOT:PSS) layer is introduced as the hole transport facilitating layer so that the contact between anode (ITO glass) and active D/A blend layer is improved. [12] Indeed, such OSC device structure is known as conventional BHJ device (**Figure 1-3**), and sometimes an electron transport layer is also introduced often utilizing TiO_x, $CsCO_3$ and LiF. The metal electrode includes a metal with low work function like calcium and aluminum. The main limitation of conventional OSC device arises from the easy conversion of low work function metal to insulating oxides so that the performance of the OSC degrades rapidly.[14] In order to settle this issue, it is necessary to encapsule the OSC device with expensive packing materials to prevent the exposure to water and oxygen.

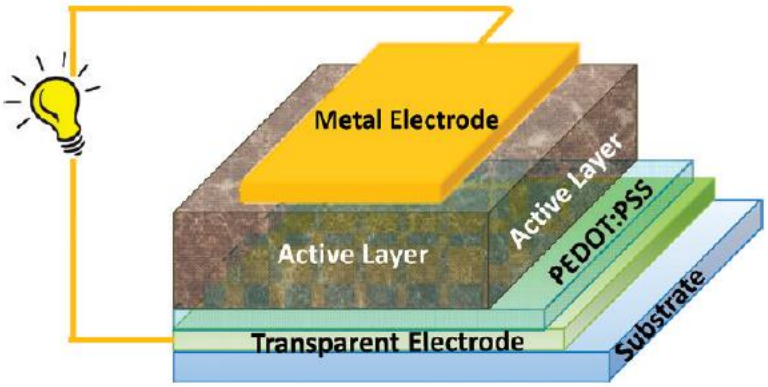

Figure 1-2 Diagram of the structure of a typical bulk heterojunction organic solar cell. [12]

Inverted BHJ organic solar cell configuration (**Figure 1-3**) was developed to improve the device performance via reducing the active layer degradation and increasing the interface stability.[15] The

term “inverted” describes an opposite layer sequence and thus opposite direction of the flow of charges.[15] OSC with inverted structure can be fabricated on rigid glass or flexible plastic substrate which is coated with the transparent ITO as cathode whereas the ITO is used as anode in the conventional BHJ devices. An electron transport layer utilizes oxides including TiO_x and ZnO in the inverted structure in an opposite position of this layer in the conventional device. Similarly with the commonly used PEDOT:PSS as the hole facilitating transport layer in the conventional architecture of OSC, the materials used for this layer involve p-type oxides, MnO_3, V_2O_5, and PEDOT:PSS etc.[16] Moreover, a metal with high work-function such as gold and silver is introduced as the anode in the inverted BHJ device, and this very air-stable metal enhances the stability of the device. Consequently, the inverted device exhibits much better environmental stability under ambient condition mainly due to the removal of unstable low work-function metal as well as substituted usage of PEDOT:PSS in the hole transport layer which affects the stability of the OSC device because of the acidic nature.[15] Additionally, the Ohmic contacts get improved in the inverted architecture leading to enhanced collection of photo-generated charges and therefore better photovoltaic performance.[15] So far, the most efficient BHJ solar cell devices have been reported to adopt the inverted architecture.

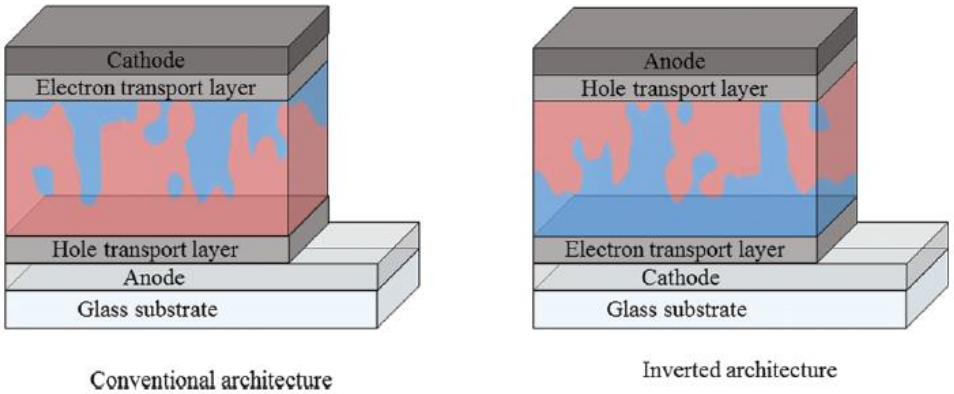

Figure 1-3 Schemic illustration of a conventional and inverted architecture of bulk heterojunction (BHJ) organic solar cell. [17]

1.2 Working Principles of Organic Solar Cell

The operation process of an OSC device can be explained step by step as illustrated in Figure **1-4**:

(1) When light irradiates the active layer which is a D/A composite, other donor (channel 1) or acceptor (channel 2) will absorb photons to generate excitons that refer to coulombically binding electron-hole pairs.

(2) The excitons can subsequently diffuse to the D/A interfacial areas and then separate or dissociate to free carriers including free holes and free electrons. The dissociation driving force is provided by the energy level difference or offset between donor and acceptor material, so that is LUMO level offset determining electron transport and HOMO level offset determining hole transport.

(3) After the dissociation of excitons, there will be transport of free electrons from donor to acceptor through LUMO level driven by the LUMO energy offset in channel 1and further transport in the D/A interpenetrating network. Similarly with free electrons, the free holes produced in channel 2 will be transferred from the acceptor to donor through HOMO level driven by the HOMO energy offset and then continue the drift in the donor domains.

(4) The free charges are finally collected by the cathode and anode electrodes to produce photocurrent. [3,4,10,18,19]

The key factor for efficient exciton dissociation is to maintain the comparable magnitude between the exciton diffusion length and D/A separation phase length. Otherwise, the power conversion efficiency will be lowered as a result of the loss of excitons via radiative or nonradiative recombination before reaching D/A interface. [10]

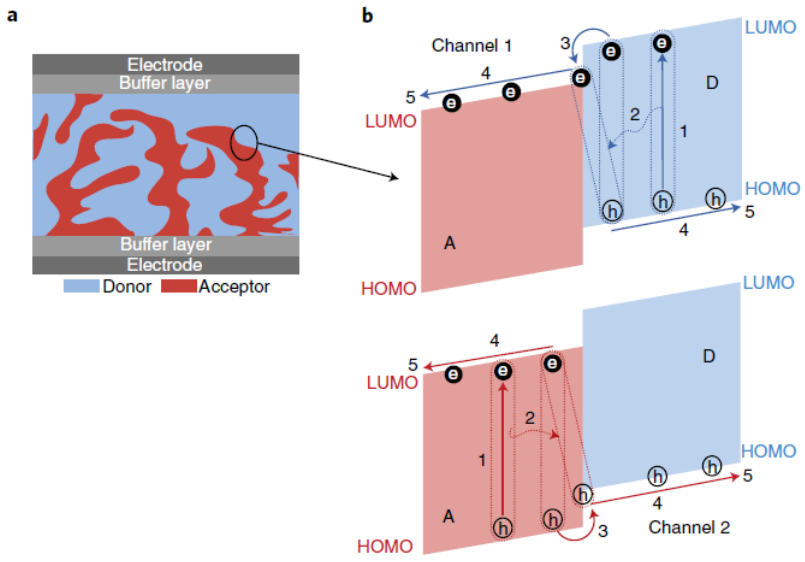

Figure 1-4 Operation mechanism of OSC device **a**, BHJ solar cell structure **b**, (1) exciton generation; (2) exciton diffusion; (3) exciton dissociation; (4) transport of free carriers; (5) collection of free carriers at electrodes. [20]

A representative current density versus voltage (J-V) curve of OSC device under light illumination which is normally AM 1.5G 100Mw/cm^2 is showed in **Figure 1-5**. Three critical parameters involving short circuit current density (J_{sc}), fill factor (FF) and open circuit voltage (V_{oc}) are illustrated in this figure. J_m and V_m stand for the "current density" and "voltage" when the power reaches the maximum value meaning the maximum point of J×V. The power conversion efficiency (PCE) is defined by Equation 1:

$$PCE = \frac{J_{SC} \times V_{OC} \times FF}{P_{in}} \qquad (1)$$

P_{in} in the equation means the total incident light input power. According to this equation, the PCE should be proportional to the values of J_{sc}, V_{oc}, and FF, and all these values should be maximized in order to maximize the PCE.

Generally speaking, J_{sc} stands for the highest current density that can be achieved for the OSC device, and this value can be affected by several factors that are related to photocarriers generation:

photons absorption ability of the active D/A blend film, excitons dissociation efficiency at D/A interfacial areas, transport of free carriers in donor and acceptor counterparts and the charge collection efficiency at electrodes. [3] For the active layer with fixed light absorption profile, the limitation of J_{sc} is the charge carriers mobilities depending on the material nature and the nanoscale morphology of the thin film which is very difficult to control and optimize. [10]

In OSC devices, the values of V_{oc} are reported to be proportionally related with the energy level offset between the HOMO level of the donor and LUMO level of the acceptor. Under the open circuit conditions, the accumulation of photo-generated free carriers on the electrodes causes a potential difference without current flow, and this potential difference between anode and cathode is V_{oc}, also the maximum voltage the OSC device can afford. [21] To quantize this parameter, Scharber [22] introduced one invaluable equation:

$$V_{OC} = \frac{1}{e}\,(E_g - 0.3V) \qquad (2)$$

In this Equation 2, E_g represents the lowest optical bandgap between donor and acceptor materials. Many OPV systems have been investigated to estimate the empirical value of energy loss, 0.3eV as shown in Equation 2, which should be due to the disorder of phase separation of donor and acceptor domains resulting in restricted transport of charge carriers. [21,23]

Fill factor is defined by the ratio between the power at maximum point ($J_M \times V_M$) and the value of $J_{sc} \times V_{oc}$ as shown by Equation 3:

$$FF = \frac{J_M \times V_M}{J_{SC} \times V_{OC}} \qquad (3)$$

This value is determined by the effective charge carriers collected by the electrodes. There is indeed possibility for free carriers to be recombined or extracted by the electrodes. Hence, the lifetime and mobility of free carriers should be enhanced to increase the drifting length of the

charge carriers so that they are able to reach the electrodes. [10] Simultaneously, the series and parallel resistances also have a great impact on the FF values which should be minimized. [3]

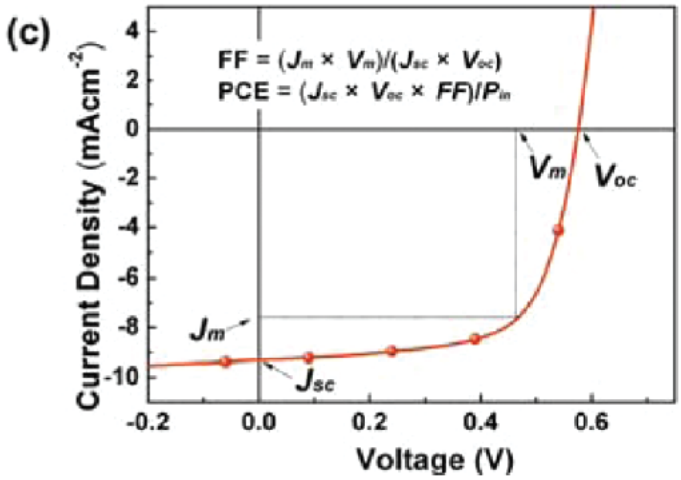

Figure 1-5 Current-voltage (J-V) curve of OSC device. [3]

1.3 Non-fullerene Organic Solar Cell

One typical OSC device is comprised of a pair of matching materials with the function as electron-donating and -accepting part, respectively. [5] For the acceptor counterpart, fullerene derivatives have long dominated to be used as electron accepting materials in the past decades. [17] Due to the poor solubility of the original fullerenes including C_{60} in organic solvents, solubilizing groups are introduced to fullerenes to produce the most commonly used fullerene derivative, [6,6]-phenyl-C_{61}-butytic acid methyl ester ($PC_{61}BM$) as shown in **Figure 1-6**. [24] In addition, $PC_{71}BM$ which is an analogue of C_{70} instead of C_{60} has been developed to enhance PCE as a result of its enhanced light absorption range in the visible region. [25] PCBM has shown several advantages to be applied in highly efficient OSCs involving high electron mobility as well as affinity, three-dimensional structure with unique packing ability and good miscibility with conjugated polymers to function as efficient electron transport channel in the D-A blend in combination with low-bandgap polymers as electron donor. [7,26] Currently, BHJ OSC devices based on donor polymers and fullerene

acceptors have been reported to achieve a PCE exceeding 11%. [27] Nevertheless, the donor polymers and PCBM system exhibits several drawbacks which ultimately restrict the further improvement of PCE. Firstly, PCBM typically shows low photons absorption in the visible as well as near-infrared (NIR) light region due to the highly symmetrical structure resulting in low contribution of acceptors to the photocurrent generation. [17,28] Secondly, the opportunity to tune the bandgap of the fullerene derivatives is restricted to maintain the intact structure of C_{60} or C_{70} core with limited possibilities of structure modification. Thirdly, the spherical structure of PCBM makes it very easy to crystalize and aggregate destroying the stability of the OSC device. [29,30] Lastly, PCBM based OSC device has been reported to yield large V_{oc} loss as a consequence of its non-sharp absorption edge. [20]

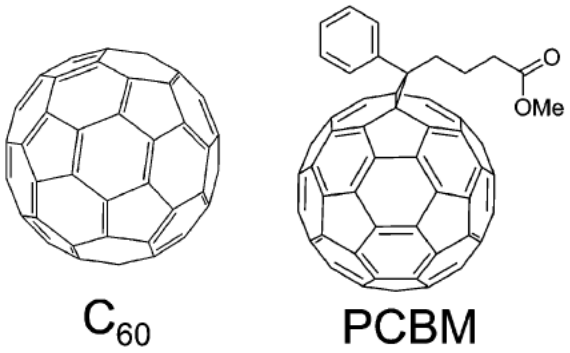

Figure 1-6 Chemical structures of C_{60} and $PC_{61}BM$. [10]

In the last few years, small molecule non-fullerene acceptors (NFAs) have attracted more and more research attention to replace fullerene acceptors leading to significant enhancement in PCE of OSC devices. [31] The NFAs with high synthetic complexity have shown distinct advantages including broadened absorption in visible including near-infrared (NIR) region due to their tunable bandgaps

and tunable energy levels which contribute to suitable energy levels alignment between donor and acceptor materials to obtain high V_{oc} and low energy loss. [20,32] The fully conjugated structure of NFAs strongly facilitates electron accepting and isotropic electron transporting ability as well as electron delocalization at D/A interfaces. [33] With the rapid progress of structure design of NFAs, the NFA based OSC devices have achieved a PCE exceeding 16% in single junction devices and 17% in tandem structure showing the high potential of NFAs for future generation of OSCs. [31,34] Several model small molecule NFAs have been considered as the benchmark for NFA based OSCs development as shown in **Figure 1-7**. One of the most frequently investigated NFAs, ITIC, was discovered in 2015 representing a remarkable step forward for exploration of NFAs. [35] ITIC contains an indacenodithiophene (IDT) electron-donating core and 2-(3-oxo-2,3-dihydroinden-1-ylidene) malononitrile (INCN) electron-accepting ending group to form an A-D-A push-pull NFA which favors intramolecular charge transfer (ICT) and exhibits high hole mobility as well as broad absorption attributed to the coplanar structure. [20,36] ITIC has been successfully matched with various donor polymers yielding PCE exceeding 13%. [37] Structural modifications on ITIC lead to a series of derivatives such as ITIC-Th [38] with thienyl alkyl chains substitution and IT-4F [39] with fluorination substitution. The PCE is further enhanced to over 14% when IT-4F is used as acceptor. Very recently, Yuan et al. has introduced one highly promising NFA with the name of Y6, and when PM6 is used as the wide bandgap donor polymer, the OSC device with PM6:Y6 system exhibits a high PCE up to 16%. [40] In this thesis, the model NFA ITIC will be used as the acceptor owing to its high availability and miscibility with different donor polymers developed in this thesis.

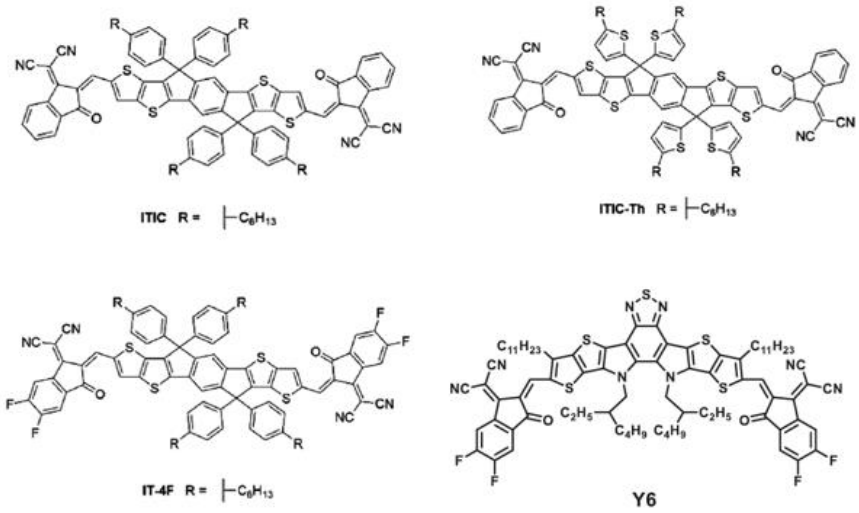

Figure 1-7 Chemical structures of non-fullerene acceptors. [17,36]

1.4 Wide-bandgap Donor Polymers

The choice of donor materials to properly match with the acceptors shows great effect on determining the performance of resulting OSC devices. The donor polymers can be classified into three categories according to their optical bandgap (E_g^{opt}): low-bandgap (LBG) polymers with E_g^{opt} < 1.6eV, medium-bandgap (MBG) polymers with 1.6eV < E_g^{opt} < 1.8eV and wide-bandgap (WBG) polymers with E_g^{opt} > 1.8eV. [1] In the early stage, LBG and WBG donor polymers with broad light absorption range have dominated the filed of OSC applications at the aim to match with fullerene-based acceptors which show limited light absorption. On the contrary, less attention has been attracted to the development of WBG polymers due to the limitation on visible light absorption and low photocurrent output. [27,32] However, the rapid development of efficient near-infrared NFAs makes it possible to achieve complementary light absorption with WBG polymers thus covering the full range of visible light absorption. Additionally, the usage of WBG polymers with deep HOMO levels can effectively increase the V_{oc} and hence decrease the energy loss in NFA-based

OSC devices. [32] Consequently, the pattern of NFAs paired with WBG donor polymers has been reported to generate the most efficient OSCs up to date indicating the great significance for the development of new designs of WBG donor polymers.

Rapid progress on the development of WBG polymers has been achieved through the past decade. In the initial stage, only some classic materials including poly (3-hexylthiophene) (P3HT) were thoroughly studied whereas only low PCE less than 6% was reported. [1,41] After then, the emergence of D-A polymers has been identified as the milestone for the development of WBG polymers. D-A copolymers with commutative electron-rich and electron-poor repeating units in the polymer backbones stand for one of the most popular photovoltaic materials due to its tunable optical and electronic properties relating with the manipulatable internal electron push-pull effect. [2]

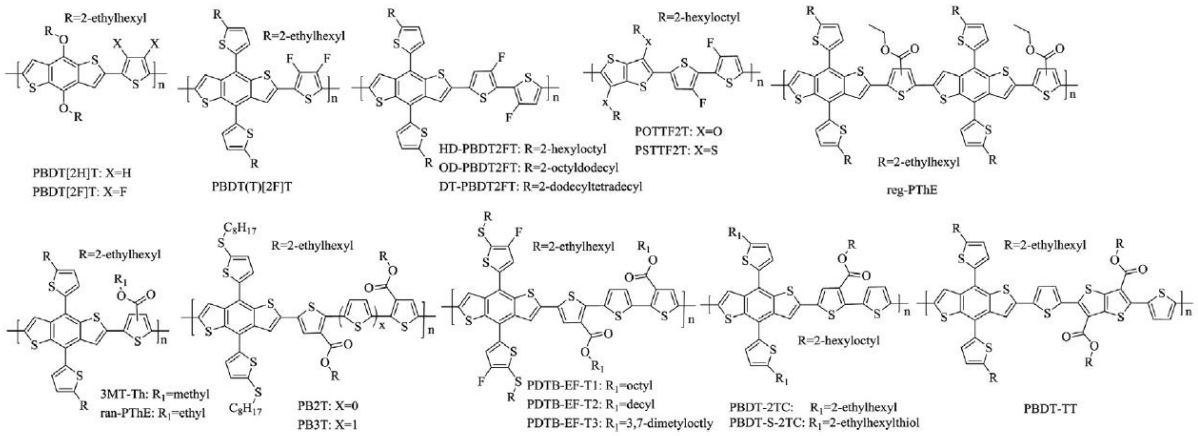

Figure 1-8 Chemical structures of BDT and PT based WBG polymers. [32]

Hou et.al introduced the famous constructing block for photovoltaic polymers, benzo[1,2-b:4,5-b0] dithiophene (BDT) unit, in 2008. [42] BDT unit exhibits rigid and large coplanar structure, and hence BDT-based polymers can achieve high hole mobilities and tunable optical bandgaps and energy levels. [32] D-A copolymers based on BDT and polythiophene (PT) alternating repeating units have been widely investigated in NFA OSCs where thiophenes introduced with electron-deficient groups acting as "weak electron acceptors" as shown in **Figure 1-8**. For example, Firdas

et al. introduced fluorine atoms to the backbone of BDT and thiophene repeating unit and varied the side chains of BDT to generate a series of donor polymers. The resulting polymer, PBDT(T)[2F]T with both introduction of fluorine and alkylthienyl side chains obtained the highest PCE of 9.8% when ITIC was applied as acceptor attributed to the lowered energy levels and reduced energy loss in the device. [43] Hou et al. reported a strand of donor polymers which are based on BDT and thiophene units which were substituted with alkylcarboxyl groups and with further fluorination. The polymer PDTB-EF-T2 with linearly decyl side chain demonstrated higher hole mobility owing to its enhanced interchain π-π interaction and stacking achieving the highest PCE of 14.2% in PDTB-EF-T2 : IT-4F devices.[44]

1.5 Green-solvent-processable Materials for Organic Electronics

The state-of-art organic electronics including OSCs discussed previously based on semiconducting conjugated organic materials are typically processed by halogenated and aromatic hydrocarbon solvents involving chloroform (CF), dichlorobenzene (CB) and 1,2-dichlorobenzene (DCB) due to the limited solubility of conjugated organic materials and the high possibility to form ordered crystalline structures and ideal molecular orientation in thin-film state in the halogenated solvents. [45–47] However, these solvents can cause very serious and normally irreversible hazards to the environment thus associated with pollution problems and also expose human health in severe danger as consequence of their high toxic properties. [45,48] Many countries in Europe, North America and Asia have proposed strict legislative regulatory restrictions on such chemicals which might expose chronic toxicity hazards to environment or human health greatly affecting the commercialization of large-scale organic electronics including the fabrication of OPVs. [45,49] As a result, it is crucial to develop organic electronics that can be processed by eco-friendly green solvents which are divided into different categories as illustrated in **Figure 1-9**. [50] As shown in

this diagram, alcohols and water should be regarded as the most ideal green solvents, and the ultimate goal is to achieve alcohols/water processable devices like OPVs that use alcohols to fabricate.

Molecular design has been investigated as one commonly adopted strategy via the structure modifications of the conjugated materials to improve their solubility in non-halogenated solvents. As shown in **Figure 1-10**, the conjugated polymers can be grafted with both functional groups and side chains to achieve the green-solvent-processable polymers.

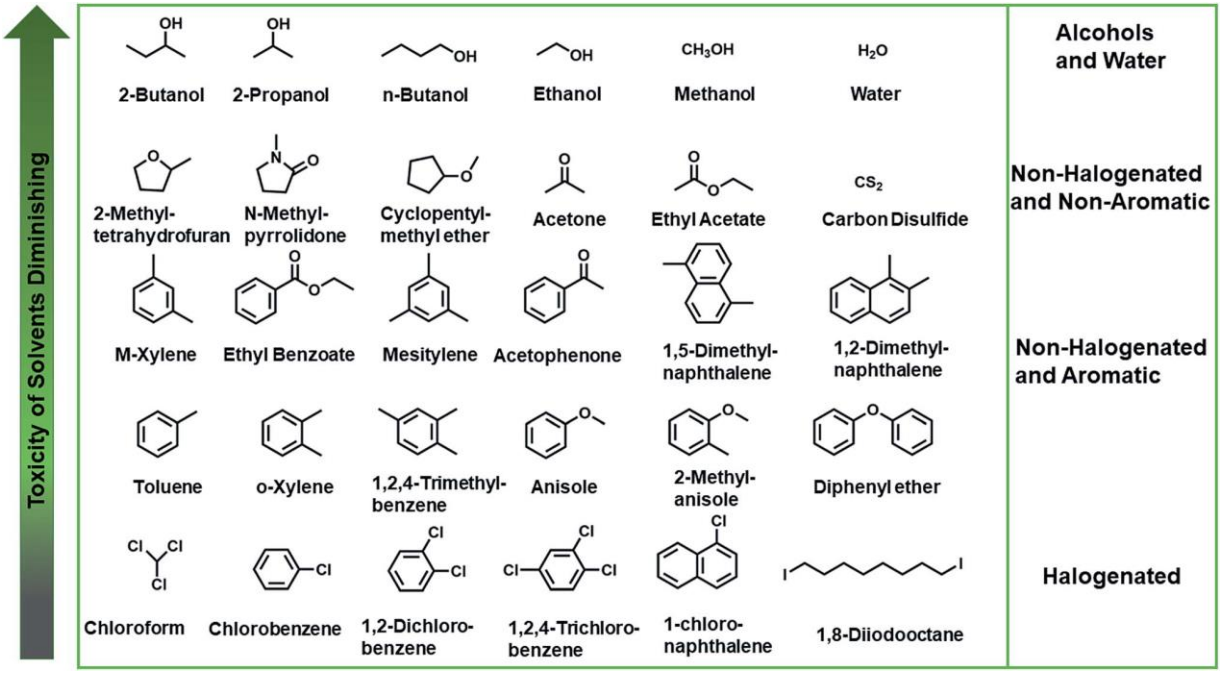

Figure 1-9 Diagram of some halogenated solvents and different categories of green solvents. [48]

The green-solvent-processable conjugated polymers can be further divided into conjugated electrolytes with functional side chains (e.g. amino, phosphate, sulfonic and quaternary ammonium groups [51]) and conjugated polymers with polar groups (e.g. tertiary amino [52], phosphonate groups [53] and oligoethylene glycol (OEG) side-chains [54]) or alkyl/alkenyl side chains. [27,55,56] Conjugated

polymers typically show complex chemical structures with high molecular weight which render them difficult to dissolve in green solvents, and hence delicate structural designs are necessary to make the conjugated polymers exhibit solubility in green solvents to fabricate various organic electronics.

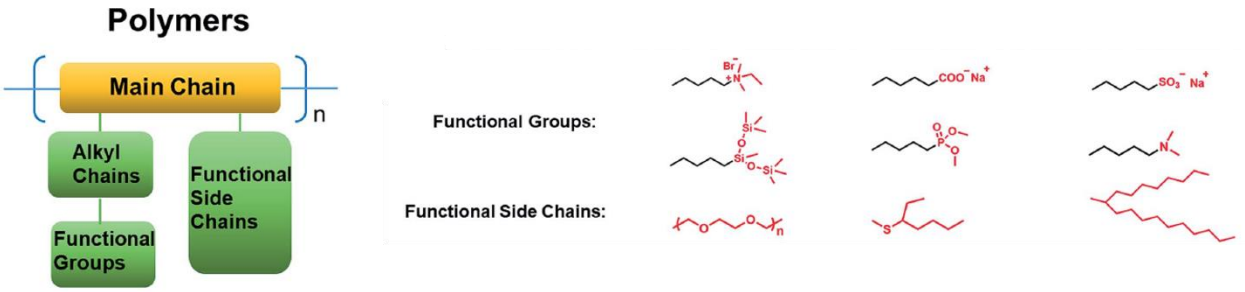

Figure 1-10 Diagram of green-solvent-processable conjugated polymers with some commonly used functional groups and side chains. [48]

1.6 Characterization of Polymers

Various techniques have been applied to investigate the properties of synthesised polymers in this work. Different characterization technologies are briefly summarized in the following part.

After the synthesis of new organic compounds, nuclear magnetic resonance (NMR) spectroscopy will be applied to determine the specific molecular structure and purity of the product. The working mechanism of NMR arises from the characteristic "nuclear spin" of nuclei including ^{1}H and ^{13}C under the applied external magnetic field, and the nucleus always present in different chemical environment will generate unique resonance frequency coupled with energy transformation. The chemical shift (δ) describes the resonance frequency shifted from reference compound such as tetramethylsilane (TMS), and specific information of measured sample can be acquired through analysis of chemical shifts in corresponding NMR spectrum. [57]

Gel-permeation chromatography (GPC) is commonly adopted technology to determine the molecular weight of resulted polymers. The macromolecules with different sizes can be effectively separated in GPC column which is packed with porous gel particles like polystyrene so that the large molecules will be eluted very fast in short elution time, whereas it takes more elution time for smaller molecules stuck by the porous particles to get through the column. The molecular weight can be determined by the conversion of elution time with the reference of known molecular weight of standard polymer such as polystyrene. [58]

Thermal properties are typically characterized by thermal gravimetric analysis (TGA) and differential scanning calorimetry (DSC) techniques. TGA measures the change of weight of polymers when temperature is increased and investigates the thermal stability. Thermally stable polymers should show durability with little loss of weight under certain range of temperature. DSC is another useful technique which monitors the heat flow between the sample and a reference undergoing phase transitions. When the temperature is increased at specific heating rate, the sample will absorb or release heat depending on the state of phase transition, and the heat will be transferred to the reference cell to maintain the same temperature with the sample. The characteristic heat-flow curve can be analysed to determine the glass transition temperature (T_g) and investigate the crystallinity of polymers with the corresponding melting point. [59]

Ultraviolet-visible (UV-vis) spectroscopy is considered as one fundamental technique to characterize the optical properties of resulted polymers which is used to acquire the absorption spectra of polymers in solution or solid state in ultraviolet-visible light region. The optical bandgap (E_g) describes the minimum required photon energy to excite an electron from the ground state which means the valance band (HOMO) to the conduction band (LUMO), and E_g can be estimated based on the edge onset wavelength (λ_{onset}) of absorption profile according to this equation [60]:

$$E_g = hv = h\frac{c}{\lambda_{onset}} = \frac{1240(eVnm)}{\lambda_{onset}(nm)}$$

where *h* represents the Planck constant, *v* is the frequency, *c* means the speed of light in vacuum. Cyclic voltammetry (CV) is used to investigate the electrochemical properties of resulting polymers. In the CV measurement, the applied potential is swept back and forth forming a cycle, and the corresponding oxidation and reduction current peaks can be analyzed to determine the energy levels. [61] The HOMO (highest occupied molecular orbital) level describes the energy to remove an electron from the molecule during the oxidation process and can be estimated from oxidation onset potential (E_{ox}^{onset}) got by CV measurement, whereas LUMO (lowest unoccupied molecular orbital) level describes the energy to excite an electron to the molecule as reductive process and can be estimated from reduction onset potential (E_{red}^{onset}) following equations below:

$$E_{\mathrm{HOMO}}\ (\mathrm{eV}) = -e\ (E_{ox}^{onset}) - 4.8\ \mathrm{eV}$$

$$E_{\mathrm{LUMO}}\ (\mathrm{eV}) = -e\ (E_{red}^{onset}) - 4.8\ \mathrm{eV}$$

where ferrocene with the HOMO level of 4.8eV is used as the reference, and its oxidation potential is set at 0eV.

Atomic force microscopy (AFM) is applied to image the polymer film morphology with very high resolution. The sharp tip on the cantilever of AFM can probe the force interactions with the atoms on the surface, and the 3D image will be generated with the response from the tip as it moves on the sample surface. [62] AFM images can reveal information including morphology, domain size and surface roughness. X-ray diffraction (XRD) is typically used to investigate the crystallinity of polymers. The XRD peaks arise from the diffraction of the incident X-ray beam which is scattered by the crystalline lattice planes at different angles in the sample material. [63] The XRD pattern should satisfy the Bragg's law: $n\lambda=2d\sin\theta$, where λ means the wavelength of incident X-ray beam, d is the separation distance between lattice planes, and θ represents the angle of incident beam.

1.7 Objective and Structure of Thesis

Although rapid progress has been made for the development of NFA-OSCs, it is essential to develop new designs of low-cost WBG polymers exhibiting both fully complementary light absorption when paired with NFAs and deep HOMO levels to achieve higher V_{oc} values and lower energy loss (E_{loss}) in the OSCs. Moreover, there is urgent need to exploit green-solvent-processable conjugated polymers to enable the commercialization of organic electronics without chronic hazards to the environment and human health.

In chapter 2, two novel donor polymers including PTIBDT and its fluorinated analog, PTIFBDT, will be discussed as further development of our previously reported Type II D-A copolymers. The optical and electrochemical properties of the new donor polymers were carefully characterized, and the charge transport mobilities were measured in organic field-effect transistor (OFET) devices. Inverted OSCs were fabricated with the developed polymers as donor and ITIC as acceptor, and the vertical charge mobilities and film morphology would be further investigated.

In chapter 3, strong electron-withdrawing carboxyl functional group was introduced to the side chain of PTIBDT polymer to further synthesize PTIABDT polymer with acetyl group and PTIPBDT with propionyl group showing better solubility. Different technologies were adopted to study their thermal, optical and electrochemical properties including charge mobilities in OFET devices. The polymers were then used as donor polymers matched with ITIC or IT-4F acceptors in the inverted OSC devices to show their photovoltaic properties.

In chapter 4, the design and synthesis of isoindigo(ID) based conjugated polymer will be discussed to achieve the objective to develop green-solvent-processable organic electronics improving the environmental pollution caused by toxic halogenated solvents.

As the last chapter, there will be a summary for the work in this thesis and some proposed future work directions for further investigation in chapter 5.

Chapter 2 Synthesis and Characterization of PTIBDT and PTIFBDT Polymers

2.1 Introduction

Wide-bandgap (WBG) polymers based on building blocks such as polythiophene (PT) and benzodithiophene (BDT) are suitable candidates as donor polymers to match with NFAs in NF-OSC systems due to their complementary light absorption in the short wavelength region and low-lying HOMO levels which can promote both J_{sc} and V_{oc} leading to high final PCE values. [43,64]

Donor-acceptor (D-A) copolymers have attracted much attention to be used as WBG donor polymers in NFA-OSC systems since they have demonstrated superior advantages including broad light absorption and tunable energy levels. [3,12] D-A polymers can be classified into two categories as indicated in **Figure 2-1** with Type I polymers exhibiting both D-A repeating blocks on the main chain backbone, whereas Type II polymers have D blocks on the backbone and A blocks on the side chain. Type I D-A polymers typically show relatively narrow optical bandgaps and high energy levels due to the internal charge transfer (ICT) effect between D-A repeating units, [65] which limit the further improvement of PCE of NFA-OSC devices.

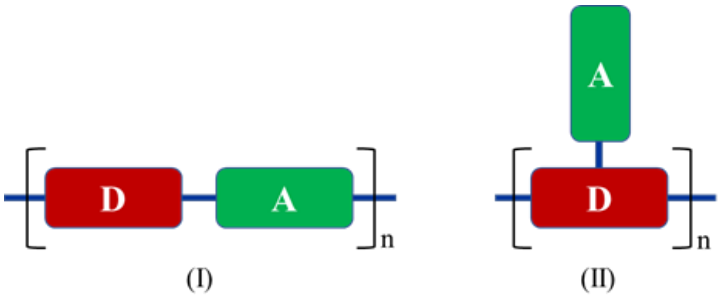

Figure 2-1 Structures of Type I and Type II D-A polymers. [66]

To overcome the limitations, Type II D-A polymers comprised of a donor-backbone and acceptor-side chain are introduced exhibiting advantage of D-A structures which polarize the polymer and relieve the binding energy of excitons by increasing the dipole moment or dielectric constant of the polymer chain thus enhancing the exciton separation process and photovoltaic properties. [67] Additionally, a wide-bandgap and low-lying HOMO level can be achieved since the accepting units are located on the side chain. [66] Recently, our group reported a Type II D-A donor polymer, namely PTIBT, utilizing bithiophene unit as the donor-backbone and electron-withdrawing indolin-2-one unit as the acceptor-side chain with superior low synthetic complex, and the donor polymer exhibits deep HOMO level of -5.41eV as well as a large optical bandgap of 1.80eV. A high PCE of 5.72% was finally obtained when PTIBT polymer was used as donor polymer with ITIC as NFA. [66] (**Figure 2-2**)

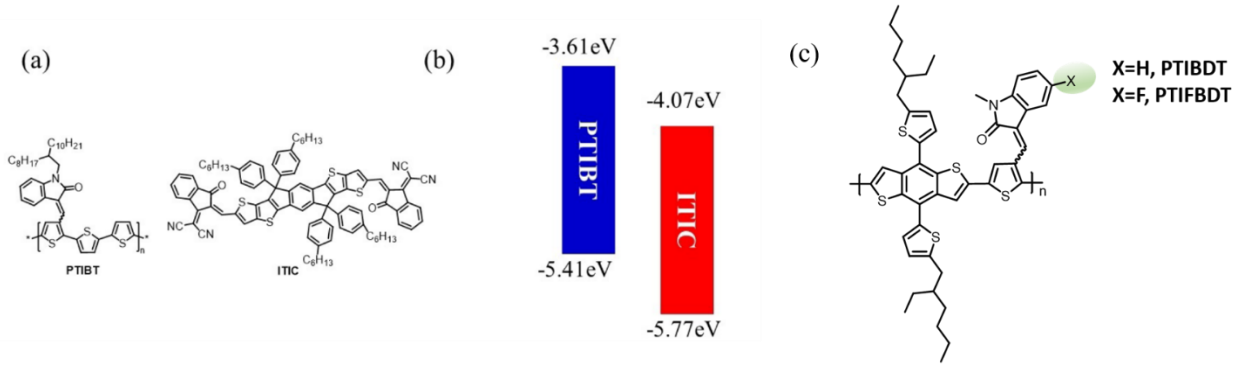

Figure 2-2 (a) Structures and **(b)** energy levels alignment of PTIBT and ITIC **(c)** Structures of PTIBDT and PTIFBDT.

However, the PCE of PTIBT: ITIC system has been shown seriously restricted by the low V_{oc} of 0.66V which could be related with the inappropriate energy level offset between donor polymer and NFA materials. In addition, the highly amorphous and disordered film resulted by the heavily isomeric side chains exhibited great effect on the J_{sc} and FF values.

Interestingly, it is found that the benzodithiophene (BDT) unit demonstrates highly coplanar and symmetric structure which supports the charge transport and leads to suitable energy levels. More importantly, the two-dimensional (2D) BDT-T unit was developed with 2-ethylhexyl thienyl group attached to the BDT structure to further downshift the HOMO level and facilitate the hole mobility. [68] Side-chain engineering has been reported to play a crucial role on the modulation of properties of polymer such as solubility, molecular weight and processability. However, improper side chain attachment can decrease the π-π stacking between polymer chains thus leading to reduced charge mobility and light absorption which is harmful to photovoltaic performance. [12] For the polymer PTIBT, the attachment of long and branched alkyl chain, 2-octyldodecyl, indeed introduced much steric hindrance to the polymer chains interrupting the conjugation of polymer backbone and leading to twisted polymer chain especially the alkyl chain was attached to the acceptor-side chain unit, indolin-2-one, which already increased the structure hindrance of the polymer backbone. Consequently, shorter alkyl chain might address this problem with less effect on the conjugation of polymer chains. Another approach of side chain engineering has been frequently investigated which is fluorination, as an efficient modification to promote the performance of donor polymers due to the high electronegativity of introduced fluorine atoms.[69–73] Specifically, the introduction of fluorine atoms onto the electron-poor acceptor unit can strongly stabilize the energy levels including LUMO and HOMO and also reduce the undesired steric hindrance existed in the polymer chains.[74] Consequently, fluorine substitution has been reported to be one of the most effective ways to deepen the HOMO levels of donor polymers and thus to achieve a high V_{oc} due to the strong electro-withdrawing property of introduced fluorine atoms. [75–77]

In this chapter, two novel Type II D-A polymers including PTIBDT and its fluorinated analog PTIFBDT as shown in **Figure 2-2 (c)** have been successfully designed and synthesized as further

development based on PTIBT polymer. 2D BDT-T unit was used as backbone donor instead of bithiophene in PTIBT to further down-shift HOMO level to enhance a high V_{oc} and reduce energy loss (E_{loss}) in OSC devices. Additionally, a short methyl chain was attached to the indolin-2-one unit to improve the steric hindrance may be caused by long alkyl side chain in PTIBT. At the same time, fluorination effect was also investigated for the novel Type II D-A copolymer, PTIBDT, with fluorine atom attached to the 5-position of the indolin-2-one side chain to obtain the fluorinated polymer, PTIFBDT.

2.2 Structure Simulation by Density Functional Theory (DFT)

At the first stage, Density Functional Theory (DFT) was adopted to simulate the two donor polymers, PTIBDT and PTIFBDT to predict the corresponding frontier energy levels and electronic structures, and the simulations were performed by the Gaussian 09 at the B3LYP/6-31(d) level. The structures of the repeating blocks of PTIBDT and PTIFBDT which involves TIBDT and TIFBDT units are shown in the **Figure 2-3**. In theory, there is possibility to form two different configurations of TIBDT and TIFBDT involving E-isomer and Z-isomer since the vinylene linkage between BDT and indolin-2-one can rotate resulting in different configurations (**Figure 2-3**). Consequently, both isomers were simulated to predict the optimized geometries and frontier molecular orbitals. Interestingly, it was found that both Z-isomers of TIBDT and TIFBDT demonstrated a wider optical bandgap with slightly higher-lying LUMO levels and lower-lying HOMO levels revealing different configurations could exert influence on the properties of resulting polymers. Surprisingly, the introduction of fluorine atom to TIFBDT only down-shifts the HOMO level of 0.05eV for E-isomer and 0.04eV for Z-isomer when compared with TIBDT suggesting fluorination on acceptor side chain may show less effect on the Type II D-A copolymers, and the Z-isomer of TIFBDT was simulated to achieve the lowest theoretical HOMO level of -

5.20eV. `Besides, it is declared that the LUMO levels are mainly delocalized around the indolin-2-one acceptor unit with partial distribution on BDT unit, and the HOMO levels are delocalized along the polymer backbone for both donor polymers with Z-configurations. In E-isomer configuration, both TIBDT and TIFBDT were observed to show separate charge distribution separation with most LUMO distribution on the indolin-2-one unit and HOMO distribution on BDT unit suggesting the polymers in E-configuration should be a little bit more electron-deficient compared with polymers in Z-configuration.

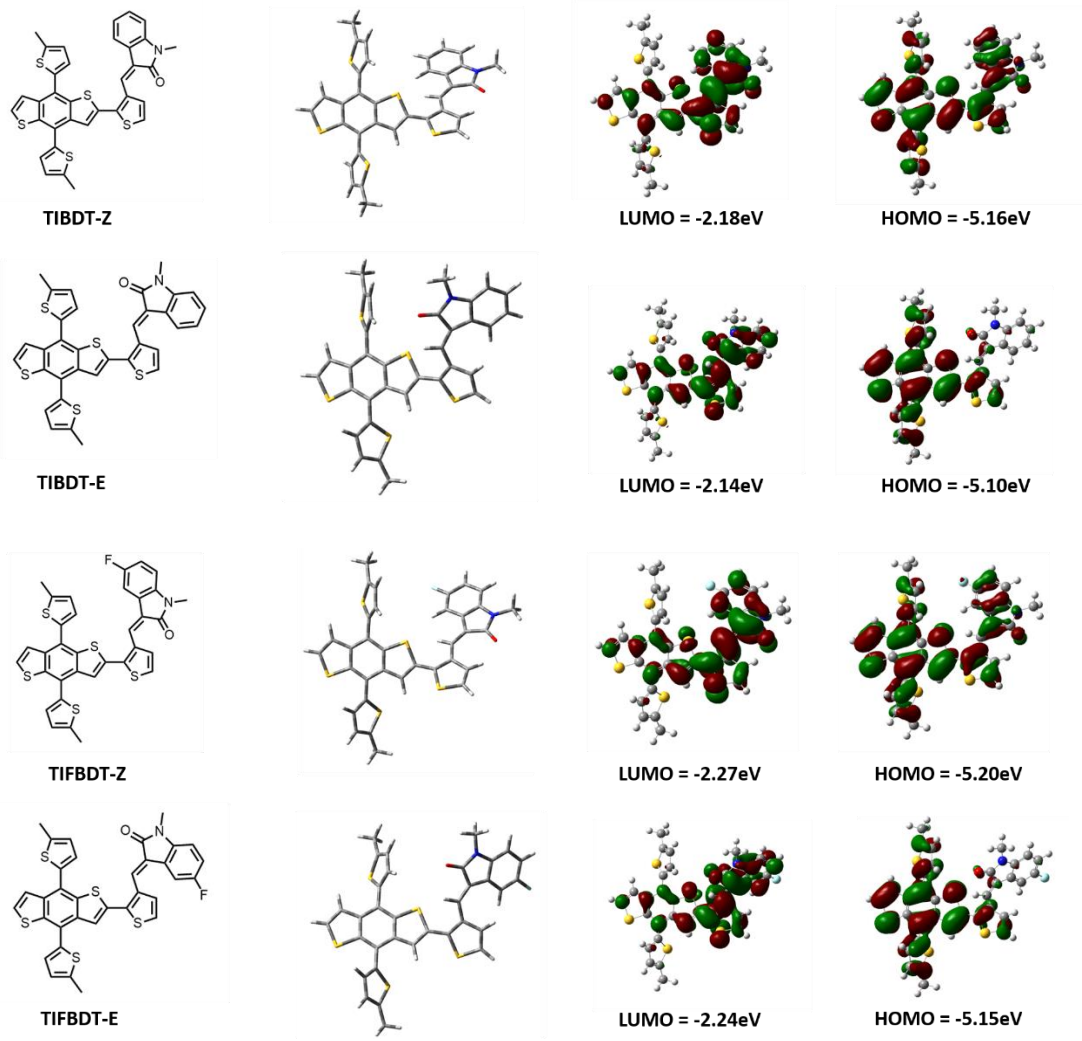

Figure 2-3 Optimized geometries of PTIBDT and PTIFBDT and predicted energy levels in different configurations.

2.3 Synthesis of Monomers and Polymers

PTIBDT and its fluorinated analog PTIFBDT were successfully synthesized according to the synthesis route as indicated in **Figure 2-4**. Knoevenagel condensation method was used to prepare M1 and Compound 2 via the condensation between 1-methyloxindole & 5-fluoroindole and 2,5 dibromothiophene-3-carbaldehyde where piperidine was added as catalyst with anhydrous ethanol as solvent according to the literature. [78] M1 and Compound 2 directly precipitated out from the solvent, and Compound 2 was further alkylated with one methyl group on the nitrogen atom of indolin-2-one to improve the solubility and stabilize the compound producing M2. ^{1}H NMR was performed to characterize the two monomers, M1 and M2, and it was found that only Z-isomer was formed during the condensation process since the ^{1}H NMR data was consistent with the monomer of PTIBT, TI, in Z configuration which got both Z/E isomers after the condensation reaction.

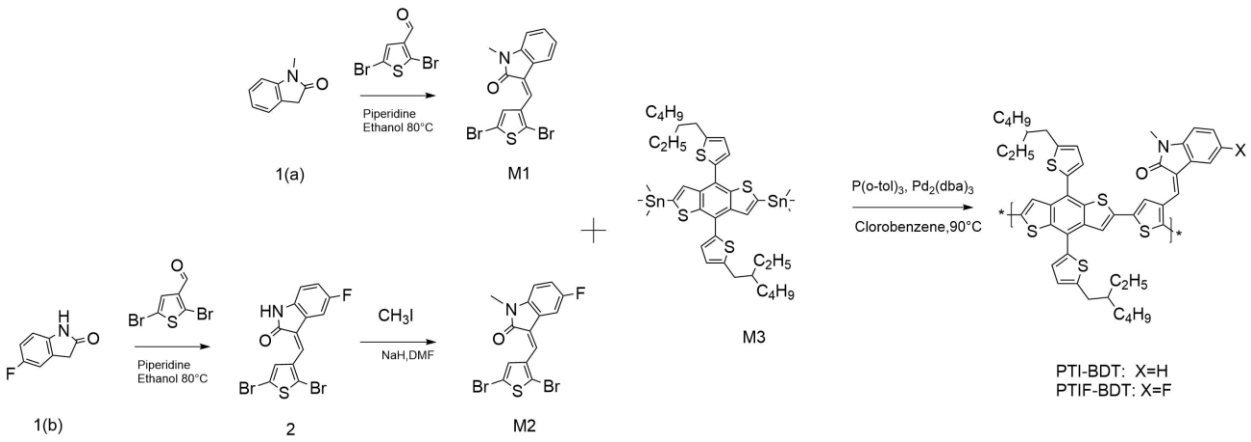

Figure 2-4 Synthesis route of PTIBDT and PTIFBDT.

As shown in **Figure 2-5** which demonstrates the ^{1}H NMR data of M1 and M2, the peak that is located at 8.75ppm for M1 and 8.77ppm for M2 corresponds to the special hydrogen bond that is formed between the carbonyl group from indolin-2-one unit and the 4-position hydrogen atom of the thiophene ring (**Figure 2-5**). This special hydrogen bond has been verified by two-dimensional NMR and Fourier-transform infrared spectroscopy (FTIR) technique in the literature. [66]

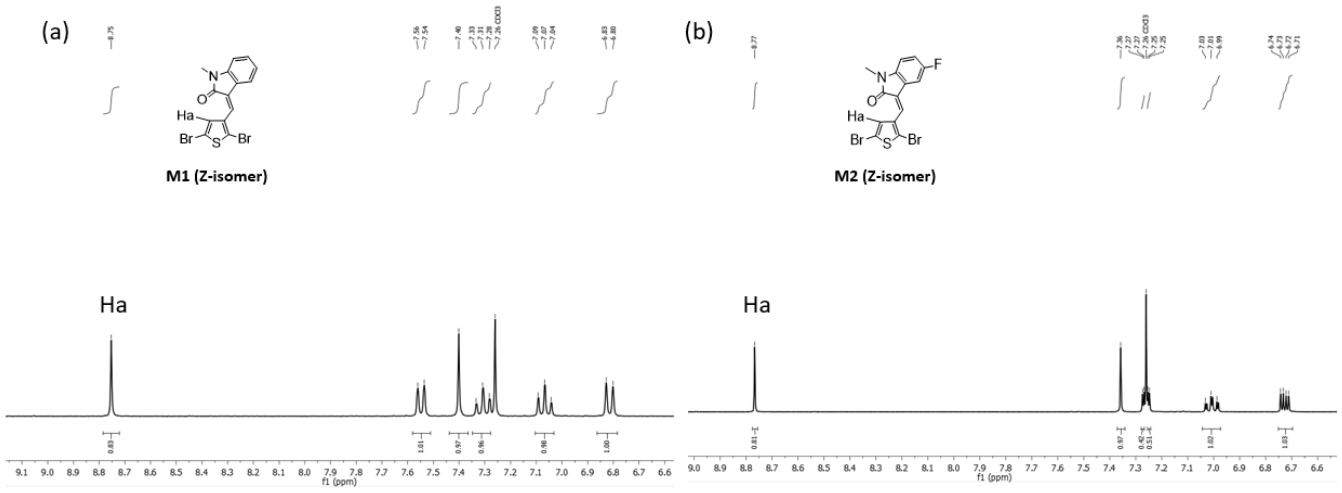

Figure 2-5 ^{1}H NMR of monomer of PTIBDT **(a)** and PTIFBDT **(b)**.

The monomer TI for polymer PTIBT was found to form a mixed compound of isomers (Z/E) in a ratio of 21:79 (Z:E) after the Knoevenagel condensation reaction, and the separated pristine Z or E isomer would be transformed to another configuration after heated at 90℃ for 12hrs resulting in a mixture with 1:1 ratio of two isomers. As a result, the polymer PTIBT was synthesized with the mixture of isomers which resulted in the regiorandom side chain distribution of the repeating units causing less favorable amorphous film morphology. In contrast, both M1 and M2 monomers in this work demonstrated superior configurational stability where the monomers could maintain almost 100% Z-configuration after heated at 90℃ for 22hrs as illustrated in **Figure 2-6**. According

to the ^{1}H-NMR after heating, the absence of protons from E-isomer revealed little isomerization during the heating process.

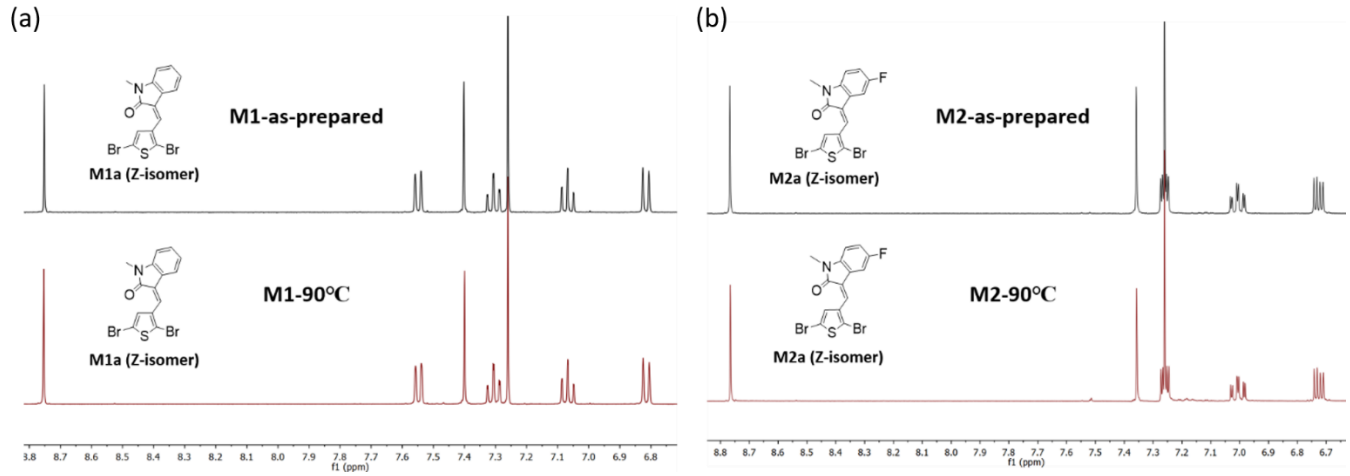

Figure 2-6 ^{1}H NMR spectra of M1**(a)**, and M2 **(b)** as-prepared (black) and heated at 90 ℃ for 22 hrs in chlorobenzene (red) in CDCl3.

The desired PTIBDT and PTIFBT polymers were synthesized via the Stille cross-coupling method according to the literatures with 1:1 ratio of monomer M1 or M2 and BDT-T stannane compound utilizing $Pd_2(dba_3)$ as catalyst with the ligand, namely $P(o\text{-}tol)_3$, as well as chlorobenzene used as the solvent. After the polymerization was finished, methanol was used to get the crude polymer products as the precipitate, and the crude products were then washed and purified through Soxhlet extraction method using acetone and hexane solvents. The final polymers were extracted by chloroform, and dark green polymer films were obtained when chloroform was removed. Both PTIBDT and PTIFBDT demonstrated good solubility in commonly used organic solvents at room temperature including chloroform and chlorobenzene. Although M1 and M2 showed superior structural stability, this stability could not be maintained during the polymerization process, and consequently, the donor polymers including PTIBDT and PTIFBDT were found to possess regiorandom side chain configuration with the Z/E isomer ratio of 1: 2.57 for PTIBDT and 1: 1.44

for PTIFBDT according to the High-temperature (HT) ^{1}H NMR spectra of polymers measured in 1,1,2,2-tetrachloroethane at 90°C. (**Figure 2-7**) The Z/E ratio could be determined via the integral of the hydrogen bond which located at 8.68ppm for PTIBDT and 8.72ppm for PTIFBDT.

(a)

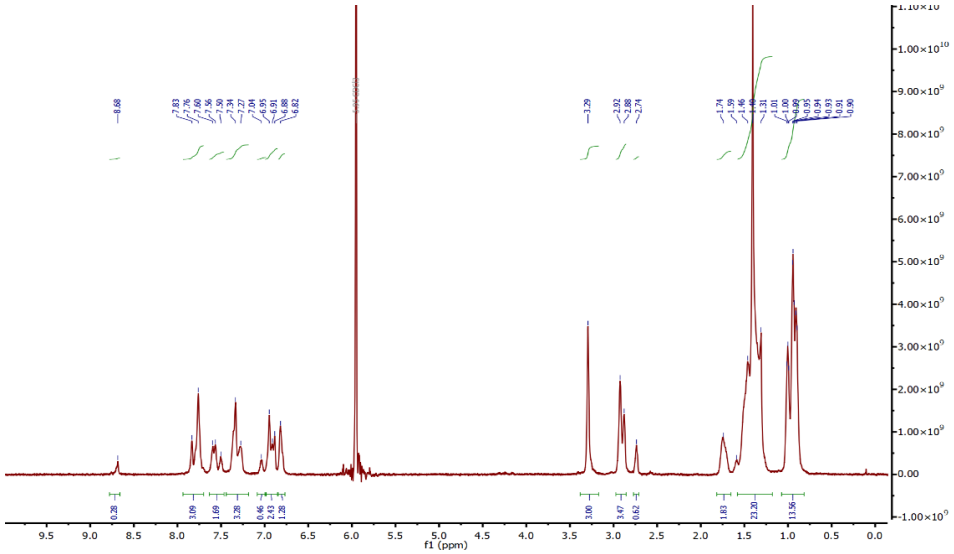

(b)

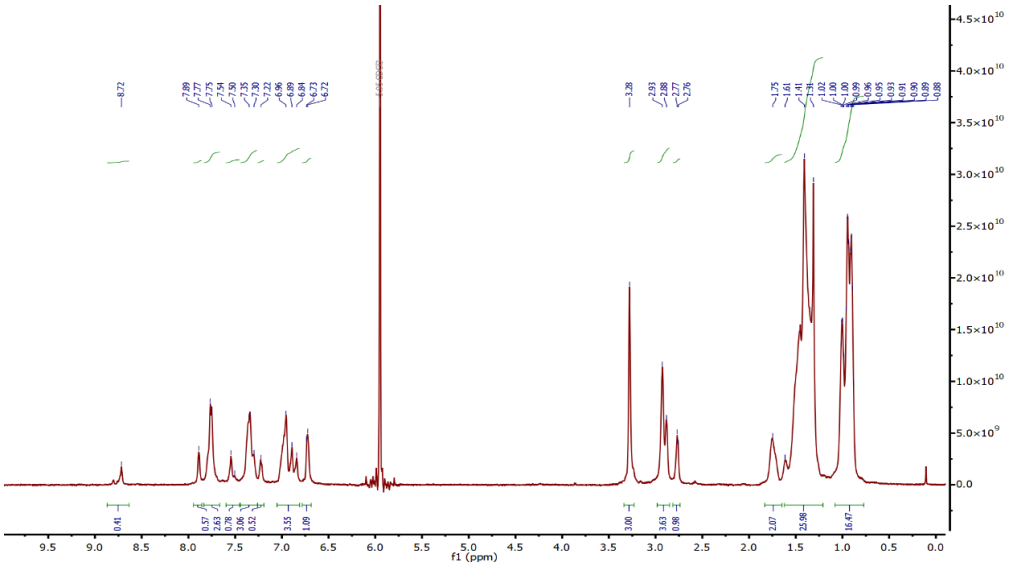

Figure 2-7 ^{1}H NMR spectra of PTIBDT**(a)**, PTIFBDT **(b)** in 1,1,2,2-tetrachloroethane which was measured at 90°C.

2.4 Characterization of PTIBDT and PTIABDT

2.4.1 Physical Properties (GPC, TGA and DSC)

The molecular weight of PTIBDT and PTIFBDT was measured using high-temperature gel permeation chromatography (HT-GPC) with 1,2,4-reichlorobene as the eluent at 110℃, and polystyrene was employed as the standard. The number-average molecular weight (Mn) was determined to be 60.2 kDa and 20.5 kDa for PTIBDT and PTIFBDT, respectively. Polydispersity index (PDI) for PTIBDT and PTIFBDT were measured to be 2.65 and 2.76 indicating the high molecular weight of both synthesized polymers. (**Figure 2-8** and **Table 2-1**)

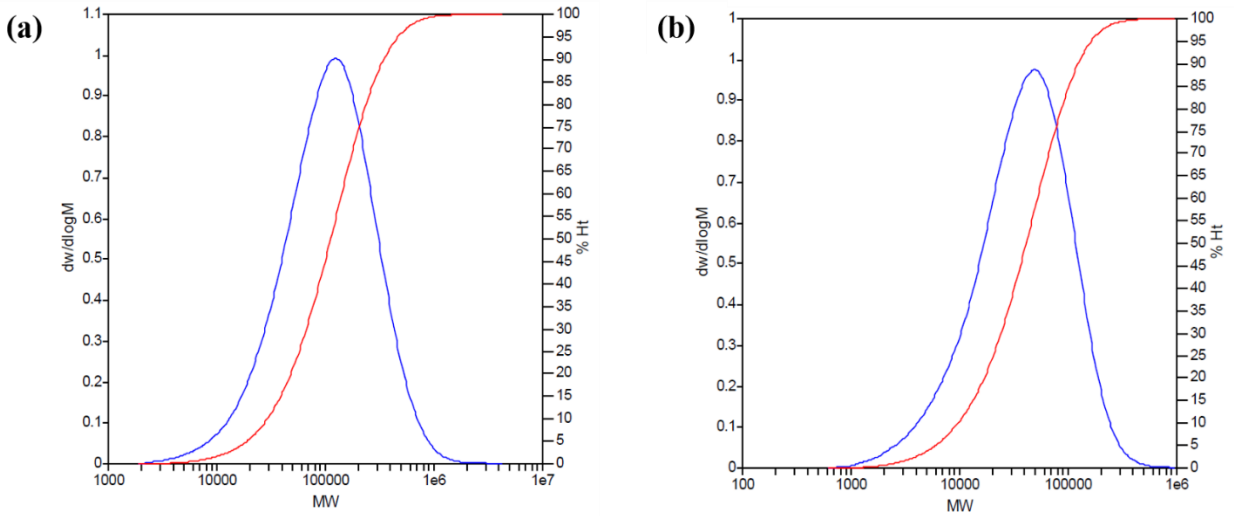

Figure 2-8 High temperature GPC molecular weight distribution for **(a)** PTIBDT, and **(b)** PTIFBDT, measured using 1,2,4-trichlorobenzne as eluent at 110 °C with a flow rate of 1.00 $mLmin^{-1}$.

Thermal gravimetric analysis (TGA) was conducted to investigate the thermal properties for two polymers. The polymers exhibited almost negligible first step of decomposition at 295℃ for PTIBDT and 269℃ for PTIFBDT. The decomposition temperature of second step for PTIBDT and PTIFBDT were estimated to be 353℃ and 345℃, respectively, demonstrating their good thermal stability to be applied in OSC and OFET devices which might need a high temperature

durability. (**Figure 2-9** and **Table 2-1**) The differential scanning calorimetry (DSC) data (**Figure 2-9**) of both two polymers showed very weak glass transition temperature which was 65℃ for PTIBDT and 70℃ for PTIFBDT with no obvious exothermic nor endothermic transitions implying the absence of crystalline domains. (**Table 2-1**)

Table 2-1 Molecular weight and thermal properties of PTIBDT and PTIFBDT

Polymers	M_n (kDa)	M_w(kDa)	$Đ$ (M_w/M_n)	T_d ^{1st}(℃)	T_d^{2nd}(℃)	T_g(℃)
PTIBDT	60.2	159	2.65	295	353	65
PTIFBDT	20.5	56.6	2.76	269	345	70

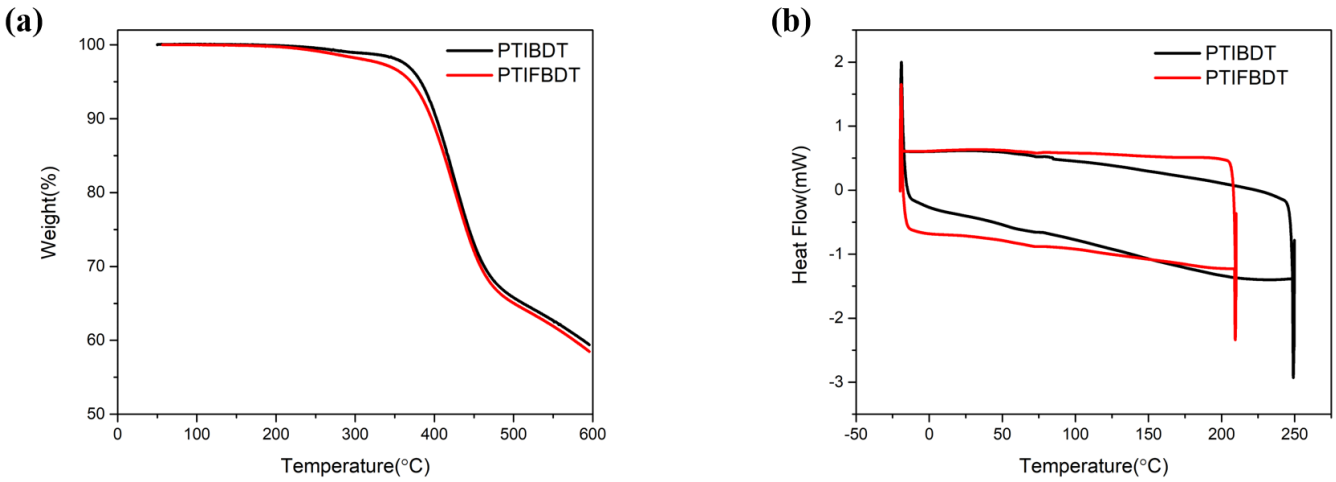

Figure 2-9 TGA **(a)** and DSC **(b)** curves of PTIBDT and PTIFBDT.

2.4.2 Optical and Electrochemical Properties (UV-vis and CV)

The Ultraviolet-visible (UV-vis) profiles of PTIBDT and PTIFBDT as solution and films are demonstrated by **Figure 2-10**, and the summary of their optical properties is shown in the **Table 2-2**. For the solution of polymers in chloroform, PTIBDT showed the absorption maximum (λ_{max}) at 540nm, and the value for PTIFBDT is 536nm. The two polymers show similar absorption shape

composed of two absorption bands which involve a band with high energy due to the π-π* transition located between 300 and 400nm and a band with low energy due to ICT transitions of the donor-acceptor (D-A) units of the polymer in the visible light range of 400-700nm. In compare with the absorption spectra in solution state which should be more random, the absorption maximums of the polymers demonstrate significant red shift in the thin-film sate because of the better molecular aggregation and π-π stacking of the polymer chains changing from solution to solid state. [79] The optical bandgap calculated from thin-film absorption spectra wavelength onsets is 1.91eV for PTIBDT and 1.89eV for PTIFBDT demonstrating a wider bandgap compared with our previously reported Type II D-A polymer, PTIBT which showed an optical bandgap of 1.8eV. PTIFBDT exhibited a lower band gap with a little redshift compared with PTIBDT which was consistent with the reported decreased band gaps of fluorinated polymers due to the stronger push-pull effect after fluorination. [2,41] For both PTIBDT and PTIFBDT polymer donors, the increased bandgap reveals a broadened light absorption range and forms complementary light harvest fully covering the solar spectrum from 350 to 800nm when combined with the absorption of ITIC with the maximum absorption at 706nm as shown in **Figure 2-10** which should be beneficial for the photocurrent generation and thus lead to better photovoltaic performance.

Table 2-2 Optical and electrochemical properties of PTIBDT and PTIABDT

Donor Polymers	**$\lambda_{max}^{sol.}$ (nm)**	**$\lambda_{max}^{film.}$ (nm)**	**$\lambda_{onset}^{film.}$ (nm)**	**E_g^{opt} (eV)**	**HOMO (eV)**	**LUMO (eV)**
PTIBDT	541	563	649	1.91	-5.59	-3.69
PTIFBDT	534	554	656	1.89	-5.60	-3.70

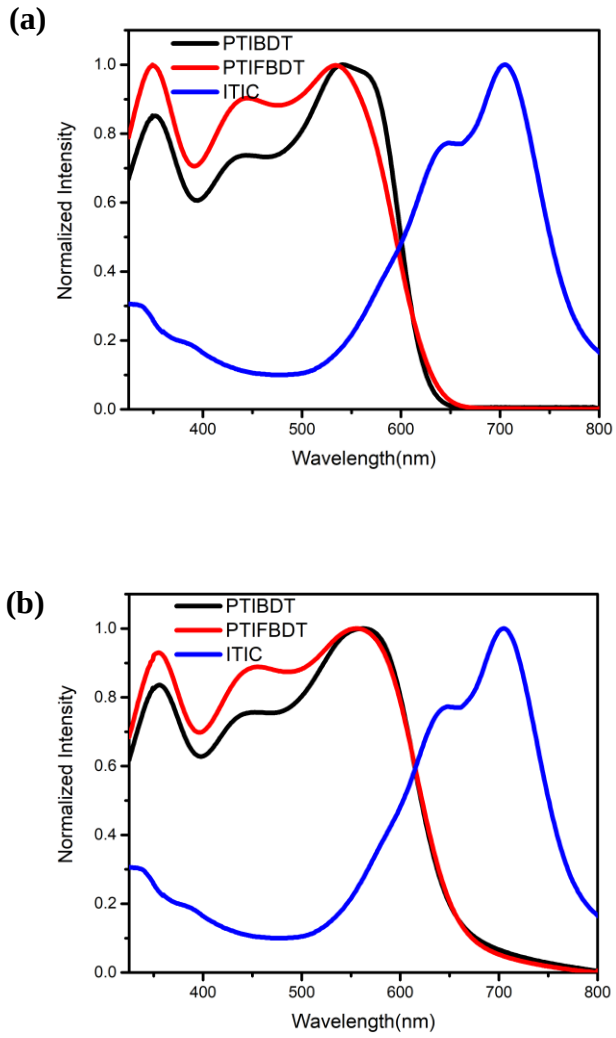

Figure 2-10 UV-vis spectra of PTIBDT, PTIFBDT and ITIC **(a)** in chloroform and **(b)** as spin-coated films at room temperature.

In order to investigate the electrochemical properties, the cyclic voltammetry (CV) of PTIBDT and PTIFBDT were measured and shown as in **Figure 2-11**. Consequently, the HOMO and LUMO levels of PTIBDT are calculated to be -5.59eV and -3.69eV, and the values of PTIFBDT are estimated to be -5.60 and -3.70eV in correspondence with the oxidation potentials from the CV profile which is used to estimate HOMO levels, whereas LUMO levels can be calculated combing with optical bandgaps since no reduction CV band was observed. The energy levels of PTIFBDT

are slightly lower than that of PTIBDT as a result of the introduced strong electron-withdrawing fluorine atom, and this small difference also agrees with the DFT simulation results where the fluorination of accepting side chain shows less effect on the HOMO levels compared with typical Type I D-A copolymers showing 0.1-0.2 eV lower HOMO levels after fluorination [80–82] The PTIBDT and PTIFBDT also demonstrated much lower HOMO levels compared with our reported Type II D-A polymer, PTIBT with the HOMO of -5.41eV revealing the substitution of BDT unit with the bithiophene one can effectively enhance the push-pull effect in D-A structure which is also consistent with the theoretical DFT results showing the highly delocalized LUMO on acceptor and HOMO on BDT unit. Moreover, the Type II polymers including PTIBT, PTIBDT and PTIFBDT show much downshifted HOMO levels (from -5.41ev to -5.60eV) and broadened band gaps (from 1.80eV to 1.91eV) in compare with the typical Type I D-A polymer, PTEI-T, with both acceptor-indolin-2-one and donor-bithiophene on the backbone exhibiting a band gap of 1.57eV and HOMO of -5.33eV, respectively. [83] The wider band gaps as well as deep-lying HOMO levels of PTIBDT and PTIFBDT will effectively promote a much higher V_{oc} and achieve complementary light harvesting when matched with low-band gap NFA materials to obtain higher PCE in OSCs.

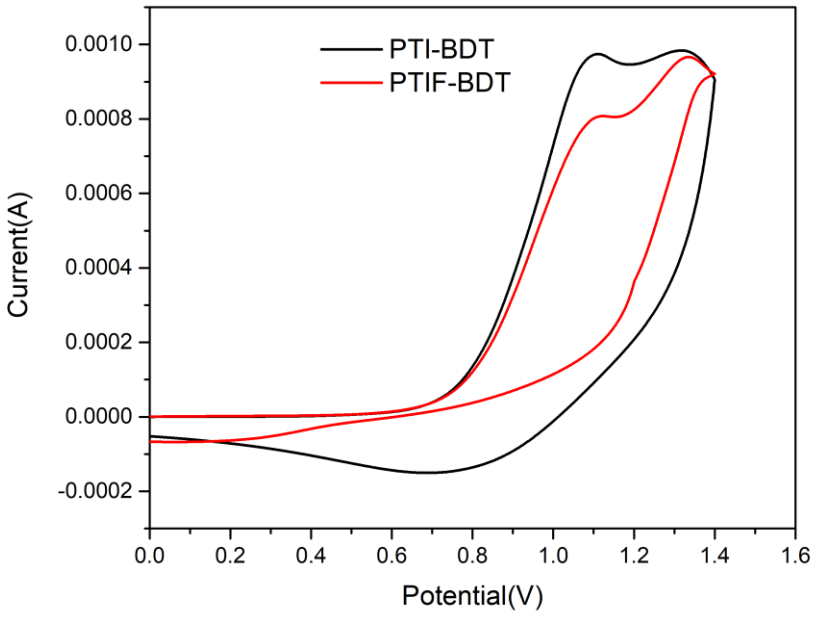

Figure 2-11 Cyclic voltammetry profiles of PTIBDT and PTIFBDT acquired in tetrabutylammonium hexafluorophosphate solution (0.1M) dissolved in acetonitrile at a scan rate of 0.1V/s.

2.4.3 Organic Field-effect Transistor (OFET) Performances

The lateral charge mobilities of PTIBDT and PTIFBDT were investigated as semiconducting layers in OFET devices in bottom-gate bottom-contact (BGBC) configuration which were manufactured on SiO_2/Si wafers with modification of dodecyltrichlorosilane (DDTS) and deposited gold source-drain contacts. The illustration of BGBC-OFET device is shown in **Figure 2-12**, and the details describing fabrication as well as characterization process are listed in Experimental Section 2.7. The polymer films were formed on the wafer substrates via the spin-coating method, and the fabricated devices were further heated at different temperatures (50℃, 100℃, 150℃, 200℃) to measure the corresponding mobility at each temperature.

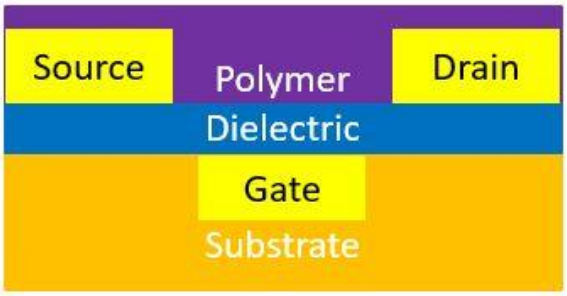

Figure 2-12 Configuration of a bottom-gate bottom-contact (BGBC) organic field-effect transistor (OFET).

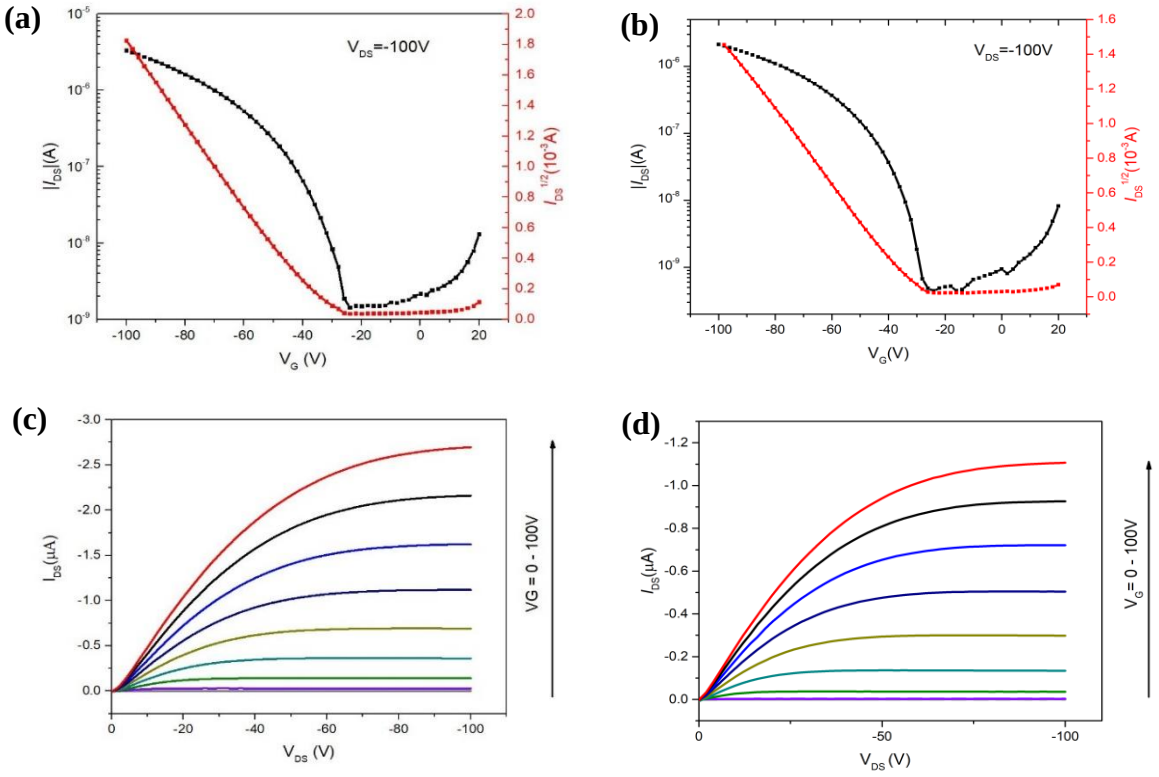

Figure 2-13 Transfer and output curves of PTIBDT annealed at 150°C [**(a)** and **(c)**] and PTIFBDT annealed at 100°C [**(b)** and **(d)**].

As shown in **Figure 2-13**, both polymers exhibit typical p-type behaviours with PTIBDT achieving the highest hole mobility which is up to 0.0044 $cm^2V^{-1}s^{-1}$ at an annealing temperature of 150℃. PTIFBDT shows the best hole mobility of 0.0026 $cm^2V^{-1}s^{-1}$ when annealed at 100℃ which is much lower than PTIBDT. The hole mobility could be calculated by extracting the saturation current regime from the characteristic transfer curve using this equation:

$$I_{DS} = \frac{\mu CiW}{2L}(V_G - V_T)^2$$

where I_{DS} means the drain-source current, μ represents charge carrier mobility, Ci means the gate dielectric layer capacitance per unit area (~ 11.6 nF cm^{-2}), L is the channel length (30 μm), W is the channel width (1000 μm), V_G is the applied gate voltage, and V_T is the threshold voltage which need to be calculated.

Indeed, the p-type OFETs based on donor-acceptor semiconducting polymers have been reported to achieve a very high level of hole mobility up to 20$cm^2V^{-1}s^{-1}$. [84] Although the polymers in this work show limited mobilities, it's still possible to obtain high PCE results with these polymers used as donor since the lateral carrier mobility shows less influence on the photocurrent generation compared with the vertical mobility which will be discussed later. Both polymers demonstrated low sensitivity to temperature annealing due to their superior amorphous properties which would be further confirmed by XRD data. Noticeably, both polymers showed high threshold voltage (V_{th}) around -30V demonstrating massive charge carrier traps could exist so that a large V_{th} was required to overcome this trapping problem to turn the transistor "on". The serious hole trapping was assumed to be due to the one pair of free electrons introduced by the nitrogen atom of indolin-2-one unit causing the considerable traps for the free hole carriers. It was noticed that PTIFBDT still exhibited comparable large V_{th} (~30V) in compare with PTIBDT indicating weak electron-withdrawing effect of fluorination, and the hole trapping could also hinder the transport of charge

carrier resulting in lower photocurrent generation. Consequently, it is crucial to improve this hole trapping problem which will be discussed in Chapter 3.

Table 2-3 BGBC OFET performances of PTIBDT and PTIFBDT at different annealing temperatures

Polymer	Annealing Temp (℃)	Avg mobility ($cm^2V^{-1}s^{-1}$)	Max mobility ($cm^2V^{-1}s^{-1}$)	V_{th} (V)	$I_{ON/OFF}$
PTIBDT	RT	0.0024±0.000089	0.0025	-25.0	10^4
	50	0.0026±0.00018	0.0028	-29.4	10^4
	100	0.0036±0.00035	0.0042	-33.8	10^4
	150	**0.0041±0.00022**	**0.0044**	**-27.7**	10^4
	200	0.0033±0.00018	0.0036	-28.5	10^4
PTIFBDT	RT	0.0019±0.00016	0.00218	-31.06	10^4
	50	0.0017±0.00018	0.001971	-33.72	10^4
	100	**0.0024±0.00024**	**0.002606**	-33.36	10^4
	150	0.0021±0.000089	0.002259	**-23.05**	10^4
	200	0.0020±0.00011	0.002218	-28.59	10^4

2.5 Organic Photovoltaic (OPV) Performances

The wide optical bandgaps and low-lying energy levels make both PTIBDT and PTIFBDT polymers promising donor polymers for fabrication of NFA OSC devices. The exciton diffusion and dissociation efficiency which show great effect on the photocurrent generation were firstly investigated by photoluminescence quenching efficiency (PLQE) technology before fabrication of OSC devices.

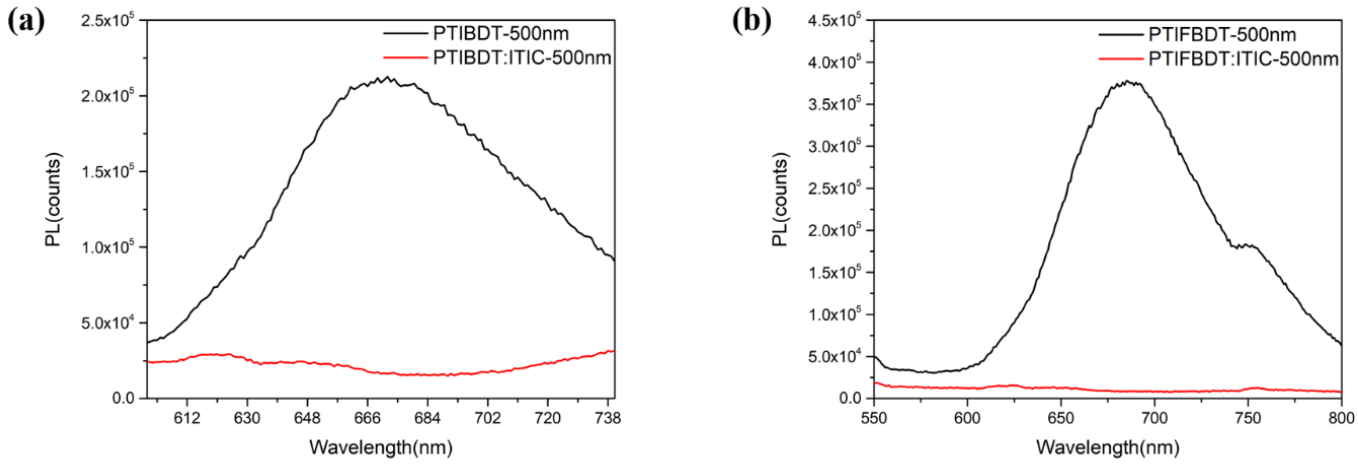

Figure 2-14 Photoluminescence spectra of **(a)** PTIBDT neat film and blend film of PTIBDT: ITIC, **(b)** PTIFBDT neat film and PTIFBDT: ITIC when excitation wavelength is 500nm.

As shown in **Figure 2-14**, the PLQE of blend films of PTIBDT:ITIC and PTIFBDT:ITIC were measured to be 92% and 98%, respectively, when PTIBDT and PTIFBDT pristine films were excited at 500nm wavelength to get rid of photoluminescence from ITIC due to the weak absorption of ITIC at 500nm. At this excitation wavelength, the dominated emission should arise from donor polymers, and the emission of D-A blend films was quenched since ITIC was introduced. The high PLQE of two blend films demonstrated efficient electron dissociation efficiency when excitons were generated. Meanwhile, the PLQE of pristine film of ITIC when blended with PTIBDT and PTIFBDT were determined to be 75% and 94%. (**Figure 2-15**) The much lower PLQE of PTIBDT:ITIC film when quenched with ITIC showed less efficient hole carrier generation and could cause charge carrier accumulation which was also consistent with lower SCLC hole mobilities of PTIBDT:ITIC blend film that would be discussed in the following section.

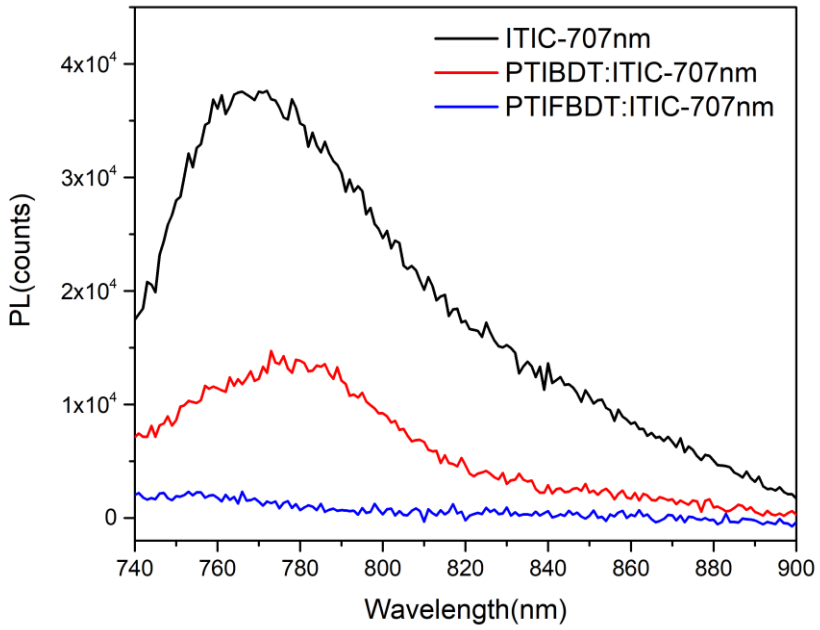

Figure 2-15 Photoluminescence spectra of neat film of ITIC and blend films of PTIBDT: ITIC, PTIFBDT: ITIC when excitation wavelength is 707nm.

The commonly used commercial NFA, ITIC, was blended with both donor polymers to function as active layers in an inverted OSC device with the structure as shown in **Figure 2-16 (a)** where the scheme of ITO/ZnO/Active layer/MoO_3/Ag is employed. The energy diagrams of two donor polymers and ITIC are also indicated in **Figure 2-16 (b)**, and the offset of HOMO levels (ΔE_{HOMO}) between PTIBDT & PTIFBDT and ITIC has been determined to be 0.18eV and 0.17eV, respectively. The ΔE_{HOMO} values are much smaller than the 0.3eV offset which has long been considered as the limitation of energy level offset to provide enough driving force for the excitons to dissociate effectively. [27,85,86] Recently, some researches have reported highly efficient NFA-based OSC systems exceeding PCE of 16% [87] with $\Delta E_{HOMO} < 0.3$eV whereas fast charge separation could still be maintained attracting more and more attention to study this phenomenon theoretically.

For instance, Hou et. al suggest that an intermolecular electric field (IEF) facilitating the charge separation will be formed since there is difference between the donor and acceptor in electrostatic potential (ESP) . [88] Consequently, it's possible to match donor and acceptor materials at very small HOMO offset to pursue higher V_{oc} and lower E_{loss} maintaining efficient charge carrier separation and transport simultaneously to get better photovoltaic performances.

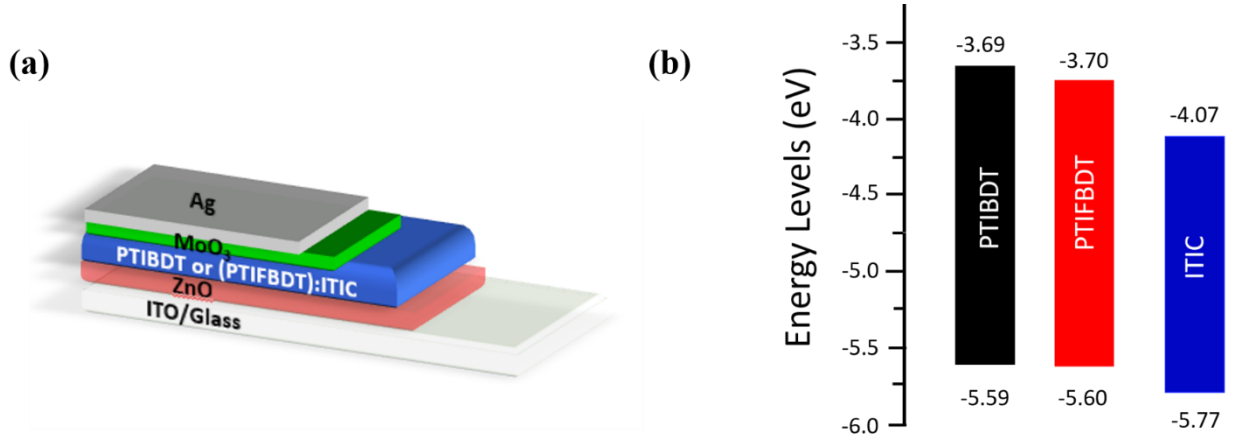

Figure 2-16 (a) Illustration of inverted OSC device structure, and **(b)** energy levels for PTIBDT, PTIFBDT and ITIC.

The optimized condition to fabricate OSC devices was to spin-coat the active layers of PTIBDT:ITIC and PTIFBDT:ITIC in 1.5:1 (D/A) ratio when chlorobenzene was applied as solvent to process D/A mixture (20mg/mL) at 1200 rpm. The photovoltaic performances with different donor polymers under different conditions are summarized in **Table 2-3,** and the current density-voltage (J-V) characteristics obtained with light illumination of AM 1.5G (100mW cm^{-2}) were shown in **Figure 2-17(a)**. Obviously, both donor polymers demonstrated excellent photovoltaic properties with PTIBDT achieving the highest PCE of 8% (J_{sc}=15.60mA/cm^2, V_{oc}=0.97V, FF=60%) and PTIFBDT achieving its best PCE of 7.70% (J_{sc}=13.70mA/cm^2, V_{oc}=1.00V,

FF=59%) when ITIC was used as acceptor at room temperature. The average PCE values of PTIBDT:ITIC and PTIFBDT:ITIC systems were investigated to be 7.50% and 7.60%, respectively. Both donor polymers have showed comparable current density and improved V_{oc} which is up to 1V for PTIFBDT:ITIC system compared with previously reported PTIBT showing a low V_{oc} of 0.66 V which indeed consists with the expected results since the unique Type II D-A copolymers can effectively broaden the π-conjugation of the polymer chains enhancing light absorption and thus lead to enhanced photocurrent response and low-lying HOMO levels which will contribute to higher V_{oc} values. Both systems demonstrated even decreased PCE results at annealing temperature at 100℃ which was due to the highly amorphous and disordered properties of the donor polymers containing regioradom distribution of isomeric sidechains as discussed previously. Annealing at high temperature could not promote the formation of organized crystalline domains which are beneficial for the transport of charge carriers, and as a result, the polymers showed less improved hole mobilities as indicated in OEFT relating part as well as decreased PCE values in OPV devices.

Table 2-4 Summary of OSC devices performance of PTIBDT:ITIC and PTIFBDT:ITIC

Active layer	D/A ratio	Solvent	Annealing temperature (℃)	Jsc (mA/cm^2)	Voc (V)	FF (%)	PCE (%)
PTIBDT:ITIC	1:1	CB	RT	13.91	0.96	56	7.52%
PTIBDT:ITIC	1.5:1	CB	RT	15.60	0.97	60	8.00%
PTIBDT:ITIC	1.5:1	CB	100	13.53	0.96	56	7.23%
PTIFBDT:ITIC	1:1	CB	RT	13.38	1.00	53	7.11%
PTIFBDT:ITIC	1.5:1	CB	RT	13.70	1.00	59	7.70%
PTIFBDT:ITIC	1.5:1	CB	100	13.25	0.97	56	7.30%

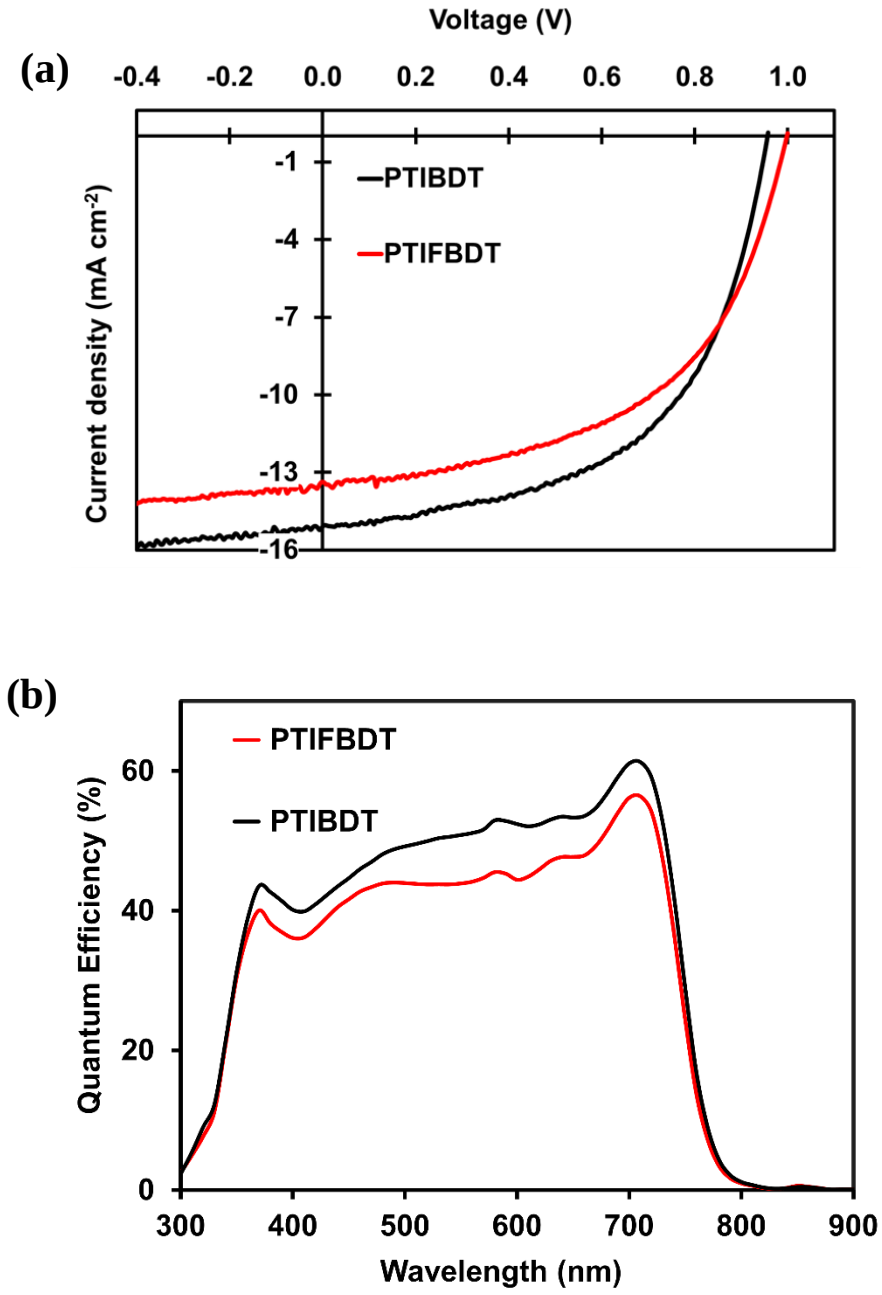

Figure 2-17 (a) Current density-voltage (J-V) curves of OSCs, **(b)** External quantum efficiencies of PTIBDT:ITIC and PTIFBDT:ITIC blends.

The external quantum efficiencies profiles for two systems are shown in **Figure 2-17 (b).** Both blend films showed high and flat EQE response covering the wavelength range of 300-800nm

especially exhibiting a sharp peak at around 350 nm consistent with the sharp light absorption peak at low wavelength region measured in UV-vis spectra demonstrating efficient charge carrier generation and transport which indicated improved involvement of photons absorbed from short-wavelength region in the photocurrent generation process. Compared with PTIBDT based system, PTIFBDT based system has shown slightly lower current density which could be attributed to the less miscible film morphology of PTIFBDT:ITIC blend film which will be discussed later.

To further understand the charge transport in the blend films, the vertical charge mobilities of PTIBDT:ITIC and PTIFBDT:ITIC blend films were measured and determined by the space-charge-limited current (SCLC) technique. As shown in **Figure 2-18**, the hole-only device was in the layer sequence of ITO/ZnO/Active layer/LiF/Al, and the electron-only device was in the structure of ITO/PEDOT:PSS/Active layer/MoO_3/Ag. The charge carrier mobilities can be calculated through extracting the quadratic region from the J-V curves according to the Mott-Gurney equation:

$$J = \frac{9}{8}\mu\varepsilon\varepsilon_0\frac{V^2}{L^3}$$

where J represents the current density, ε means the dielectric constant which is approximately 3 for organic conductors, ε_0 is the vaccum dielectric constant, V is the corresponding volatage, and L is the thickness of the active layer.

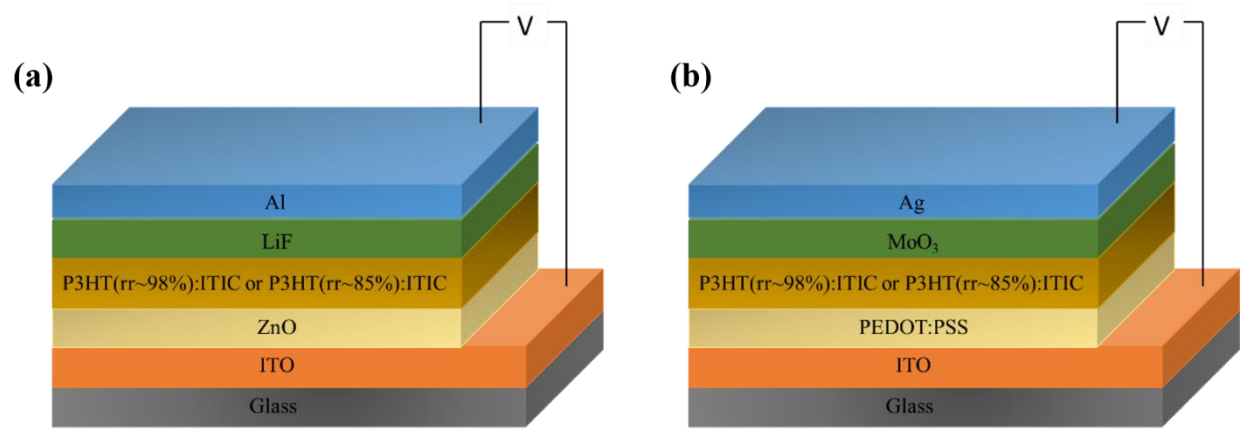

Figure 2-18 Schematic of hole-only device **(a)** and electron-only device **(b)** for SCLC measurement.[89]

The SCLC results showed that the hole mobiltis (μ_h) for PTIBDT:ITIC and PTIFBDT:ITIC blend films were 6.31×10^{-5} and 1.40×10^{-4} $cm^2 V^{-1} S^{-1}$, respectively, and the electron mobilities (μ_e) for them were estimated to be 6.56×10^{-5} and 1.47×10^{-4} $cm^2 V^{-1} S^{-1}$ as shown in **Figure 2-19**. Both blend films demonstrated favoured hole/electron mobilities which were relatively balanced with the μ_h /μ_e ratio to be 0.96 for PTIBDT system and 0.95 for PTIFBDT system that should be advantageous for a high V_{oc} and FF value agreed with the crucial requirement for high performance OSC devices to achieve a highly balanced ratio of charge carriers mobilities which should be close to unity to enhance the effective collection of photocurrent. [90] Compared with PTIBDT system, PTIFBDT one has shown an order higher magnitude hole and electron mobilities revealing its better charge transport property which can effectively prevent the accumulation of charges and thus improve V_{oc} and FF values.

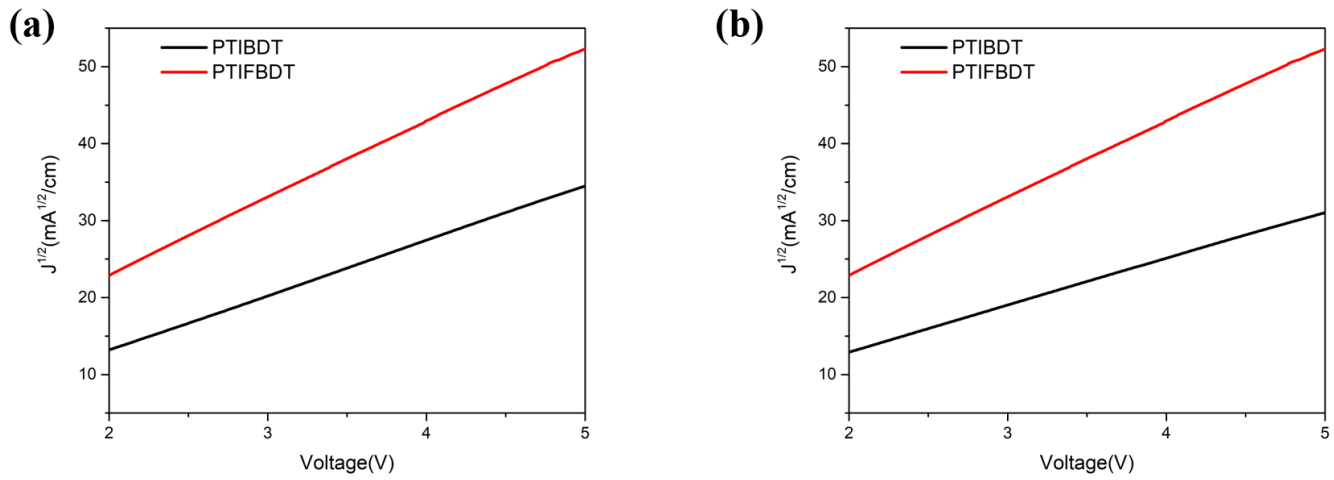

Figure 2-19 Current density-voltage (J-V) curves of **(a)** hole-only device and **(b)** electron-only device of PTIBDT and PTIFBDT.

The photovoltaic performances of OSC devices are be affected by the morphology of donor polymer and NFA blend films. Therefore, the crystallinity of polymers and morphology of blend films were carefully investigated with X-ray diffraction (XRD) to get XRD patterns and atomic force microscopy (AFM) to detect the film morphology. As shown in **Figure 2-20**, both PTIBDT:ITIC and PTIFBDT:ITIC blend films demonstrated relatively smooth morphology with small crystalline domains and low surface roughness with the root-mean-square (RMS) value of only 0.4nm for PTIBDT:ITIC and 0.97nm for PTIFBDT:ITIC. Noticeably, PTIBDT :ITIC blend film formed better continuous interpenetrating networks with smaller domains compared with PTIFBDT which should be favorable for the charge carrier separation and transport due to more available donor/acceptor interfaces resulting in higher current density (J_{sc}) which could partially explain the slightly higher J_{sc} of PTIBDT based system. [91,92] However, although the very homogeneously mixed film morphology for both donor polymers based systems can enhance the charge generation since the formation of large area of D/A interfaces for the excitons to dissociate,

the low crystallinity and very fine phase separation will cause more serious germinate recombination not favored for the exciton diffusion and charge carriers transport and therefore account for the limited J_{sc} and FF results of both donor polymers based OSC devices. [93,94]

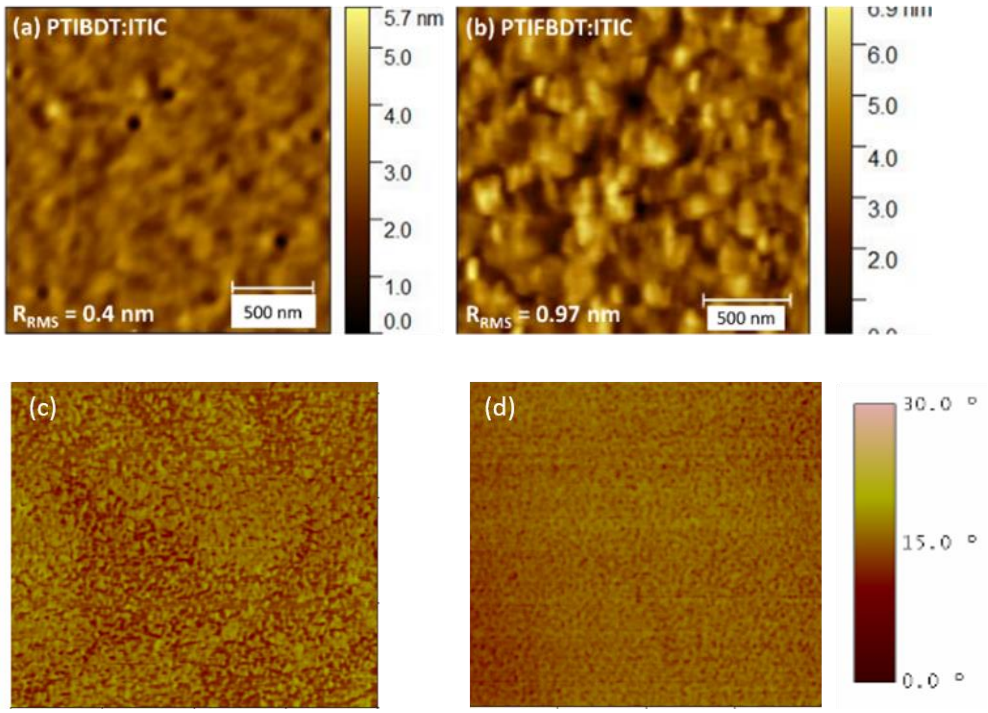

Figure 2-20 AFM height [(**a**) and (**b**)] and phase [(**c**) and (**d**)] images of PTIBDT:ITIC and PTIFBDT:ITIC blend films.

The very amorphous properties of PTIBDT and PTIFBDT polymers were simultaneously revealed by their two-dimensional grazing-incidence X-ray diffraction (2D-GIXD) patterns which were obtained by measuring the pristine polymer flaxes as shown in **Figure 2-21**. Both polymers demonstrated a weak and broad (100) diffraction peak at 2θ= ~4.2 ° for PTIBDT and 2θ= ~4.5 ° for PTIFBDT, and this diffraction peak determined the corresponding lamellar d-spacing which represented the separation distance of polymer backbones due to the existence of side chains, and the d-spacing was determined to be 2.1nm for PTIBDT and 1.96 for PTIFBDT demonstrating their similar interlamellar packing ordering. PTIBDT polymer showed slightly higher diffraction

intensity which meant the improved crystallinity compared with PTIFBDT polymer. Due to the very low crystallinity of two polymers, there was no π-π stacking peak could be observed. This superior low crystallinity should result from the highly regiorandom (Z/E) side chain distribution of polymer chains which hinders the free carriers generation and transport and hence cause low J_{sc} and FF values.

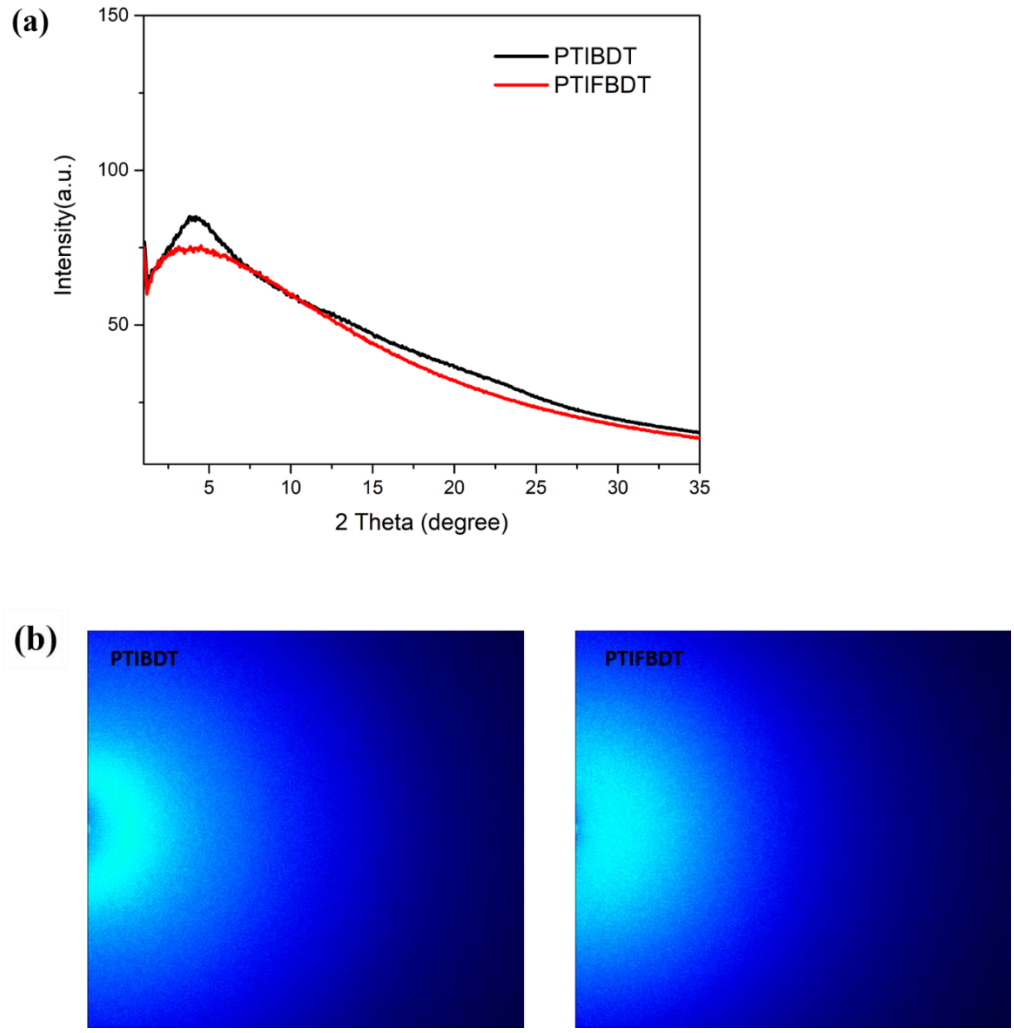

Figure 2-21 (a) Out of plane line cutting of GIXD patterns and **(b)** images of PTIBDT and PTIFBDT films.

2.6 Summary and Future directions

In conclusion, two Type II donor-acceptor copolymers including PTIBDT and its fluorinated counterpart PTIFBDT with 2-dimentional BDT-T as donor backbone and indolin-2-one as acceptor side chain were successfully designed and synthesized via simple synthetic routes which also indicated the low cost of these donor polymers. Both novel polymers demonstrated wide optical band gaps achieving fully complementary light harvesting to enhance high J_{sc} and deep-lying HOMO levels which could effectively increase V_{oc} resulting in improved photovoltaic performances when ITIC was used as acceptor. PTIBDT:ITIC blend film achieved the highest PCE of 8% , and PTIFBDT:ITIC blend got a comparable PCE of 7.7% and showed the best V_{oc} which was up to 1V. The photovoltaic results showed the polymers can be promising donor materials with low synthetic costs and comparable high OPV performances compared with current high-performance donor polymers synthesized via tedious routes.

For the future work, both PTIBDT and PTIFBDT based devices were found to be restricted from further PCE improvement by the limited J_{sc} and FF values that could be attributed to the low crystallinity of PTIBDT and PTIFBDT polymers, and this highly amorphous property should be related with the disordered side chains with both Z/E configurations. Moreover, the PLQE results revealed that the hole carrier generation was not favored with low ITIC quenching efficiency of PTIBDT:ITIC film. Consequently, it might be helpful to change the NFA material from ITIC to some recently published NFA molecules such as Y6, which typically enhances the J_{sc} value and maintains efficient exciton generation at small HOMO level offset. [40] In addition, introduction of solvent additives with a high-boiling point involving 1,8-diiodooctane (DIO) might be effective method to further enhance PCE results with improved J_{sc} and FF due to the optimization of morphology and improved charge transport. [95]

2.7 Experimental Section

Materials and Characterization

All solvents and chemicals were provided by commercial suppliers such as Sigma-Aldrich and were directly applied without purification. Density functional theory (DFT) simulations were calculated by Gaussian 09 software at the B3LYP level with 6-31G (d) basis set. High-temperature gel permeation chromatography (HT-GPC) analyses were measured on Agilent PL-GPC220 using 1,2,4-triclorobenzene as eluent at column temperature of 110℃ with polystyrene used as the standard. Thermogravimetric analyses (TGAs) and differential scanning calorimetry (DSC) data were obtained with TA Instruments SDT 2960 at a heating rate of 10 and 5 ℃ min^{-1} under protection of nitrogen flow. CV measurements were conducted on a CHI600E electrochemical analyzer with an Ag/AgCl as reference electrode. Two Pt disk electrodes functioned as the counter electrode and working electrode which was coated by the polymer film in 0.1M tetrabutylammonium hexafluorophosphate solution in acetonitrile at a scan rate of 100 mV s-1. Ferrocene which has a HOMO level of 4.8eV was used as reference. The UV-vis absorption spectra of polymers were acquired by Cary 7000 Universal Measurement Spectrophotometer (UMS). Two-dimensional grazing-incidence X-ray diffraction (2D-GIXD) patterns were obtained with a Bruker D8 Discover powder diffractometer using geometry with Cu Kα radiation (λ= 0.15418 nm) in standard Bragg-Bretano geometry. Atomic force microscopy (AFM) images were characterized by Digital Instruments Dimension 3100 Nanoman Nanoscope IV microscope. Photoluminescence (PL) spectra were recorded on Horiba PTI QuantaMasterTM 8000 Series Fluorimeter**.**

Fabrication and Characterization of OFET Devices

The charge carrier mobility of polymers was measured by OFET device in a bottom-gate bottom-contact (BGBG) configuration. The fabrication and preparation of OFET devices was as followed: the gold contacts including source and drain were deposited on a SiO2/Si substrate through conventional photolithography and thermal deposition where the heavily p-doped p+-Si wafer was employed as the gate electrode, and the 300nm thickness of SiO2 layer which was thermally grown was used as the insulating dielectric. The prepared wafers were then cut into small pieces containing several transistor pairs and sonicated by acetone and followed isopropanol (IPA) in an ultrasonic bath for 20 min respectively, which were then treated by oxygen plasma. After that, the cleaned wafers were soaked in dodecyltrichlorosilane (DDTS) solution (3% DDTS in toluene) for 20 min and washed by toluene followed by drying under nitrogen flow. The polymer film was then formed on the wafer substrate via the spin-coating method at 3000rpm for 60s using a polymer solution in chloroform with the concentration of 5mg/ml, and the fabricated device was then thermal annealed at various temperatures for 20 min under argon environment inside a glove box. The fabricated OFETs had a channel width (*W)* of 30 um and a channel length (*L*) of 1000 um and were characterized by an Agilent B2902A Semiconductor Analyzer inside the same glove box.

Fabrication and Characterization of Organic Solar Cells (OSCs)

Organic solar cell devices of inverted configuration were fabricated with ITO/ZnO/Active layer/MoO3/Ag as indicated in **Figure 2-13 (a).** Firstly, the ITO glass substrates were immersed and cleaned by sonification in deionized water (DI water), acetone, and IPA for 20 min, respectively. Then the substrates were dried using nitrogen flow and treated by oxygen plasma cleaning for 10 min. Subsequently, a layer of ZnO (~40nm) was coated on the substrate via Spin-coating method at rpm of 4000, and the devices were then dried at 200°C for 1 hr in air. Then the prepared substrates were moved into glove box in nitrogen environment, and an active layer (D/A

blend) was sin-coated on the substrate using the solution of donor polymer and ITIC. The fabricated devices with films were dried in the vacuum overnight. Finally, the top electrode compris a layer of MoO3 (~7nm) and Ag (~120nm) was evaporated in the presence of about 5 × 10^{-7} mbar vacuum in thermal process and deposited onto the substrate. The current density–voltage (J-V) performances of the organic solar cells were characterized on an Agilent B2912A Semiconductor Analyser with a Science Tech SLB300-A Solar Simulator. The light source was A 450 W xenon lamp with an air mass (AM) 1.5 filter.

Synthesis Procedures

Synthesis of 2,5-dibromothiophene-3-carbaldehyde

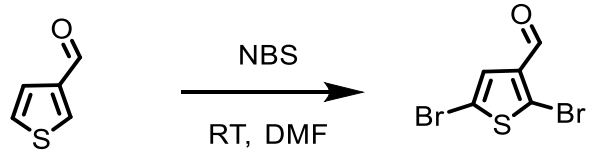

This compound was synthesized following the method reported by literature:

3-thiophenecarboxaldehyde (9 g, 80.25 mmol) was added to a 250 mL one-neck round bottom flask. Then 120 mL dimethyl formamide (DMF) was added to dissolve the solid. N-bromosuccinimide (NBS) (45.71 g, 256.81mmol) was then charged to the reactor as solution in 100mL DMF dropwise, and the reaction mixture was kept stirred for 48 hrs in the dark at room temperature. The reaction mixture was then washed with water and extracted by diethyl ether. The organic layer was collected and was dried using anhydrous sodium sulfate (Na2SO4), and the solvent was evaporated by rotary evaporator under reduced pressure to give crude solid. The crude product was further purified by column chromatography by column chromatography on silica gel using the eluent of 1: 3 dichloromethane and hexane. to give the pure product as yellow solid. (yield: 15.16g, 70%) 1H NMR (300 MHz, CDCl3, ppm) δ: 9.80 (s, 1H), 7.34 (s, 1H).

Synthesis of (Z)-3-((2,5-dibromothiophen-3-yl) methylene)-1-methylindolin-2-one (M1).

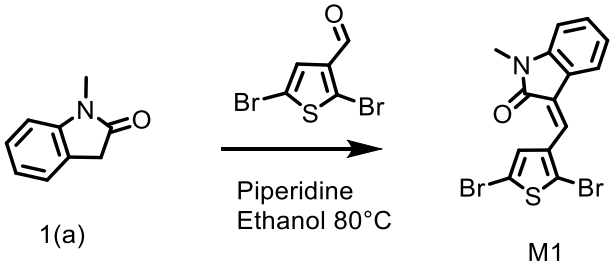

2,5-Dibromothiophene-3-carbaldehyde (0.473g, 1.754mmol) and 1-methyl-2-oxindole (0.258g, 1.754mmol) were added to a 25mL two-neck round bottom flask, and the reactor was purged for three times with nitrogen. Absolute ethanol (12mL) was injected via a syringe, and piperidine(0.234mL) was then added. The reaction mixture was refluxed overnight under nitrogen, and orange solid precipitate out from the solvent. After cooled down to room temperature, the crude solid was collected by filtration and then washed with ethanol (3×5mL) then dried under vacuum to obtain the product as yellow solid. (yield: 0.443g, 43%) 1H NMR (300 MHz, CDCl3, δ/ppm): 8.75 (s, 1H), 7.56-7.53 (d, J = 9Hz, 1H), 7.40 (s, 1H), 7.33-7.28 (t, J = 6Hz, 1H), 7.09-7.04 (t, J = 6Hz, 1H), 6.83-6.80 (d, J = 9Hz, 1H), 3.27 (s, 3H).

Synthesis of (Z)-3-((2,5-dibromothiophen-3-yl) methylene)-5-fluoroindolin-2-one (2).

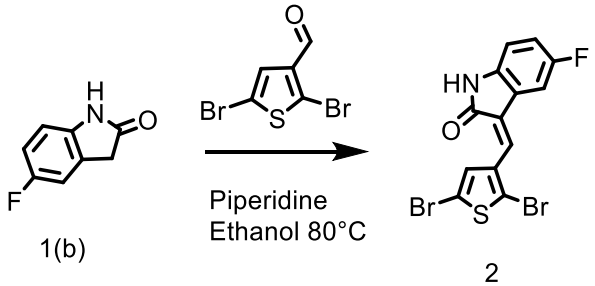

2,5-Dibromothiophene-3-carbaldehyde(0.335g, 1.24mmol) and 5-fluorooxindole (0.187g, 1.24mmol) were added to a 25mL dry two-neck round bottom flask, and the reactor was purged for three times with nitrogen. Anhydrous ethanol (9 mL) was injected via a syringe, and piperidine

(0.165mL) was then added. The mixture changed color to yellow immediately when piperidine was added. The reaction mixture was then refluxed overnight under nitrogen protection. Orange solid precipitate out from the solvent after overnight refluxing. The solid was collected by filtration and then washed with methanol (3×5mL) then dried under vacuum to give the crude orange product. (yield: 0.41g, 81%) Due to the poor solubility of this compound 2, the crude solid was directly applied in the next step.

Synthesis of (Z)-3-((2,5-dibromothiophen-3-yl) methylene)-5-fluoro-1-methylindolin-2-one (M2).

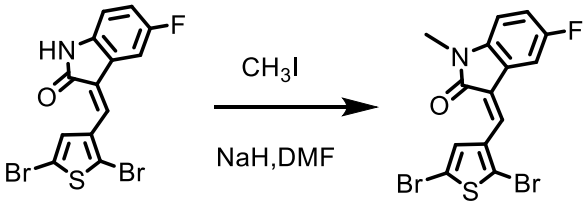

2 M2

Compound 2 (0.174g, 0.432mmo, 1 equal) and sodium hydride (0.052g, 2.16mmol, 5 equal) were added to a 25mL dry two-neck round bottom flask, and the reactor was purged for three times with nitrogen. Anhydrous DMF (6mL) was injected, and iodomethane (0.0797g, 0.562mmol, 1.3 equal) was added dropwise in ice bath. The mixture was kept stirred for half an hour at 0℃, and was then warmed to room temperature and poured to 200mL DI water. The desired product was extracted by ethyl acetate and washed by DI water and brine for three times. The organic layer was collected and dried by anhydrous sodium sulfate (Na2SO4) and then the solvent was removed under reduced pressure to give the crude product. The obtained solid was further purified by column chromatography on silica gel using the eluent of 1: 9 ethyl acetate and hexane. (yield: 0.14g, 68%) 1H NMR (300 MHz, CDCl3, δ/ppm): 8.77 (s, 1H), 7.36 (s, 1H), 7.27 (s, 1H), 7.04-6.98 (m, 1H), 6.74-6.71 (m, 1H), 3.26 (s, 3H).

Synthesis of polymer PTIBDT

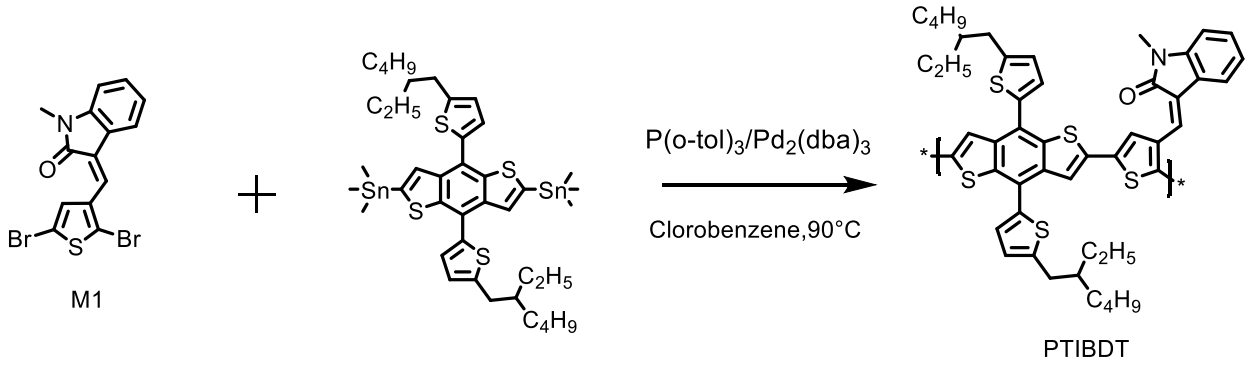

M1 (0.0734g, 0.184mmol, 1.0 eq.), BDT (0.166 g, 0.184 mmol, 1.0 eq.) and tri(*o*-tolyl)phosphine (P(o-tol)3) (0.00447g, 0.0147mmol, 0.08 eq.) were added to a 25 mL dry two-neck round bottom flask connecting with a water condenser, and the reactor was purged for three times with argon. Anhydrous chlorobenzene (4 mL) was firstly injected to the reactor via a syringe to dissolve the solid, and subsequently tris(dibenzylideneacetone)dipalladium (Pd2(dba)3) (0.00337g, 0.00368 mmol, 0.02 eq.) was added as solution in 0.5mL of anhydrous chlorobenzene. The temperature was then heated to 90℃, and the reaction mixture was then stirred for 18 hrs under argon protection. The reaction solution was then cooled down to room temperature and poured into 150mL stirring methanol. The crude solid was filtered and washed by methanol, dried and lastly purified via Soxhlet extraction with the solvents of acetone, hexane and chloroform. A dark black film was yielded upon removal of the chloroform. (yield: 0.135g, 90%)

Synthesis of polymer PTIFBDT

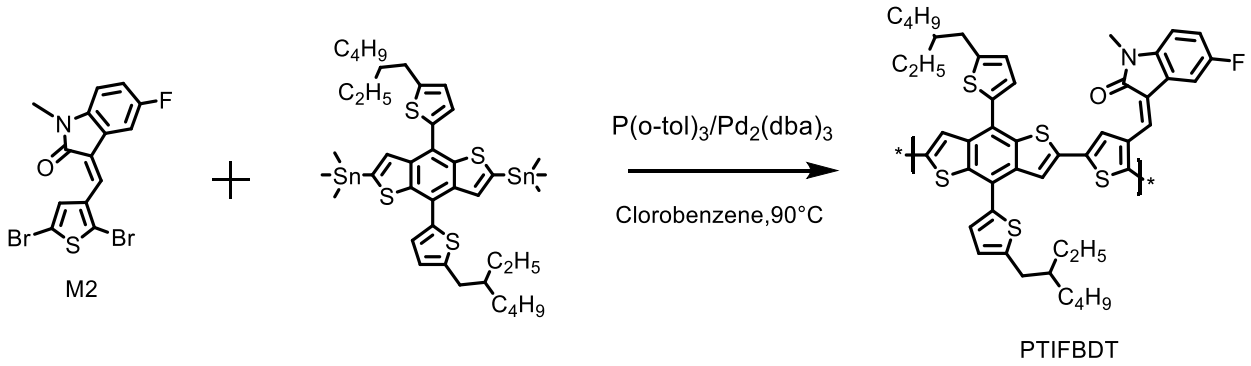

M2 (0.0427g, 0.1024mmol, 1.0 eq.), BDT(0.0926g, 0.1024mmol, 1.0 eq.) and tri(*o*-tolyl)phosphine (P(o-tol)3) (0.0025g, 0.00819mmol, 0.08 eq.) was added to a 25 mL dry two-neck round bottom flask connecting with a water condenser, and the reactor was purged for three times with argon. Anhydrous chlorobenzene (3.5 mL) was firstly injected to the reactor via a syringe to dissolve the solid, and subsequently tris(dibenzylideneacetone)dipalladium (Pd2(dba)3) (0.00187g, 0.00205 mmol, 0.02 eq.) was added as solution in 0.7mL anhydrous chlorobenzene. The temperature was then heated to 90℃, and the reaction mixture was then stirred for 18 hrs under argon protection. The reaction solution was then cooled down to room temperature and poured into 150mL stirring methanol. The crude solid was filtered and washed by methanol, dried and lastly purified via Soxhlet extraction with the solvents of acetone, hexane and chloroformA dark black film was yielded upon removal of the chloroform. (yield: 0.0714g, 82%).

Chapter 3 Synthesis and Characterization of PTIABDT and PTIPBDT

3.1 Introduction

In chapter 2, two Type II D-A copolymers comprised of benzo[1,2-b:4,5-b0]dithiophene (BDT) donor backbone and indolin-2-one acceptor side-chain have been successfully synthesized and characterized by several techniques to demonstrate wide optical bandgaps and deep-lying HOMO levels as promising donor materials when matched with commonly used NFA, ITIC. Interestingly, it was found that the introduction of fluorine atom to the indolin-2-one side-chain had shown very little influence on the optical bandgap as well as energy levels resulting in similar properties for both polymer with or without fluorination, and more importantly, the fluorinated polymer, PTIFBDT, still exhibits very large threshold voltage (V_{th}) in OFET devices indicating serious hole trapping problem induced by the electron-rich nitrogen atom in indolin-2-one unit which should limit the OPV performance. Consequently, in this chapter, another strong electron-withdrawing carbonyl group will be directly introduced to the nitrogen atom of indolin-2-one side-chain aiming at further decreasing the number of hole traps and thus presuming better photovoltaic performance when the new donor polymers are applied in OSC devices.

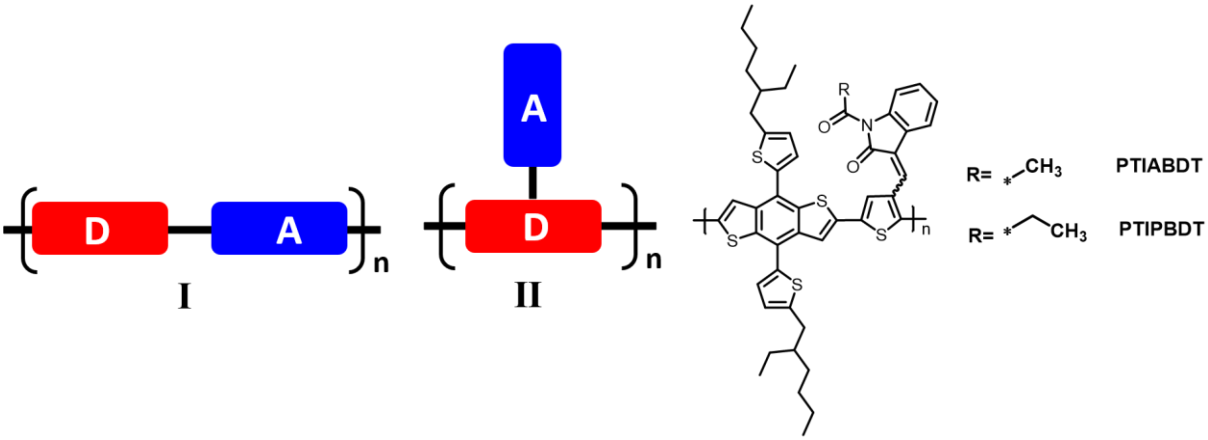

Figure 3-1 Structures of Type I, Type II D-A copolymer and PTIABDT, PTIPBDT polymer.

As shown in **Figure 3-1**, two carbonylated polymers including PTIABDT with acetyl group introduced and PTIPBDT with propionyl group introduced were designed and synthesized via simple synthetic steps, and the different alkyl chain length can modulate the solubility of resulted polymers which will be discussed later. It has been investigated that the introduced carbonyl group onto electron-deficient units can significantly decrease the HOMO level of the resulting donor polymers without influence on the bandgap.[68] Hou et. al [96] reported the substitution of ester group with ketone group to give thieno-[3,4-b]thiophene (TT-C) unit which was substituted with alkylcarbonyl group and copolymerized with BDT yielding the polymer PBDTTT-C which achieved lower HOMO level and increased V_{oc} as shown in **Figure 3-2**. Then the alkoxy group on BDT unit in PBDTTT-C was further replaced with alkylthienyl group to form 2D conjugated copolymer, PBDTTT-C-T, (**Figure 3-2**) which demonstrated even lower HOMO, enhanced hole mobility and improved photovoltaic properties. [68] In addition, although fluorination has been commonly adopted as effective approach to decrease the HOMO level, it takes quite tedious and costly procedures to synthesize, [97] thus carbonylation can be alternative effective method with lower cost to achieve lower-lying HOMO level. [96]

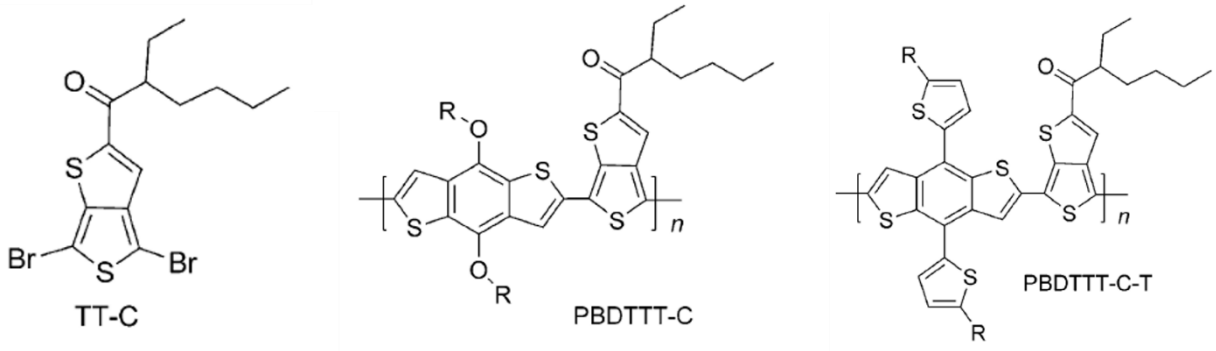

Figure 3-2 Structures of TT-C, PBDTTT-C and PBDTTT-C-T.

3.2 Structure Simulation by Density Functional Theory (DFT)

Density functional theory (DFT) simulation was firstly performed to simulate the donor polymer structure via Gaussian 09 software at the B3LYP/6-31(d) level to predict the optimized geometry and energy levels. Since PTIPBDT is a counterpart of PTIABDT polymer with a longer propyl chain aiming to improve the polymer solubility, and the long alkyl side chain is commonly abbreviated as a short methyl group in DFT calculation so that the one repeating unit TIABDT with one acetyl group introduced was simulated to represent both PTIABDT and PTIPBDT. Very similarly with PTIBDT and PTIFBDT polymers discussed in Chapter 2, it is also highly possible for the TIABDT repeating unit to form both Z and E configurations due to the rotation of the vinylene linkage between BDT and indolin-2-one, so Z- and E-isomers were simultaneously simulated as shown in **Figure 3-3**.

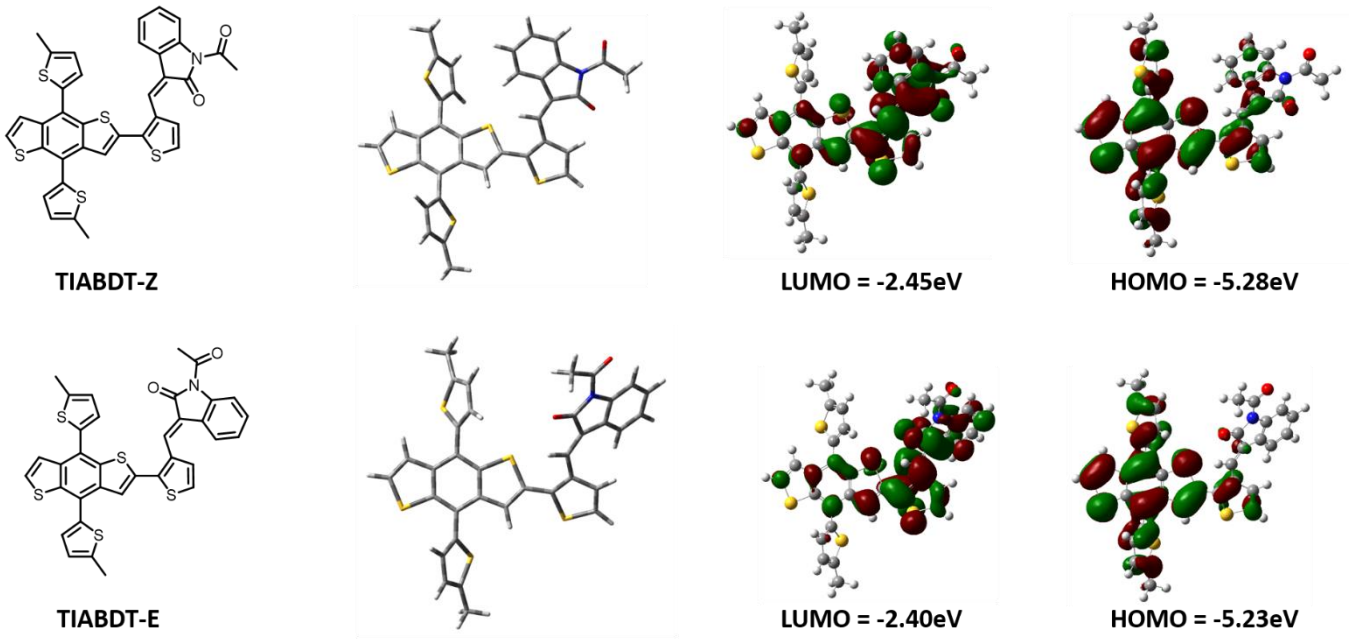

Figure 3-3 Optimized geometries of PTIABDT and PTIPBDT and predicted energy levels in different configurations.

According to the optimized frontier energy levels, carbonylation can further decrease the energy levels with the Z-isomer possessing the lowest simulated HOMO level of -5.28eV in this series of Type II D-A copolymers including PTIBT, PTIBDT and PTIFBDT. The HOMO level was shown to be downshifted by 0.12eV for Z-isomer and 0.13eV for E-isomer when compared with the repeating unit TIBDT of PTIBDT polymer, and fluorination was shown to lower the HOMO level of PTIBDT by 0.06eV for Z-isomer and 0.05eV for E-isomer in theory as discussed in Chapter 2 illustrating the enhanced electron-withdrawing effect of the introduced carbonyl group in Type II D-A polymer structure. In addition, the charge distributions showed the very delocalized LUMO on the acceptor part and delocalized HOMO on the donor backbone especially for E-isomer due to the strong push-pull effect in this kind of structure where BDT functions as donor backbone with indolin-2-one as acceptor side chain and the strong electron-withdrawing property of the introduced carbonyl group.

3.3 Synthesis of Monomers and Polymers

PTIABDT and PTIPBDT polymers were developed with introduction of acetyl group and propionyl group on the indolin-2-one, respectively, and the monomers and polymers can be simply synthesized via a few steps according to the synthetic routes as indicated in **Figure 3-4**. The monomer M1 for PTIABDT and the key intermediate 2 for PTIPBDT were simply prepared by Knoevenagel condensation reaction between N-acetyl-2-oxindole & indolin-2one and 2,5 dibromothiophene-3-carbaldehyde using piperidine as the catalyst with absolute alcohol as solvent following reported literature method. [78] The crude product precipitated out from the solvent when the reaction mixture was cooled down to room temperature and washed with methanol to obtain the pure compound. The monomer M2 for PTIPBDT was further synthesized by attachment of

propionyl group on the nitrogen atom of indolin-2one unit via refluxing in the propionyl anhydride liquid, and the crude product was purified by column chromatography to give the final monomer.[98]

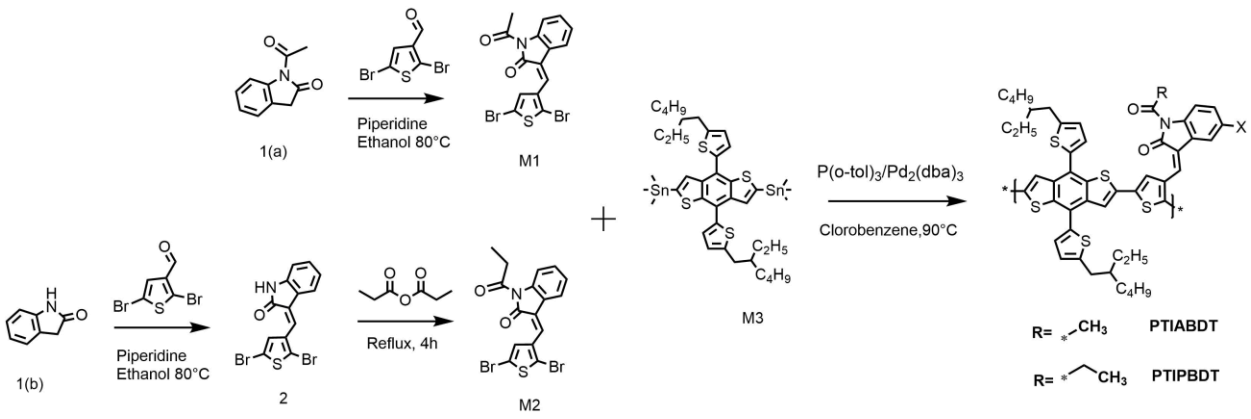

Figure 3-4 The synthetic routes to PTIABDT and PTIPBDT.

The structures of the monomers were carefully investigated by ^{1}H-NMR, and it was found that M1 only demonstrated isomer in Z-configuration according to its ^{1}H-NMR spectrum since the proton peak that was located at 8.42ppm was assigned to the special hydrogen bond that was formed between the 2-position carbonyl group on the indolin-2-one unit and the 4-position hydrogen on the thiophene unit as shown in **Figure 3-5** which is consistent with the Z-only configurational monomers for PTIBDT and PTIFBDT as discussed in the last chapter. Indeed, we proposed one hypothesis for this configurational stability of this series monomers that is the short methyl alkyl chain could effectively prevent the vinylene from rotating which leads to the formation of both Z/E isomers. Interestingly, the monomer for PTIPBDT, M2, was investigated to form both Z/E isomers in the ratio of 43:27 (Z:E isomer) after the column chromatography purification, and the ^{1}H-NMR data in **Figure 3-5** showed that the Z-isomer also formed the hydrogen bond which showed larger chemical shift (δ) to 8.41ppm with a single peak whereas the E-isomer demonstrated a smaller δ with a split doublet peak due to the effect from the hydrogens on indolin-2-one benzene

ring. Consequently, even the propionyl side chain with the extra length of one methyl group shows great influence on the configurational stability of the desired compound. It was also found that the propionyl group of M2 could be easily removed when heated at high temperature. When M2 was heated in chlorobenzene at 90℃ for 1hr, another new spot appeared in the testing thin layer chromatography (TLC) plate indicating the partial decomposition of M2 compound with the removal of propionyl groups which also affected the lateral mobility will be discussed later.

Two Type II D-A copolymers, PTIABDT and PTIPBDT, were synthesized via the Stille cross-coupling reaction as reported in literatures with two monomers of M1&M2 and BDT-2T stannane compound in 1:1 ratio in the presence of $Pd_2(dba_3)$ as catalyst, $P(o\text{-}tol)_3$ employed as ligand with chlorobenzene used as solvent. The crude dark green polymers precipitated out from methanol and were purified with acetone and hexane by Soxhlet extraction. Noticeably, PTIABDT showed poor solubility in chloroform with 92% of polymers extracted by chlorobenzene which could be due to its higher molecular weight or the strong aggregation property of the polymer. PTIPBDT polymer showed much improved solubility with 50% extracted by chloroform.

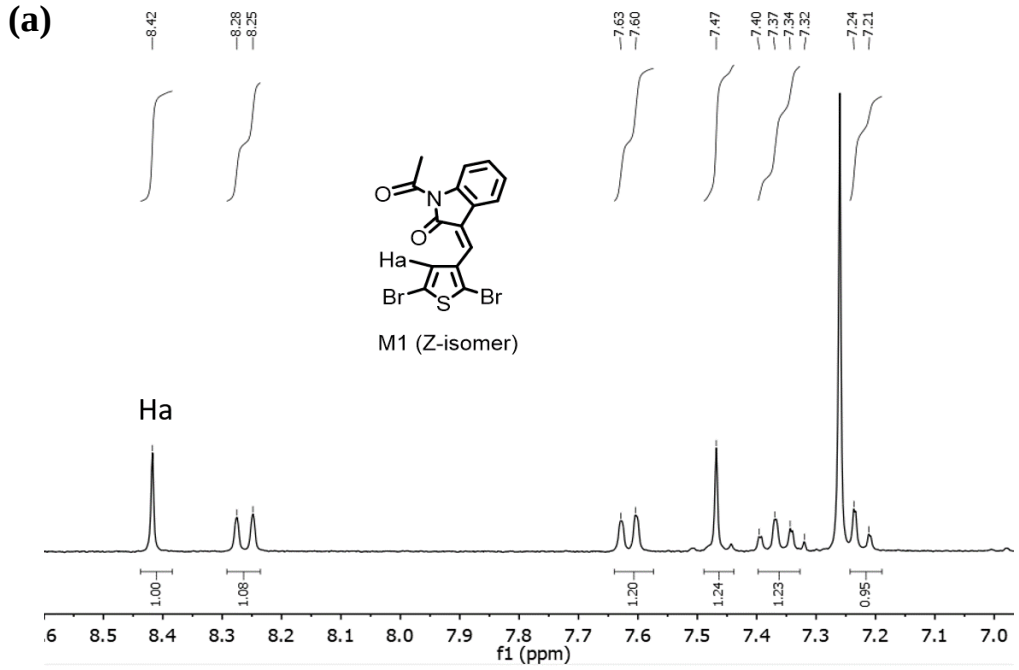

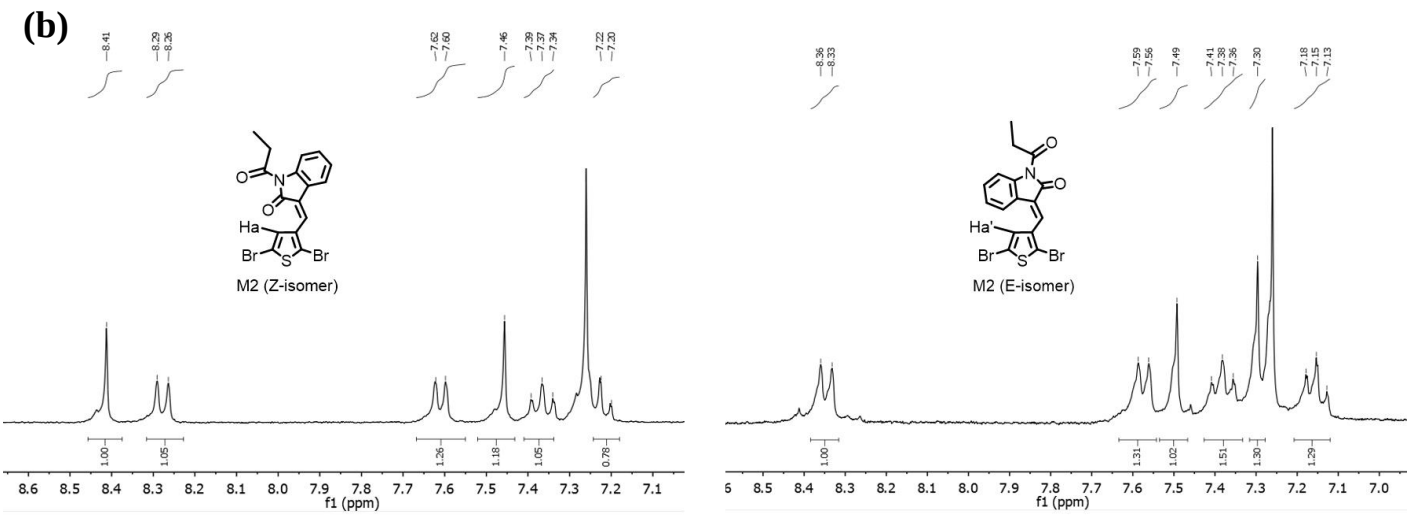

Figure 3-5 ^{1}H-NMR spectra of monomer of PTIABDT **(a)** PTIPBDT **(b)**.

3.4 Characterization of Polymers

3.4.1 Physical Properties (GPC, TGA and DSC)

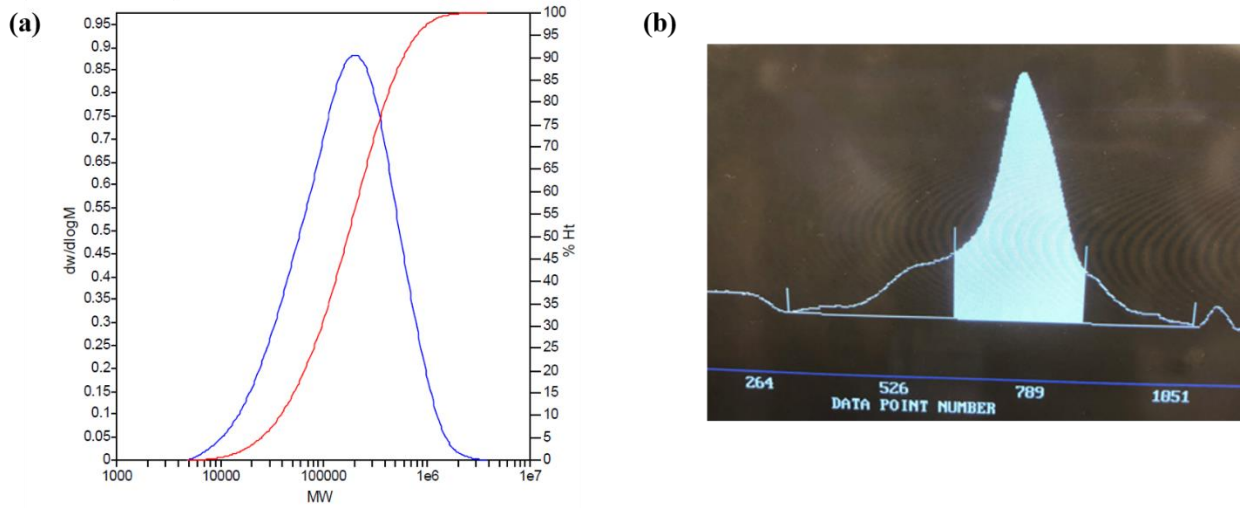

Figure 3-6 High temperature GPC molecular weight distribution for (**a**) PTIABDT measured using 1,2,4-trichlorobenzne as eluent at 110 °C with a flow rate of 1.00 mLmin^{-1} and (**b**) PTIPBDT measured using chloroform as eluent at room temperature.

The molecular weight of PTIABDT was measured by high-temperature gel permeation chromatography (HT-GPC) with 1,2,4-reichlorobene as the eluent at 110℃, and polystyrene was employed as the standard. The molecular weight of PTIPBDT was measured using chloroform as the eluent at room temperature. The number-average molecular weight (Mn) was thus determined to be 87.9 kDa and 39.6 kDa for PTIABDT and PTIPBDT, respectively. Polydispersity index (PDI) for PTIABDT and PTIPBDT were measured to be 2.91 and 2.99 where PTIABDT demonstrated superior high molecular weight which could explain its very limited solubility in common organic solvents. (**Figure 3-6**) The thermal stability of two polymers were characterized by thermal gravimetric analysis (TGA) and differential scanning calorimetry (DSC) as illustrated in **Figure 3-7**. As shown in **Figure 3-7(a)** and **Table 3-1**, PTIABDT showed 2% decomposition at 326℃, and PTIPBDT showed 1% weight loss at 170℃ for the first decomposition and 2% weight loss at 321℃ for the second decomposition. The total weight loss during the first decomposition was estimated to be 6% very close to the theoretical weight loss when the propionyl group were all removed and evaporated which was calculated to be 6.53% implying the possibility of propionyl group removal during the first decomposition process. According to the DCS data, both polymers showed very amorphous state without obvious transition peaks, and only polymer PTIABDT exhibited a very weak glass transition temperature (T_g) at 72℃. (**Table 3-1**)

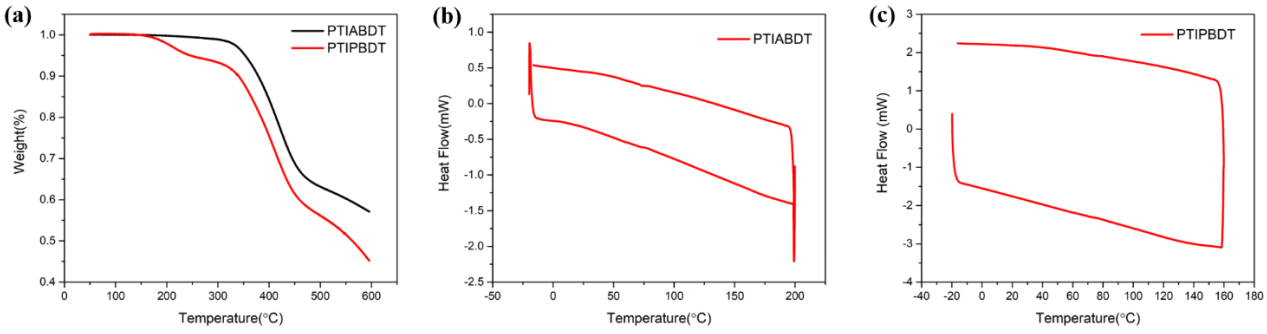

Figure 3-7 TGA **(a)** and DSC **(b, c)** curves of PTIABDT and PTIPBDT.

Table 3-1 Molecular weight and thermal properties of PTIABDT and PTIPBDT

Polymers	M_n (kDa)	M_w(kDa)	$Đ$ (M_w/M_n)	T_d ^{1st}(°C)	T_d ^{2nd}(°C)	T_g(°C)
PTIABDT	87.9	25.6	2.91	326	/	72
PTIPBDT	39.6	118.7	2.99	170	321	/

3.4.2 Optical and Electrochemical Properties (UV-vis and CV)

The UV-vis spectra of PTIABDT and PTIPBDT polymers were measured and showed in **Figure 3-7**. Both donor polymers have demonstrated broad and flat light absorption with two absorption bands involving one low energy band and a high energy one in the range of 300-700nm with similar absorption shape compared with PTIBDT and PTIFBDT polymers discussed in Chapter 2. PTIABDT film showed the absorption maximum at 576nm, and this maximum was located at 571nm for PTIPBDT film. It is worthy to notice that the two polymers showed lower band gaps which were estimated based on the onset wavelengths of the polymers film absorption spectra, and the band gap is determined to be 1.83eV for PTIABDT and 1.84eV for PTIPBDT with the slightly red shifted absorption compared with PTIBDT and PTIFBDT implying a more ordered polymer chain stacking. Meanwhile, the donor polymers also achieve complementary light absorption covering the whole visible light range (300-800nm) when blended with ITIC ensuring the enough photons absorbed to further be converted to charge carriers.

Table 3-2 Optical and electrochemical properties of PTIBDT and PTIABDT

Donor Polymers	**$\lambda_{max}^{sol.}$ (nm)**	**$\lambda_{max}^{film.}$ (nm)**	**$\lambda_{onset}^{film.}$ (nm)**	**E_g^{opt} (eV)**	**HOMO (eV)**	**LUMO (eV)**
PTIABDT	573	576	679	1.83	-5.60	-3.77
PTIPBDT	543	571	673	1.84	-5.63	-3.79

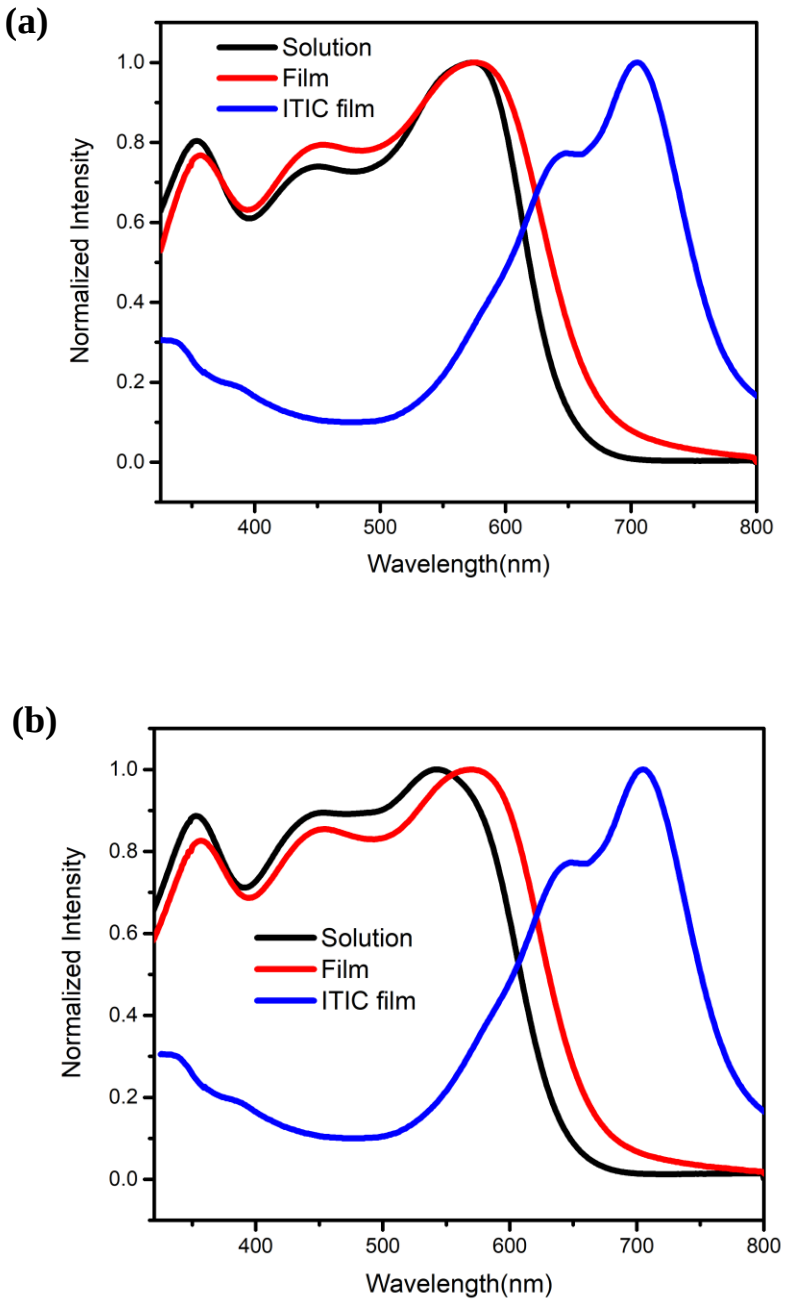

Figure 3-8 UV-vis spectra of **(a)** PTIABDT (in chlorobenzene solution and as-cast thin film at RT) and ITIC (as-cast film) **and (b)** PTIPBDT (in chloroform solution and as-cast thin film) and ITIC (as-cast film).

The energy levels of PTIABDT and PTIPBDT were measured by the cyclic voltammetry (CV), and the HOMO and corresponding LUMO levels were determined to be -5.60eV and -3.77eV for PTIABDT, and the values were -5.63eV and -3.79eV for PTIPBDT. The HOMO levels were estimated with correspondence to the oxidation potential onset obtained by CV measurement as shown in **Figure 3-9**, and corresponding LUMO levels were then deduced from optical band gap due to the absence of reduction potential in the CV measurement.

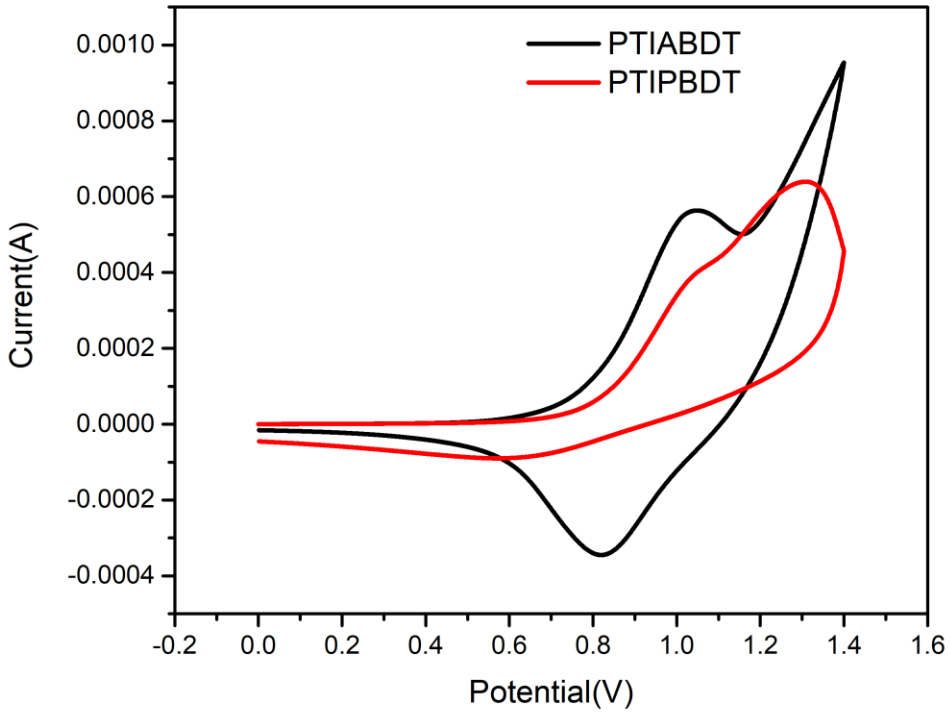

Figure 3-9 Cyclic voltammetry profiles of PTIBDT and PTIFBDT in tetrabutylammonium hexafluorophosphate acetonitrile solution (0.1M) at a scan rate of 0.1V s^{-1}.

Interestingly, it was found that PTIABDT showed the same HOMO level when compared with PTIFBDT which was only 0.01eV higher than PTIBDT although the DFT simulation results

predicting the stronger effect of carbonylation on the downshift of HOMO level compared with fluorination which could be related with the intrinsic properties of Type II D-A polymers attributed to the introduction of electron-withdrawing groups to the side chain instead of the main polymer chain. PTIPBDT with propionyl group exhibited down-shifted HOMO which was 0.03eV lower than PTIABDT polymer similar with reported conjugated polymers demonstrating slightly lower-lying HOMO levels when the length of alkyl side chain was increased. [99] In addition, it was noticed that the CV profile of PTIABDT contained the reversible current peak which was absent for PTIBDT, PTIFBDT and PTIPBDT. This appearance of reversible current was assumed to rely on the less charge trapping property of PTIABDT polymer brought by the introduction of strong electron-withdrawing carboxyl group which will also be discussed in the next OFET part.

3.4.3 Organic Field-effect Transistor (OFET) Properties

OFET devices were manufactured to determine the charge mobilities of the donor polymers via spin-coating the polymer films as active layers in BGBC configuration. The corresponding summary mobility results at different temperatures are presented in **Table 3-3** and **Figure 3-10**.

The PTIABDT polymer demonstrated much improved hole mobility up to 0.015 $cm^2V^{-1}s^{-1}$ which is one order higher in magnitude compared with the hole mobilities of PTIBDT and PTIFBDT. The much higher mobility should be due to the enhanced crystallinity which could be revealed by the XRD data discussed later. Moreover, it is investigated that the threshold voltage (V_{th}) for this polymer decreases to very small number close to zero suggesting the much improved trapping problem in the process of charge carrier transport due to the very strong electron-withdrawing property of the carbonyl group. As discussed in Chapter 2, this serious hole trapping problem can be related with the existence of free pair of electrons of nitrogen atom from indolin-2-one unit, and

the strong electron-withdrawing carbonyl group can attract the free pair of electrons and thus improve the hole trapping resulting in low V_{th}. Nevertheless, PTIPBDT exhibits lower hole mobility with the maximum value of 0.00698 $cm^2V^{-1}s^{-1}$ when annealed at 150℃. Interestingly, the threshold voltage becomes large again (~ -40V) for this polymer affected by the stronger electron-donating property of propionyl group. The increased V_{th} for PTIPBDT might also be attributed to the partially removed propionyl groups during the polymerization process since the unstability of this functional group has been discussed in the previous parts, and the polymer molecules without the propionyl group will trap the hole carriers leading to large V_{th}.

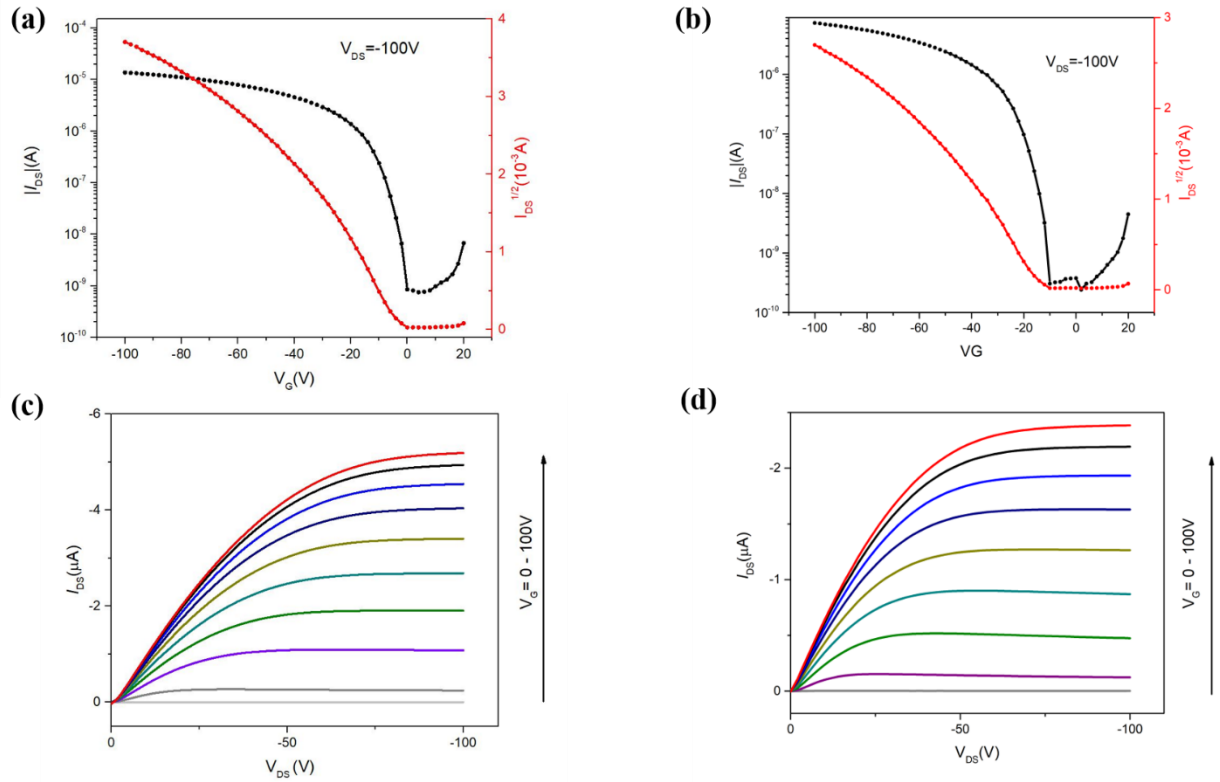

Figure 3-10 Transfer and output curves of PTIABDT annealed at 50℃ **(a, c)**, and PTIPBDT annealed at 150℃ **(b, d)**.

Table 3- 3 BGBC OFET performances of PTIABDT and PTIPBDT at different annealing temperatures

Polymer	Annealing Temp (℃)	Avg mobility ($cm^2V^{-1}s^{-1}$)	Max mobility ($cm^2V^{-1}s^{-1}$)	V_{th} (V)	$I_{ON/OFF}$
	RT	0.010 ±0.00066	0.011	-1.64	10^4
	50	**0.013 ±0.0014**	**0.015**	**1.96**	10^5
PTIABDT	100	0.0079±0.0012	0.0095	-2.78	10^5
	150	0.010 ±0.0018	0.013	-9.46	10^5
	200	0.0058±0.0014	0.0072	-27.95	10^4
	RT	0.00449±0.00034	0.00498	-43.8	10^4
	50	0.00526±0.00078	0.00641	-41.3	10^4
PTIPBDT	100	0.00549±0.00034	0.00592	-36.0	10^4
	150	**0.00640±0.00042**	**0.00698**	**-41.6**	10^4
	200	0.00354±0.00080	0.00446	-47.5	10^4

3.5 Photovoltaic properties of PTIABDT and PTIPBDT

According to the discussion on energy levels and transistor mobilities, the new polymers including PTIABDT and PTIPBDT exhibit the same or even lower-lying HOMO levels and improved charge trapping properties compared with PTIBDT and PTIFBDT which should further increase the corresponding V_{oc} and show better charge transport hence achieving better photovoltaic performance. The first step still involves the investigation of exciton separation efficiency in the blend films via photoluminescence quenching efficiency (PLQE) technology.

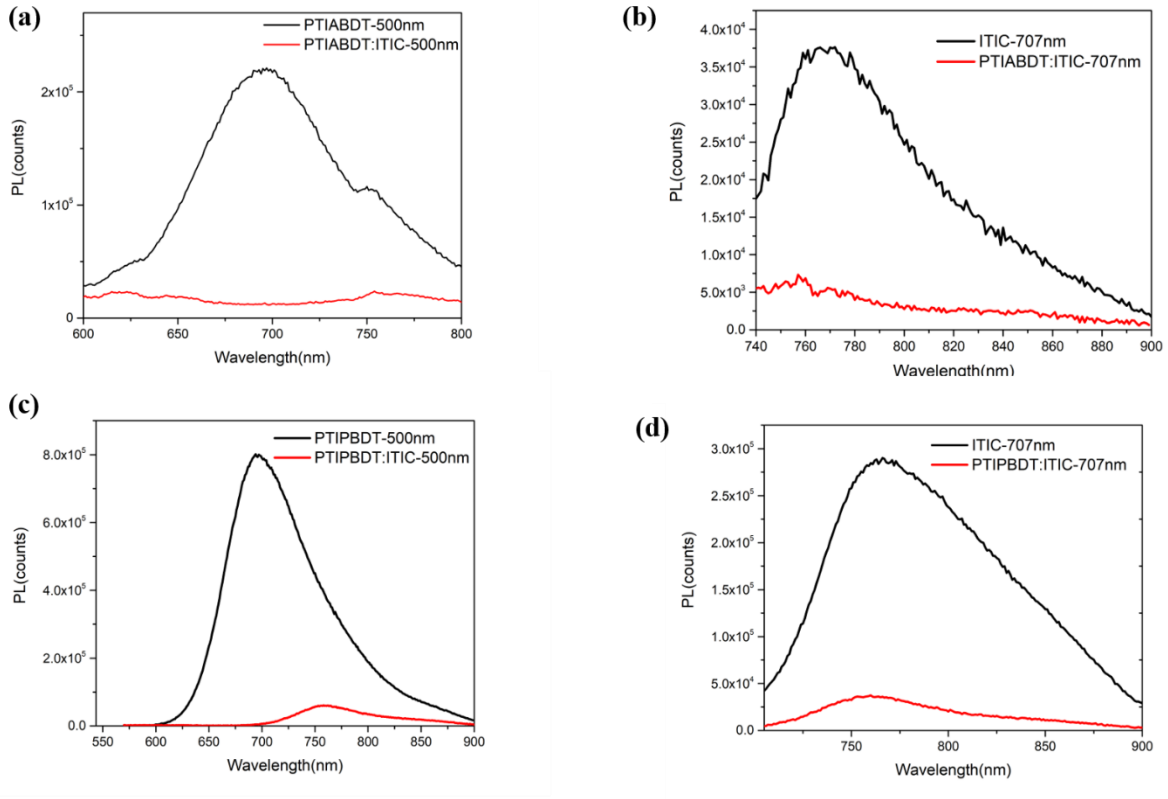

Figure 3-11(a) and (c) Photoluminescence spectra of neat films of PTIABDT, PTIPBDT and blend films of PTIBDT: ITIC, PTIFBDT: ITIC when excitation wavelength is 500nm. **(b) and (d)** neat film of ITIC and blend films of PTIBDT: ITIC, PTIFBDT: ITIC when excitation wavelength is 707nm.

The quenching results were shown in **Figure 3-11**, where the photoluminescence of PTIABDT and PTIPBDT pristine films which were excited at the wavelength of 500nm were quenched by ITIC with the PLQE values of 89% and 93% for their blend films, respectively. On the other hand, the photoluminescence of pristine ITIC film were quenched by PTIABDT and PTIPBDT with the PLQE results of 86% and 89%, respectively, when ITIC was excited at the wavelength of 707nm. The PLQE results revealed moderate efficiency of exciton diffusion and separation in PTIABDT:ITIC and PTIPBDT:ITIC blend films which could be further improved to enhance

better OPV properties if different acceptor materials are employed as what would be discussed later.

The inverted organic solar cell devices were fabricated with the blend films of PTIABDT:ITIC and PTIPBDT:ITIC as the active layers. The configuration of the OSC device and chemical structures of donor polymers and acceptors are illustrated in **Figure 3-12 (a)**.

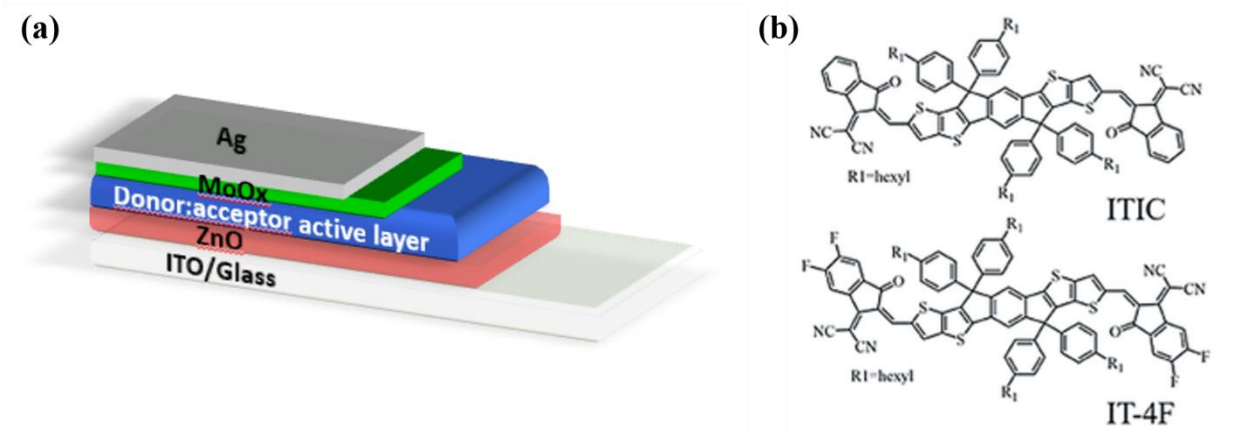

Figure 3-12 (a) Schematic of inverted device structure for OSCs and **(b)** chemical structures of ITIC and IT-4F.

The solar cell results for PTIABDT:ITIC and PTIPBDT:ITIC blend films were shown in **Figure 3-13** and **Table 3-3.** The PTIABDT:ITIC system exhibited a PCE of 3.99% with J_{sc} of 10.61mA/cm^2, V_{oc} of 1.05V, FF of 36%, and the PTIPBDT:ITIC system showed a lower PCE of 3.29% with J_{sc} of 7.84 mA/cm^2, V_{oc} of 1.05V and FF of 40% at room temperature. Both the systems demonstrated superior high V_{oc} values which were mainly due to their very lower-lying HOMO levels. However, the much lower current density (J_{sc}) and fill factor (FF) seriously limited the further improvement of these systems showing the low efficiency of exciton generation and dissociation and charge collection on the electrodes. Both PTIABDT:ITIC and PTIPBDT:ITIC active layers showed decreased PCE results when annealed at 100℃ as shown in **Table 3-3.**

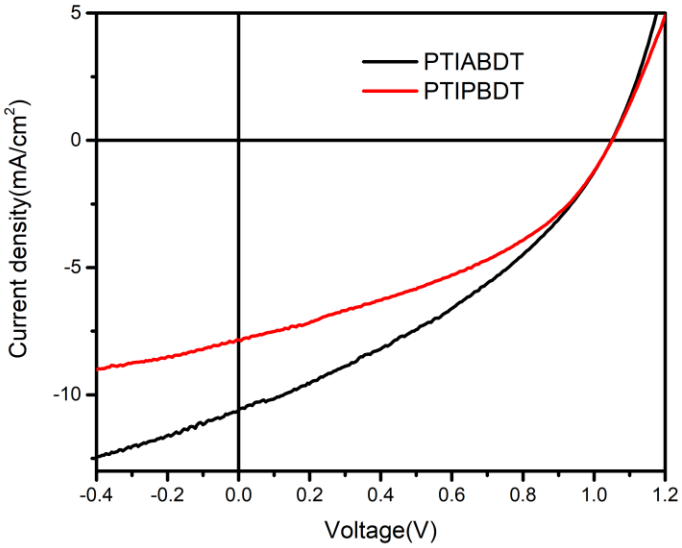

Figure 3-13 Current density-voltage (J-V) curves of OSCs of active layers of PTIABDT:ITIC and PTIPBDT:ITIC at room temperature.

Table 3-4 Summary of OSC devices performance of PTIABDT:ITIC and PTIPBDT:ITIC

Active layer	**D/A ratio**	**Solvent**	**Annealing temperature (℃)**	**Jsc (mA/cm^2)**	**Voc (V)**	**FF**	**PCE (%)**
PTIABDT:ITIC	1:1	CB	RT	10.61	1.05	0.36	3.99%
PTIABDT:ITIC	1:1	CB	100	9.81	1.03	0.33	3.32%
PTIPBDT:ITIC	1:1	CB	RT	7.84	1.05	0.40	3.29%
PTIPBDT:ITIC	1:1	CB	100	6.68	1.05	0.32	2.24%

The lower PCE results at annealing condition were consistent with the low crystallinity measured by two-dimensional grazing-incidence X-ray diffraction (2D-GIXD) of the neat polymer flaxes as shown in **Figure 3-14.** Very similarly with PTIBDT and PTIFBDT polymers in Chapter 2, PTIABDT and PTIPBDT showed a broad and weak lamellar diffraction (100) peak at 2θ= ~3.9 ° for PTIABDT and 2θ= ~4.0 ° for PTIPBDT without appearance of π-π stacking diffraction peak. The corresponding d-spacing in interlamellar direction was estimated to be 2.26nm for PTIABDT and 2.21nm for PTIPBDT which was slightly less ordered than PTIBDT and PTIFBDT with d-spacing of 2.1nm and 1.96nm. All four polymers including reported PTIBT exhibit low crystallinity which might be due to the intrinsic property of Type II D-A copolymers with large conjugated side chains easily leading to disordered polymer chain interaction which also partially explains the acquirement of low J_{sc} and FF since the very amorphous morphology does not favor the efficient exciton diffusion and free carrier transport.

(a)

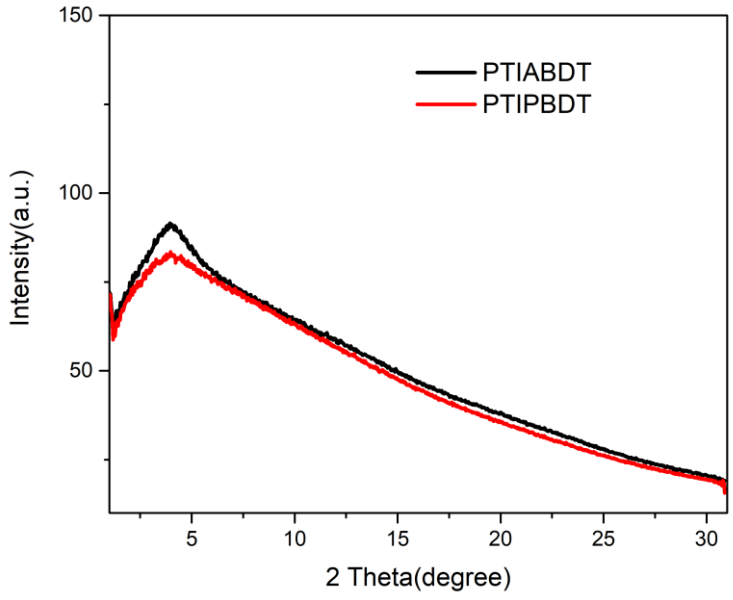

(b)

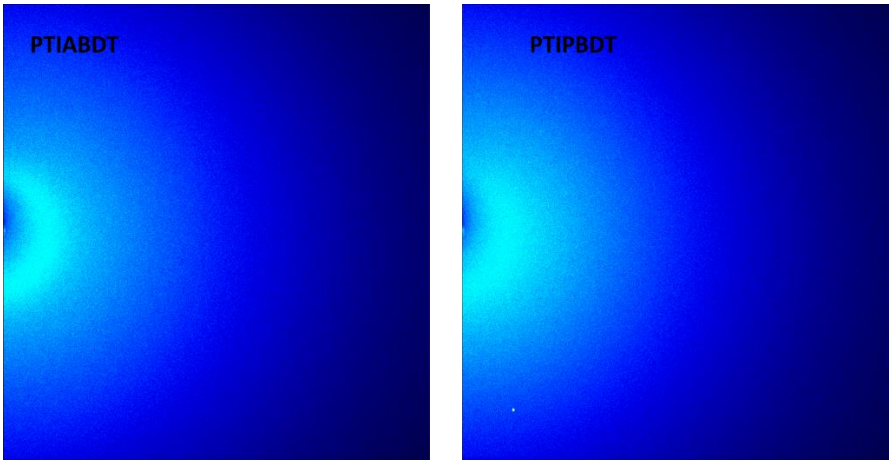

Figure 3-14 ***(a)*** *Out of plane line cuts of GIXD patterns, and* ***(b)*** *images of PTIABDT and PTIPBDT.*

One possible explanation for the low FF and J_{sc} of PTIABDT:ITIC system was because of the poor solubility of PTIABDT polymer which showed no solubility in chloroform and only dissolved in hot chlorobenzene and thus resulted in non-homogeneous donor-acceptor separation which was not favored for the exciton separation and free carriers transport leading to both low J_{sc} and FF. However, although PTIPBDT polymer demonstrated much better solubility in chloroform and should enhance the homogeneously mixed phase of donor polymer and acceptor materials, PTIPBDT:ITIC blend still exhibited even lower J_{sc} and also low FF. The lower J_{sc} of PTIPBDT based OSCs might be due to its lower lateral hole mobility and more serious hole trapping problem illustrating by high V_{th} compared with PTIABDT polymer as discussed in the OFET part.

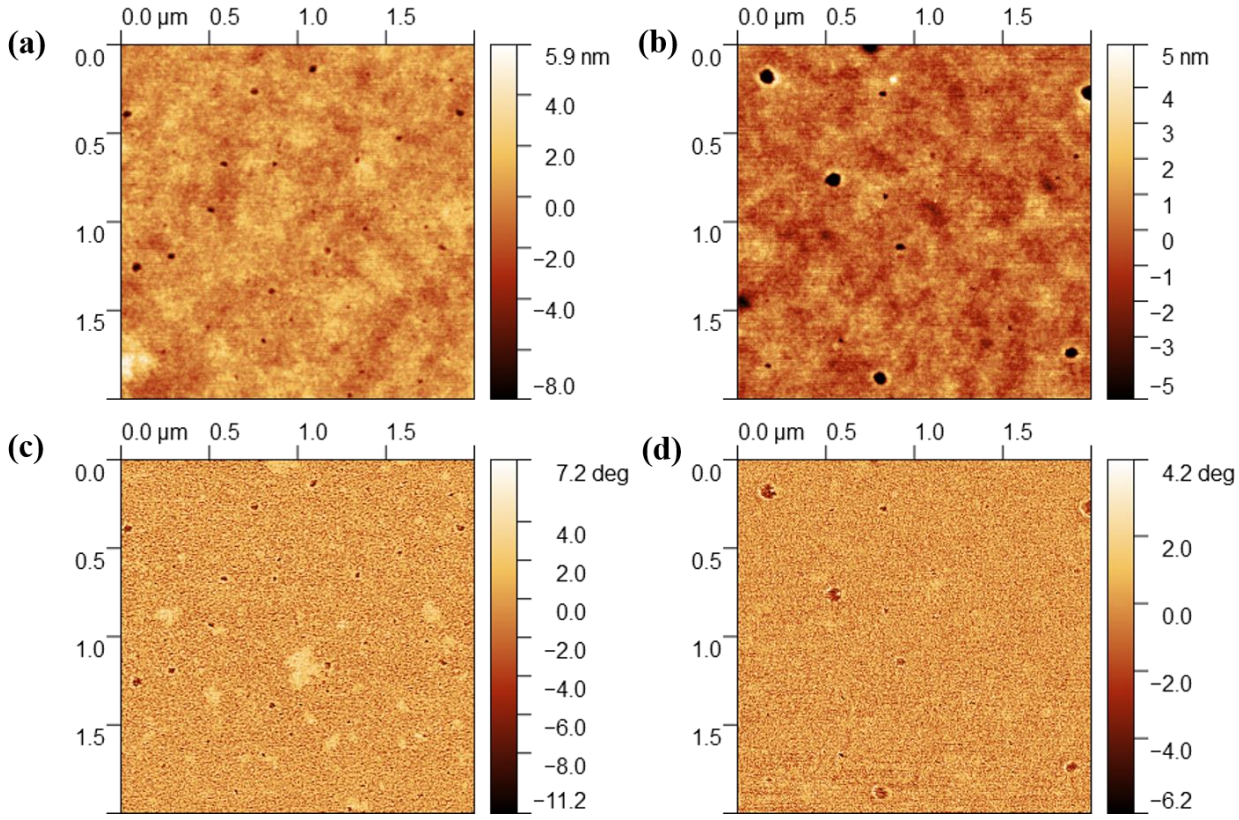

Figure 3-15 AFM height **(a)** and phase **(c)** images of PTIABDT:ITIC blend film, and height **(b)** and phase **(d)** of PTIPBDT:ITIC blend film.

To further investigate the photovoltaic results, the blend film morphology was characterized by AFM as illustrated in **Figure 3-15**. For the PTIABDT:ITIC blend, the height image showed relative smooth morphology with the RMS roughness of 0.93nm indicating homogenously separation between donor polymer and ITIC. However, it was observed that lots of small pinholes existed in the film which might trap the transport of charge carriers resulting in low J_{sc} and FF. The phase image of PTIABDT:ITIC also demonstrated the existence of pinholes and some grain aggregation which could be related with the poor processability of PTIABDT in the solvent. On the other hand, it was found that PTIPBDT:ITIC blend film showed decreased numbers of pinholes and even lower RMS roughness of 0.74nm as shown in height and phase images as a result of

improved solubility of PTIPBDT. Nevertheless, this blend seemed to exhibit poor miscibility between PTIPBDT and ITIC due to the large size of formed pinholes and less homogenous film morphology which was not favored for the exciton diffusion and charge carrier transport resulting in low photocurrent generation.

Another possible explanation for the extremely low FFs of PTIABDT and PTIPBDT based OSC could be due to the improper choice of acceptor material. Hence the fluorinated counterpart of ITIC, IT-4F (**Figure 3-12 (b)**), was chosen to be alternative acceptor which exhibits deeper energy levels with 0.16eV lower HOMO and 0.25eV lower LUMO and much red-shifted light absorption as well as enhanced light absorption coefficient compared with ITIC. [39] Since the better processability of PTIPBDT showed less improvement on J_{sc} and FF, PTIABDT was adopted as donor material to match with IT-4F. PLQE was utilized to investigate the efficiency of exciton diffusion and separation of PTIABDT:IT-4F blend film. As shown in **Figure 3-14 (a)**, **(b)**, the quenching efficiency of PTIABDT and IT-4F in PTIABDT:IT-4F blend film was determined to be 97% and 98% for the pristine PTIABDT film excited at 500nm wavelength and IT-4F film excited at 740nm, respectively. The better PLLQE results when IT-4F was applied compared with ITIC demonstrate improved exciton diffusion and separation which are expected to contribute to J_{sc} and FF.

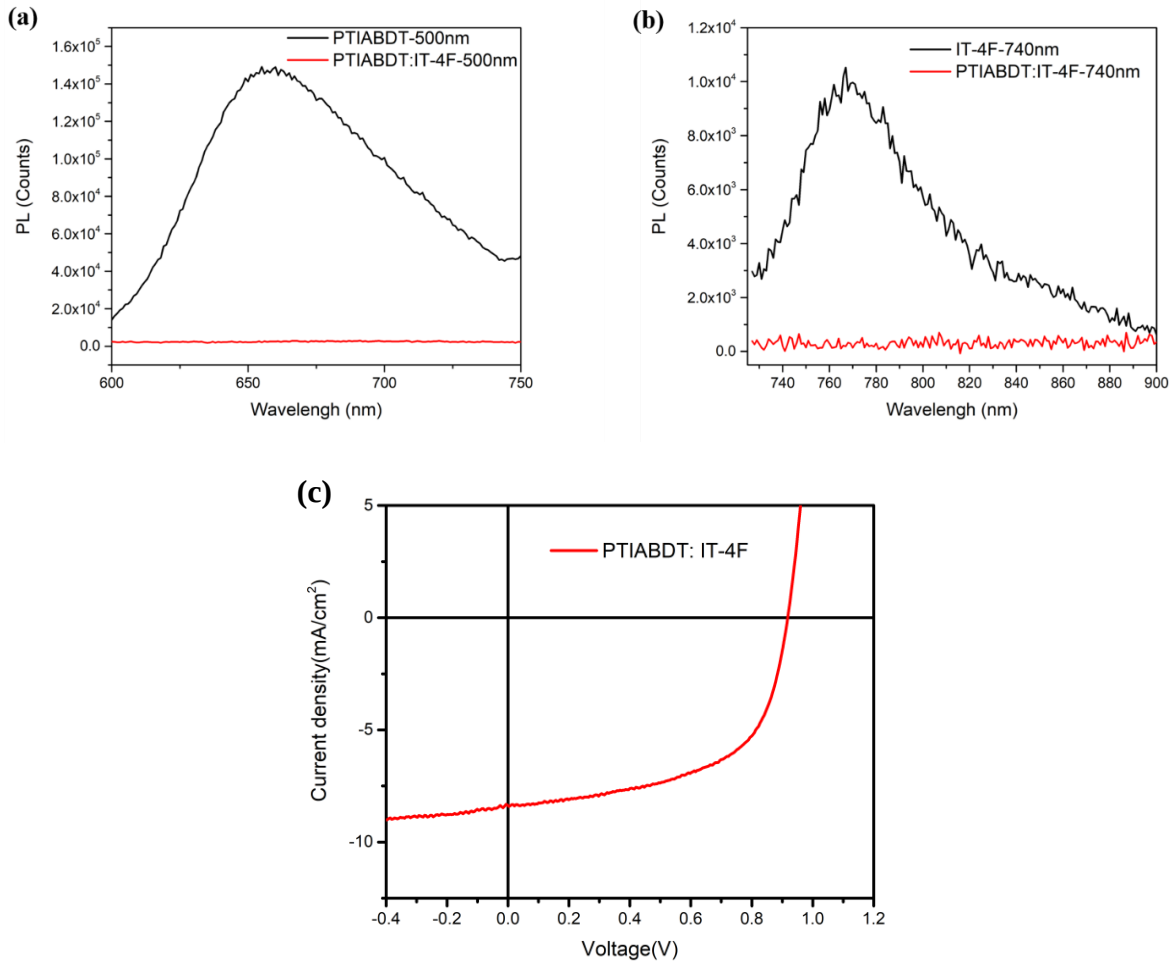

Figure 3-16 (a) Photoluminescence spectra of neat films of PTIABDT and blend films of PTIABDT: IT-4F when excitation wavelength is 500nm, **(b)** neat film of IT-4F and blend films of PTIABDT: IT-4F when excitation wavelength is 707nm, and **(c)** current density-voltage (J-V) curves of OSCs of active layers of PTIABDT:IT-4F.

The PTIABDT:IT-4F blend film was thus applied as active layer in the inverted OSC device. The OSC results are shown as **Figure 3-14 (c)** and **Table 3-4.** Although FF was improved from 0.36 to 0.58 hence resulting in better PCE of 4.48% compared with the PCE obtained with ITIC, the J_{sc} and V_{oc} simultaneously decreased which might be related with the less favored bi-continuous and interpenetrating network of active layer when IT-4F was used as acceptor demonstrating the

complexity of choice of acceptor materials to achieve all enhanced J_{sc}, V_{oc} and FF without sacrifice of relating parameters.

Table 3-5 Summary of OSC devices performance of PTIABDT:IT-4F

Active layer	D/A ratio	Solvent	Annealing temperature (℃)	Jsc (mA/cm^2)	Voc (V)	FF	PCE (%)
PTIABDT:ITIC	1:1	CB	RT	8.38	0.92	0.58	4.48%

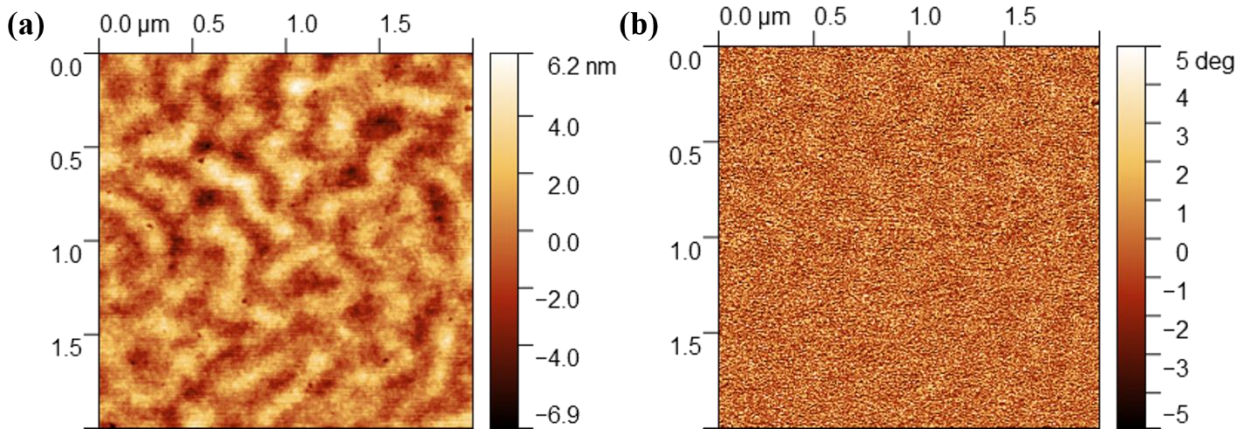

Figure 3-17 AFM height **(a)** and phase **(b)** images of PTIABDT:IT-4F blend film.

As shown in **Figure 3-17**, the PTIABDT:IT-4F blend film was characterized by AFM. Interestingly, it was found that the phase separation of this blend film was improved without existence of pinholes if compared with the PTIABDT:ITIC blend film. In addition, the RMS roughness of this blend was increased to 1.6nm, and this kind rougher surface should enhance the diffusion of excitons and the transport of charge carriers, and hence the improved phase separation and increased roughness could partially explain the much enhanced FF in this system. However, the film showed several obvious edges demonstrating the poor miscibility between PTIABDT and

IT-4F without the formation of bi-continuous interpenetrating network which could be attributed to the poor solubility of PTIABDT polymer.

3.6 Summary and Future directions

In conclusion, in this chapter, two Type-II D-A copolymers of PTIABDT and PTIPBDT were designed and synthesized with the introduction of strong electron-withdrawing carbonyl functional group as further development of this type of polymers to improve the hole trapping problem. PTIABDT with acetyl group was found to show high molecular weight whereas the solubility was poor in common organic solvents such as chloroform and only dissolved in hot chlorobenzene. PTIPBDT with the longer propionyl group was thus synthesized to improve solubility. Interestingly, the monomer for PTIPBDT formed mixture of Z/E isomers after the Knoevenagel condensation different from monomers for PTIBDT, PTIFBDT and PTIABDT with only Z-configuration after the condensation reaction which might be due to effect of longer propionyl chain on the tendency of the vinylene linkage between BDT and indolin-2-one to rotate hence forming Z/E isomers.

Both PTIABDT and PTIPBDT were investigated to show decreased band gaps around 1.83eV with lightly red shifted light absorption and comparable deep-lying energy levels with PTIBDT and PTIFBDT. Noticeably, PTIPBDT exhibits the lowest HOMO level of -5.63eV in this series of polymers. As what we expected to see, PTIABDT demonstrated much improved OFET hole mobility which is up to $0.015 cm^2V^{-1}s^{-1}$ with low threshold voltage which is almost zero revealing less hole trapping problem which could be attributed to the acetyl group withdrawing the free pair of electrons from nitrogen atom on indolin-2-one unit. However, both PTIABDT and PTIPBDT polymers showed lower PCE results when matched with ITIC compared with PTIBDT and PTIFBDT, and PTIABDT showed the highest PCE of 4.48% when IT-4F was applied as acceptor.

The much lower J_{sc} and FF could be due to the highly amorphous properties of polymers and the not favorable active layer morphology when ITIC or IT-4F was used resulting in low efficiency of exciton generation, diffusion and separation as well as charge carrier transport and collection.

For the future direction, the polymer PTIABDT exhibits high hole mobility and low V_{th} making it suitable sensing platform for OFET based sensor to detect various chemicals and temperature change. For instance, our group has established methodology to detect real time temperature change using the indolin-2-one based conjugated polymers as active layers in resistor-type sensor showing high sensitivity. Thus it will be interesting to investigate the temperature sensitivity of PTIABDT which also involves the indolin-2-one structure since the temperature response has been assumed to be related with the properties of this constructing unit.

3.7 Experimental section

Materials and characterization

All solvents and chemicals were provided by commercial suppliers such as Sigma-Aldrich and were directly applied without any purification. The DFT simulation, NMR, HT-GPC, TGA, DSC measurements, UV-vis, CV, XRD and PL characterization were completed following the same process as described in Chapter 2.

Fabrication and Characterization of OFET and OSC devices

The fabrication and characterization of OFET and OSC devices were consistent with the procedures and details described in Chapter 2.

Synthesis Procedures

Synthesis of (Z)-1-acetyl-3-((2,5-dibromothiophen-3-yl)methylene)indolin-2-one (M1)

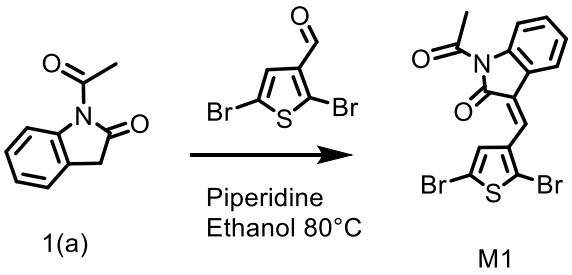

1(a) M1

2,5-Dibromothiophene-3-carbaldehyde(0.316g, 1.171mmol) and n-acetyl-2-oxindole (0.205g, 1.171mmol) were added to a 25mL dry two-neck round bottom flask, and the reactor was purged for three times with nitrogen. Anhydrous ethanol (9mL) was injected via a syringe, and piperidine(0.156mL) was then added. The white mixture solution changed to yellow color immediately after addition of piperidine. The reaction mixture was then stirred overnight at room temperature under nitrogen protection. Yellow solid precipitate out from the solvent after overnight refluxing. The crude solid was filtered and washed with ethanol and methanol to get the product. (yield: 0.2g, 40%) 1H NMR (300 MHz, CDCl3, δ/ppm): 8.42 (s, 1H), 8.28-8.25 (d, J = 9Hz, 1H), 7.63-7.60 (d, J = 9Hz, 1H),7.47 (s, 1H), 7.39-7.32 (t, J = 6Hz, 1H), 7.23-7.21 (d, J = 9Hz, 1H), 2.75 (s, 3H).

Synthesis of (Z)-3-((2,5-dibromothiophen-3-yl)methylene)indolin-2-one (2)

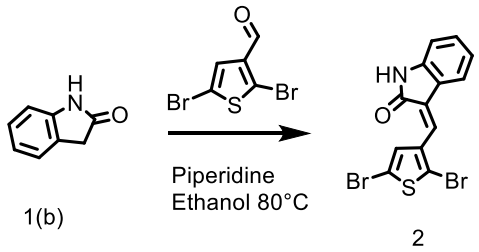

1(b) 2

2,5-Dibromothiophene-3-carbaldehyde(0.351g, 1.30mmol) and indolin-2-one (0.246g, 1.30mmol) were added to a 25mL dry two-neck round bottom flask, and the reactor was purged for three times with nitrogen. Anhydrous ethanol (11 mL) was injected via a syringe, and piperidine (0.173mL) was then added. The mixture changed color to yellow immediately when piperidine was added. The reaction mixture was then refluxed overnight under nitrogen protection. Orange solid precipitate out from the solvent after overnight refluxing. The solid was filtered and washed with methanol to get the product. (yield: 0.4g, 80%) 1H NMR (300 MHz, CDCl3, δ/ppm): 8.66 (s, 1H), 7.56-7.54 (d, J = 6Hz, 2H), 7.41 (s, 1H), 7.27-7.22 (m, 1H), 7.08-7.03 (t, J = 6Hz, 1H), 6.85-6.82 (d, J = 9Hz, 1H).

Synthesis of 3-((2,5-dibromothiophen-3-yl)methylene)-1-propionylindolin-2-one (M2)

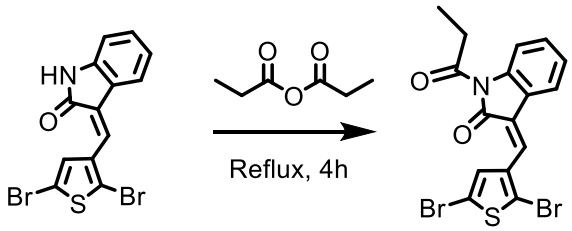

2 M2

In a 25 mL one-necked flask, M2 (0.125g, 0.0325mmol) was suspended in propionic anhydride (3mL) and refluxed at 150 ℃ for 4 h, and the mixture became red solution at 150℃. After that time, the mixture was cooled down and poured to 200mL DI water and extracted with diethyl ether. The organic layer was collected and dried with anhydrous sodium sulfate (Na2SO4), and then the solvent was evaporated by rotary evaporator to obtain the yellow-green solid. The crude solid was further purified by column chromatography using the eluent of 1:7 dichloromethane and hexane. Two isomers were successfully separated with Z and E configurations, respectively. (yield: 123mg, 43% (Z-isomer) 78mg, 27% (E-isomer)) ^{1}H NMR (300 MHz, CDCl3, δ/ppm): 8.41 (s, 1H), 8.29-

8.26 (d, J = 9Hz, 1H), 7.62-7.60 (d, J = 6Hz, 1H), 7.46 (s, 1H), 7.39-7.34 (t, J = 6Hz, 1H), 7.28-7.20 (m, 1H), 3.21-3.13 (q, J=9Hz, 3H). (Z-isomer) ^{1}H NMR (300 MHz, CDCl3, δ/ppm): 8.36-8.33 (d, J = 9Hz, 1H), 7.59-7.56 (d, J = 9Hz, 1H), 7.49 (s, 1H), 7.41-7.36 (t, J = 9Hz, 1H), 7.30 (s, 1H), 7.18-7.13 (d, J = 9Hz, 1H), 3.22-3.14 (q, J=9Hz, 3H). (E-isomer)

Synthesis of polymer PTIABDT

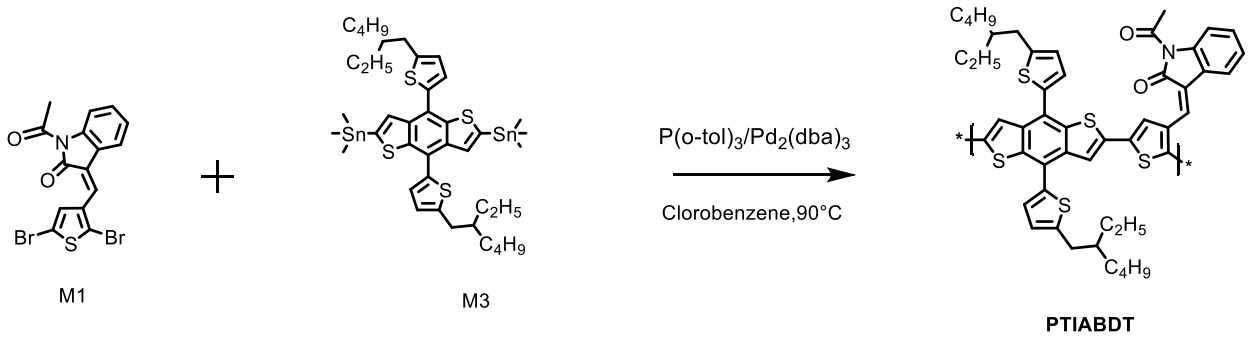

M1 (0.0759g, 0.1777mmol, 1.0 eq.), M3 (0.161 g, 0.1777 mmol, 1.0 eq.) and tri(*o*-tolyl)phosphine (P(o-tol)3) (0.00433g, 0.1777mmol, 0.08 eq.) were added to a 25 mL dry two-neck round bottom flask connecting with a water condenser, and the reactor was purged for three times. Anhydrous chlorobenzene (3 mL) was firstly injected to the reactor via a syringe to dissolve the solid, and subsequently tris(dibenzylideneacetone)dipalladium (Pd2(dba)3) (0.00325g, 0.003554 mmol, 0.02 eq.) was added as solution in 0.5mL anhydrous chlorobenzene. The temperature was then heated to 90℃, and the reaction mixture was then stirred for 18 hrs under argon protection. The reaction solution was then cooled down to room temperature and poured into 150mL stirring methanol. The crude solid was filtered and washed by methanol, dried and lastly purified via Soxhlet extraction with the solvents of acetone, hexane, chloroform and chlorobenzene. A dark green film was obtained after removal of the chlorobenzene solvent.

Synthesis of polymer PTIPBDT

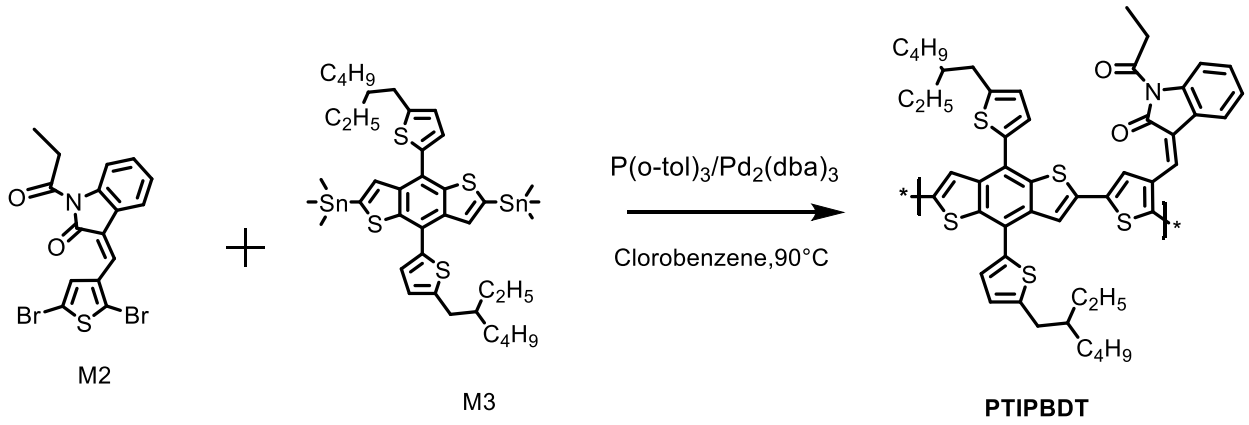

M2 (0.0493g, 0.112mmol, 1.0 eq**.),** M3 (0.101g, 0.112mmol, 1.0 eq.) and tri(*o*-tolyl)phosphine (P(o-tol)3) (0.00272g, 0.00894mmol, 0.08 eq.) were added to a 25 mL dry two-neck round bottom flask connecting with a water condenser, and the reactor was purged for three times. Anhydrous chlorobenzene (3.5 mL) was firstly injected to the reactor via a syringe to dissolve the solid, and subsequently tris(dibenzylideneacetone)dipalladium (Pd2(dba)3) (0.00205g, 0.00224 mmol, 0.02 eq.) was added as solution in 0.5mL anhydrous chlorobenzene. The temperature was then heated to 90℃, and the reaction mixture was then stirred for 18 hrs under argon protection. The reaction solution was then cooled down to room temperature and poured into 150mL stirring methanol. The crude solid was filtered and washed by methanol, dried and lastly purified via Soxhlet extraction with the solvents of acetone, hexane, chloroform and chlorobenzene. A dark green film was obtained after removal of chloroform solvent.

Chapter 4 Design and Synthesis of Water-soluble Polymer Based on Isoindigo

4.1 Introduction

The development of new energy-relevant technologies including organic solar technology must achieve a balance between high efficiency and the mass manufacturing with non-toxic materials especially avoiding the usage of excessive toxic halogenated solvents. [100] It is thus significantly essential to develop green-solvent-processable conjugated polymers so that organic electronics can be fabricated in large scale without involvement of environment polluting substances. [50] As fully green polymers which can dissolve in water or alcohol, π-conjugated polyelectrolytes (CPEs) are generally composed of a conjugated backbone which shows great influence on determination of the intrinsic properties of CPEs and a functional side chain to render them soluble in water or ethanol. [48,51] CPEs can be further clarified as cationic ones with positive terminal ions and negative counterions such as the CPEs modified with quaternary ammonium salts [101,102] as shown in **Figure 4-1**.

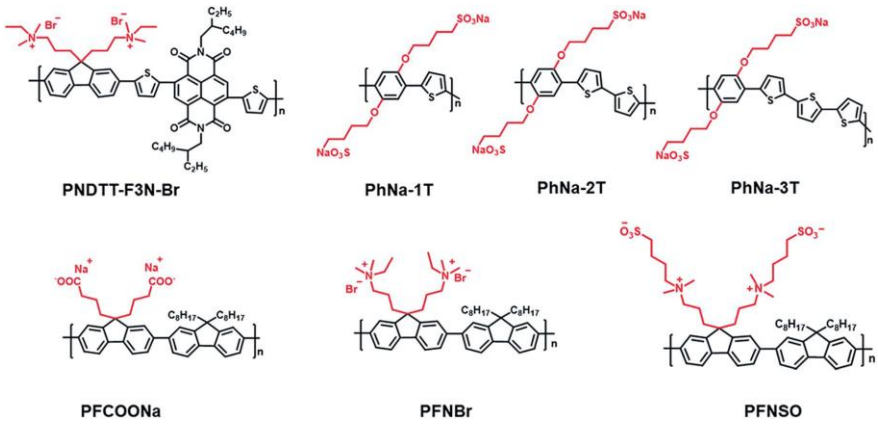

Figure 4-1 Chemical structures of different CPEs. [48]

Anionic CPEs are functionalized with negative terminal ions and positive counterions instead such as sulfonates [103] and carboxylic acids. [104] Zwitterionic CPEs describe the CPEs with both anionic

and cationic groups including sulfobetaine zwitterionic groups [105] as shown in **Figure 4-1**. Recently, it has been reported that CPEs show high potential to be applied in organic light-emitting devices [106,107] and OPV cells typically as the charge injection/extraction or transport interlayers [51,108]. Thin-film transistors based on CPEs also demonstrate a moderate mobility which is up to 10^{-4} $cm^2V^{-1}s^{-1}$. [109] These achievements hence have greatly encouraged the development of new designs of CPEs especially in donor-acceptor structure.[110]

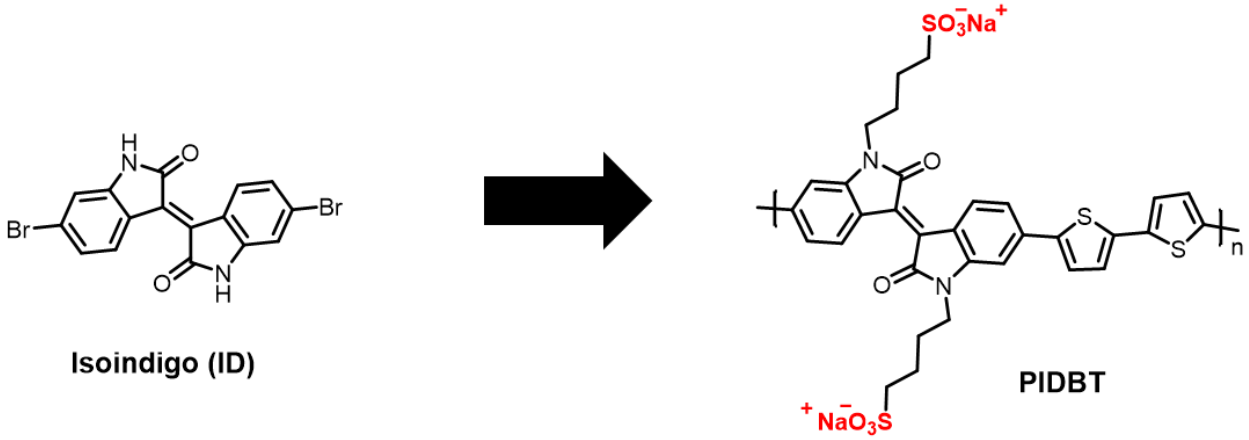

Figure 4-2 Chemical structures of isoindigo (ID) and CPE PIDBT.

Isoindigo (ID) is one of the frequently investigated indigoid dyes with two indolin-2-one units connected by the central double bond in E-configuration as shown in **Figure 4-2**. [111] N-alkylation can be used to enhance the solubility of ID and its derivates by breaking the strong hydrogen bonding which typically forms between C=O and N-H group, and the soluble ID derivates have been reported to copolymerize with donor units as strong electron-withdrawing acceptor structure to yield D-A copolymers which typically exhibit low energy levels and broad light absorption band in the range of visible light region and hence show promising results in applications involving OSCs and OFETs. [112–114] However, rare research has been reported focusing on the ID-based conjugated polyelectrolytes, and no research result can be found relatied with OFET and OSC

performance of ID-based CPEs. Consequently, in this chapter, a water-soluble ID-based CPE was successfully designed and synthesized as further development of indolin-2-one based copolymers reported in Chapter 2 and Chapter 3 which can meet the "Green" objective of materials design.

4.2 Synthesis of Monomer and Polymer

Both cationic and anionic ID-based CPEs are designed with the introduction of the 2-ethyl trimethylammonium and butyl sulfonate groups, respectively as shown in **Figure 4-3**. For the monomer synthesis, the cationic and anionic groups should be introduced by the N-alkylation of 6,6-dibromoisoindigo. During this procedure, the dibromoisoindigo will be deprotonated under the alkaline environment which is provided by the excessive potassium carbonate base using anhydrous DMF as the solvent. Then the 2-ethyl trimethylammonium and butyl sulfonate group formed by the ring-opening of 1,4-butane sultone could be alkylated to the nitrogen atom of dibromoisoindigo to obtain the water or alcohol soluble monomers. For the N-alkylation reaction of monomer 1 with 2-ethyl trimethylammonium group, the reaction mixture changed color from the dark red of the dibromoisoindigo solution to dark blue color, and some dark purple crystal compounds could be obtained in a yield over 90% after the removal of DMF solvent. The crude compound demonstrated no solubility in water and could dissolve in both ethanol and methanol. However, almost no ^{1}H-NMR signals could be observed when this compound was dissolved in chloroform-d, dimethyl sulfoxide-d_6, and methanol-d_4 which may be due to its strong tendency to aggregate in these solvents. Consequently, anionic butyl sulfonate was introduced instead to achieve water-soluble ID monomer as shown in **Figure 4-3**.

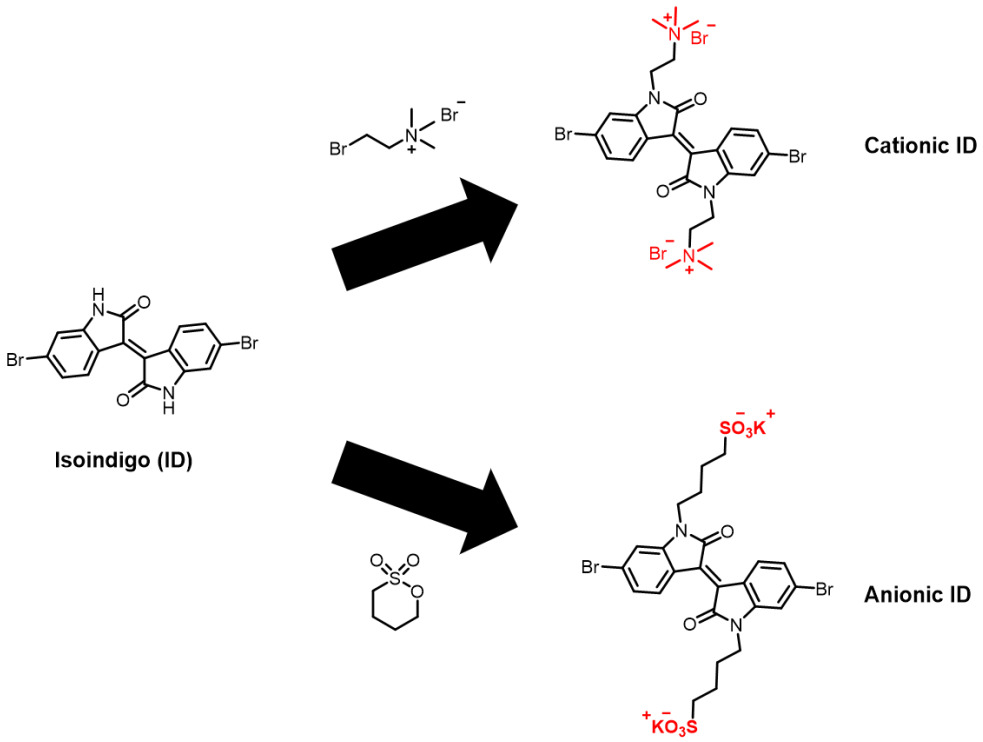

Figure 4-3 Chemical structures of cationic and anionic ID.

Kou et. al firstly reported the synthesis of sulfonated ID electrolyte to copolymerize with phenylenevinylene unit via Heck coupling method to obtain the water-soluble PIDPV as the resulting anionic CPE which was then investigated to exhibit efficient quenching effect. [111] However, the synthesis of donor-acceptor CPEs has been reported to particularly depend on Suzuki polymerization where it is possible to directly polymerize the water-soluble ionic monomer in aqueous conditions in efficient proceeding. For instance, Jo et. al reported the synthesis of a series of CPEs copolymerized with dibromo-1,4-bis(4-sulfonatobutoxy)benzene and different donor counterparts involving different numbers of thiophene rings via Pd-catalyzed Suzuki coupling reaction in a mixed solvent of dimethylformamide (DMF) and water. [103] On the other hand, there has been few research focused on the synthesis of CPEs utilizing Stille coupling which is regarded

as ubiquitously adopted method to synthesize conjugated polymers. It is thus of great significance to investigate the possibility to synthesize CPEs via Stille coupling reaction.

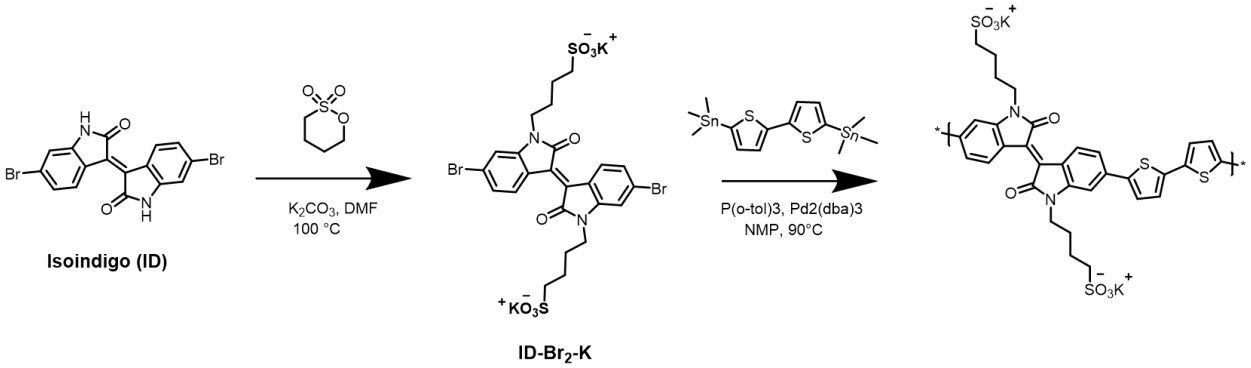

Figure 4-4 Synthetic route 1: direct Stille-coupling polymerization with ID-Br_2-K.

The first step involved the synthesis of anionic ID monomer with the counterion of potassium as shown in **Figure 4-4**. The ID-Br_2 was deprotonated under alkaline environment provided by excessive potassium carbonate, and the butyl sulfonate side chain formed was N-alkylated to obtain the product electrolyte, ID-Br_2-K. This crude compound precipitated out from DMF solvent when it was cooled down to room temperature, and the crude product was filtered and washed with acetone and dichloromethane and then recrystalized from the cosolvent of acetone and water to yield the pure product as dark brown solid in 78% yield. Due to the intrinsic properties of this ionic compound, ID-Br_2-K exhibited excellent solubility in water and was found to be undissolved in common organic solvents including chlorobenzene and DMF. To render this compound dissolve in organic solvents so that Stille coupling reaction can normally proceed, the very polar organic solvent N-methyl-2-pyrrolidione (NMP) which was investigated to dissolve ID-Br_2-K at 90℃ in good solubility was utilized as solvent for the direct Stille coupling polymerization with ID-Br_2-K electrolyte and bithiophene stannane monomer in the presence of $Pd_2(dba_3)$ as catalyst and P(o-$tol)_3$ as ligand. However, this reaction did not show much change in solution color or viscosity

when heated at 90℃ for 48hrs, and it could be due to the very polar solvent compound NMP could attract the palladium (Pd) catalyst and thus trap it in its molecules leading to the low efficiency of Pd catalysis in the process of Stille coupling reaction. Consequently, some DMF with much lower polarity compared with NMP was introduced as another phase of solvent combining with the raised temperature of 110℃ working together to improve the Pd trapping problem. After another 24hrs, the reaction was cooled down to room temperature, and some solid product was precipitated out in acetone. However, the solid obtained was confirmed to be the monomer ID-Br_2-K compound via ^{1}H-NMR measurement demonstrating the high challenge to synthesis CPE directly from ionic monomer.

Consequently, another approach was adopted to modify the ID electrolyte with tetra-phenylphosphonium counterion as shown in **Figure 4-5**. This unique modification of ID electrolyte can effectively protect the anionic sulfonate group and make it soluble in organic solvents such as DMF via the introduction of bulky organic ion of PPh_4^+ as reported by Leem et. al in 2018. [110] PPh_4^+ was chosen as the suitable precursor ion group to functionalize sulfonate ID since it was previously reported to successfully solubilize a sulfonate quinacridone molecule in organic solvents and was easily converted back to sodium sulfonate salt in a quantitative yield when NaI was added. [115] Hence the ID-Br_2-K compound was directly converted to tetra-phenylphosphonium substituted ID-Br_2-PPh_4 one via simply stirred in tetraphenylphosphonium bromide aqueous solution for 1 hr following extraction by DCM solvent. The solvent was then evaporated, and the crude solid was further purified through recrystallization in acetone to get the pure product as red solid. The resulting ID-Br_2-PPh_4 demonstrated much improved solubility in commonly used organic solvents including DCM, chloroform and DMF. Stille coupling polymerization was then proceeded using ID-Br_2-PPh_4 and bithiophene stannane monomer with

the $Pd(PPh_3)_4$ as palladium catalyst with ligand in DMF solvent. The mixture was stirred for 72hrs at 90℃, and the color changed from dark red to dark blue after overnight stirring. After cooled down to room temperature, the reaction mixture was precipitated in ethyl acetate to get the PIDBT with PPh_4^+group in 87% yield. The final CPE of PIDBT with sodium counterion was obtained by adding the solution of PIDBT-PPh_4 to acetone solution of sodium iodide, and the precipitate could be filtered to get the water-soluble PIDBT.

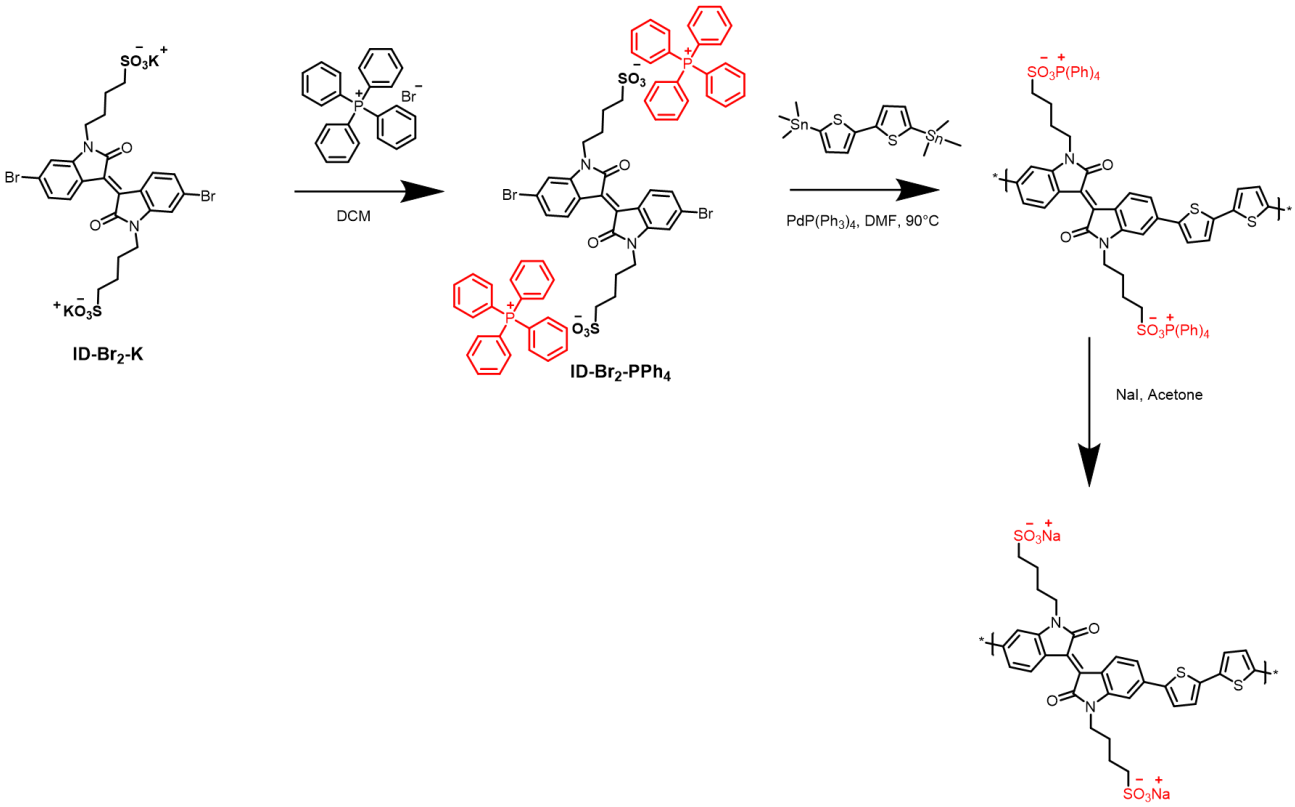

Figure 4-5 Synthetic route 2: Stille-coupling polymerization with precursor ID-Br_2-PPh_4.

4.3 Summary and Future Directions

In conclusions, water-soluble conjugated polyelectrolytes (CPEs) based on isoindigo (ID) structure have been designed and synthesized. Both cationic 2-ethyl trimethylammonium and anionic butyl sulfonate groups have been attempted to be alkylated to the ID unit to make it water or alcohol-soluble. Nevertheless, the alkylation of 2-ethyl trimethylammonium to ID was not successful related with the strong aggregation tendency of the resulted compound. The alkylation of butyl sulfonate generated the water-soluble anionic monomer ID-Br_2-K which was thus directly copolymerized with bithiophene stannane monomer via Stille-coupling using very polar solvent NMP. However, the polymerization could not proceed well which might be related with the trapping of Pd catalyst by NMP solvent. Consequently, unique precursor modification was combined with Stille-coupling polymerization to firstly convert ID-Br_2-K to ID-Br_2-PPh_4 making it soluble in organic solvents with the protection of bulky organic tetra-phenylphosphonium group. The PIDBT with PPh_4^+group was thus copolymerized with bithiophene stannane by Stille-coupling with $Pd(PPh_3)_4$ as catalyst in DMF solvent which was then converted to water-soluble PIDBT with Na^+.

For the future work, the optical, electrical and mobility of PIDBT will be further investigated and can be compared with common PIDBT conjugated polymers with normal organic alkyl chain as their “green” counterpart. Moreover, it’s also promising to apply the resulting polymer as the charge transport layer in conventional OPVs to get enhanced photovoltaic performances.

4.4 Experimental Section

Materials and characterization

All chemicals and solvents were purchased from commercial suppliers and were directly used without further purification.

Synthesis Procedures

Synthesis of potassium (E)-4,4'-(6,6'-dibromo-2,2'-dioxo-[3,3'-biindolinylidene]-1,1'-diyl)bis(butane-1-sulfonate) (ID-Br_2-K)

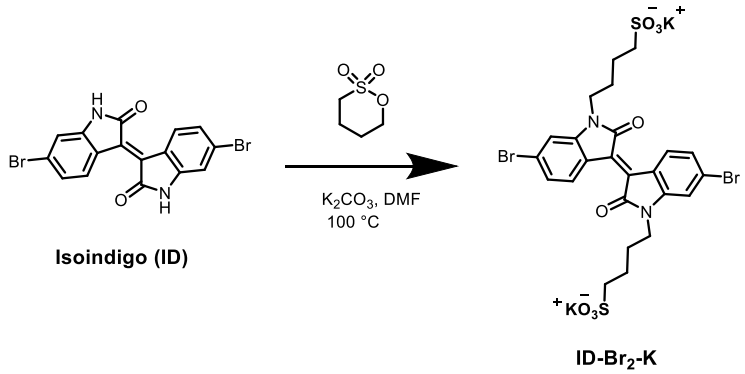

Isoindigo (ID)

ID-Br_2-K

Isoindigo (0.235g, 0.559mmol) and potassium carbonate (0.387g, 2.797mmol) were added to a 25mL two-neck flask, and the reactor was then purged for three times with nitrogen, anhydrous DMF (6mL) was injected via a syringe. The temperature was then heated up to 100℃, the mixture solution was stirred for 5 mins under nitrogen. Then 1,4-butanesultone (0.228g, 1.678mmol) was added, and the mixture was kept stirred at 100℃ overnight. The dark red mixture changed to dark blue color when the temperature was increased. After the solution was cooled down, the solid was filtrated, and the crude solid was then purified by recrystallization in mixed solvent of water/acetone. (yield: 0.36g, 80%) ^{1}H NMR (300 MHz, CDCl3, δ/ppm): 8.45-8.43 (d, J=6Hz, 2H), 7.17-7.14 (d, J = 9Hz, 2H), 7.06 (s, 2H), 3.65-3.37 (m, 4H), 2.98-2.93 (t, J = 6Hz, 4H), 1.70-1.70 (m, 8H).

Synthesis of tetra-phenylphosphonium (E)-4,4'-(6,6'-dibromo-2,2'-dioxo-[3,3'-biindolinylidene]-1,1'-diyl)bis(butane-1-sulfonate) (ID-Br_2-PPh_4)

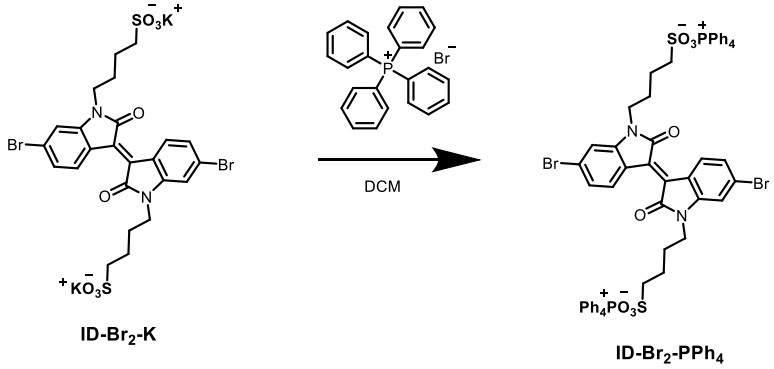

ID-Br_2-K

ID-Br_2-PPh_4

The solid ID-Br2-K was then dissolved in 150 mL DI H2O, and tetraphenylphosphonium bromide (1.747 g, 4.167 mmol) was subsequently added. The mixture was kept stirred at room temperature for 1 hr. The tetraphenyphosphonium sulfonate substituted isoindigo was then extracted using DCM (3 x 80 mL), and the organic layer was washed with 300 mL DI H2O. The organic layer was collected and dried with anhydrous sodium sulfate (Na2SO4), filtered, and the solvent was removed by rotary evaporator under reduced pressure to give 2.2 g of the crude product. 0.532g crude product was then recrystallized from acetone to yield pure compound as dark red solid (yield: 0.43g, 73%) ^{1}H NMR (300 MHz, CDCl3, δ/ppm): 9.02-9.89 (d, J = 9Hz, 2H), 7.92-7.87 (m, 8H), 7.80-7.74 (m, 16H), 7.65-7.58 (m, 16H), 7.05-7.03 (d, J=6Hz, 2H), 6.96 (s, 2H), 3.72-3.67 (t, J=6Hz, 4H), 2.87-2.82 (t, J=9Hz, 4H), 1.97-1.89 (m, 4H), 1.82-1.79 (m, 4H).

Synthesis of PIDBT

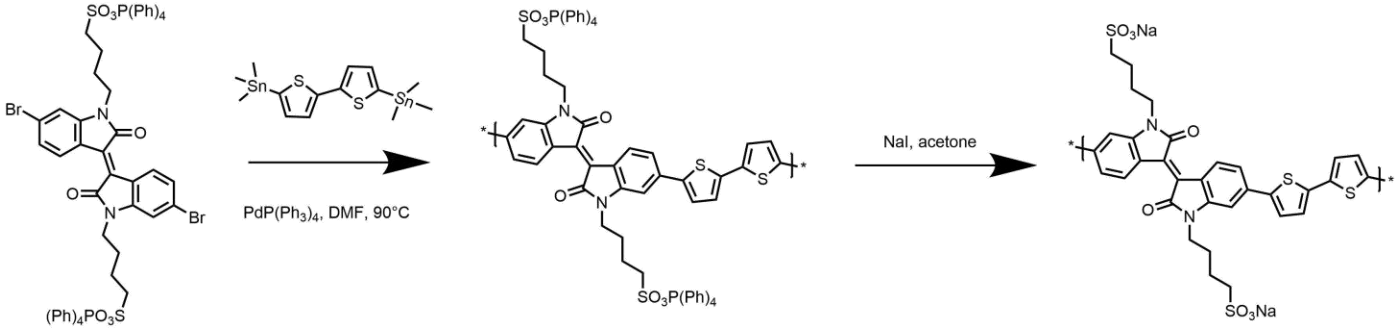

Compound ID-Br2-PPh4 (0.150g, 0.112mmol, 1.0 eq), 5,5'-bis(trimethylstannyl)-2,2'-bithiophene (0.040g, 0.112mmol, 1.0 eq.) were added to a 25 mL dry two-neck round bottom, and the reactor was purged for three times with argon. Anhydrous DMF (3.5 mL) was firstly injected to the reactor via a syringe to dissolve the solid, and subsequently tetrakis(triphenylphosphine)-palladium(0)(Pd(PPh3)4) (0.00205g, 0.00224 mmol, 0.1 eq.) was added as solution in 0.5mL anhydrous DMF. The temperature was then heated to 90℃, and the reaction mixture was then stirred for 72 hrs under argon atmosphere protection. The reaction solution was then cooled down to room temperature and poured into 150mL stirring ethyl acetate. The crude solid was filtered and washed with ethyl acetate (3×2mL) to get the PIDBT with P(PPh)4 ion. PIDBT was converted to sodium counterpart by addition of NaI in acetone.

Chapter 5 Summary and Future Directions

In conclusion, this thesis presents the successful design and synthesis of a series BDT and indolin-2-one based conjugated polymers which demonstrate wide optical band gaps and low-lying HOMO levels which enable their application as active layers using solution processable spin-coating method in organic electronics including OPVs and OFETs. Moreover, attempts have been made toward the design and synthesis of green-solvent processable conjugated polymers to achieve the fabrication of organic electronics without usage of highly toxic and environmentally harmful halogenated solvents.

In chapter 2, PTIBDT and its fluorinated polymer PTIFBDT have been polymerized via the Stille-coupling method as further development of our previously reported Type II donor-acceptor polymers with donor backbone and acceptor side chain. The previously reported polymer, PTIBT was investigated to achieve a high PCE of 5.72% and OFET hole mobility up to 0.018$cm^2V^{-1}s^{-1}$. However, the low V_{oc} of 0.66V seriously restricted the further improvement of PCE results based on PTIBT mainly due to its high-lying HOMO level of -5.41eV. PTIBDT and PTIFBDT were thus developed with stronger donor BDT backbone moiety and indolin-2-one acceptor side chain with short methyl group to reduce the steric hindrance caused by long alkyl chain in PTIBT. Consequently, PTIBDT and PTIFBDT exhibit wider optical band gaps to be 1.91eV for PTIBDT and lower-lying HOMO levels to be as low as -5.60eV for PTIFBDT. The highest hole mobility was measured to be 0.0044 $cm^2V^{-1}s^{-1}$ and 0.0026 $cm^2V^{-1}s^{-1}$ for PTIBDT and PTIFBDT, respectively. PTIFBDT with introduced electron-withdrawing fluorine atom still exhibits very large threshold voltage (V_{th}) meaning massive hole traps due to the rich electron cloud of indolin-2-one unit. For the OPV results, PTIBDT achieved the highest PCE of 8% with the V_{oc} of 0.97V, and PTIFBDT showed a comparable high PCE of 7.7% with even higher V_{oc} of 1V when ITIC

was used as acceptor material. The high PCE results were mainly due to the very low-lying HOMO levels of two polymers compared with PTIBT. However, the very amorphous property and homogeneously mixed film morphology with very small size of domains causing inefficient exciton diffusion and charge transport, and thus relatively low J_{sc} and FF values limiting the further enhancement of PCE. Consequently, on the one hand, the future work should focus on the improvement of crystallinity by different structural modifications such as chlorination [116] or introduction of ester functional group. On the other hand, various NFA materials like recently reported advantageous NFA molecule, Y6, can be tried to replace ITIC to optimize the J_{sc} and FF of OPV devices.

In chapter 3, another strong electron-withdrawing carbonyl functional group was introduced to further develop Type II D-A copolymers of PTIABDT with acetyl group and PTIPBDT with propionyl group to improve the hole trapping problem. Both polymers showed slightly decreased band gaps to around 1.83eV and comparable low-lying HOMO levels with PTIPBDT demonstrating the lowest HOMO of -5.63eV when compared with PTIBDT and PTIFBDT in chapter 2. PTIPBDT with longer side chain was developed since PTIABDT exhibited low processability in common organic solvents at room temperature. The OFET hole mobility of PTIABDT was found to be up to 0.015 $cm^2V^{-1}s^{-1}$ with very low threshold voltage (V_{th}) close to zero since the carbonyl group could withdraw the free pair of electrons from nitrogen atom of indolin-2-one structure achieving less hole trapping. PTIPBDT still exhibits relatively large V_{th} which might be attributed to the partially removed propionyl groups during polymerization process. OSCs based on PTIABDT:ITIC showed a PCE of 3.99% and 3.29% for PTIPBDT:ITIC with superior high V_{oc} of 1.05V due to the low-lying HOMO levels. Although PCE was increased to 4.48% for PTIABDT:IT-4F active layer when IT-4F was applied as acceptor, these polymers

still demonstrated low J_{sc} and FF as a result of low crystallinity and not optimized miscibility and phase separation between donor polymers and NFA materials which are not favored for exciton generation and diffusion. For the future direction, again novel chemistry designs which can promote the polymer crystallinity are expected, and the advantageous OFET performance of PTIABDT with high on-current (I_{on}) and low V_{th} making it promising as sensing platform for the detection of temperature change since similar conjugated polymer containing indolin-2-one has been investigated to show sensitivity to temperature change enabling it as active layer in temperature sensor.

Lastly in chapter 4, the design and synthesis of water-soluble conjugated polymers based on isoindigo structure have been discussed to meet the urgent needs for green-solvent-processable organic semiconductors which can be applied in various organic electronics. The water-soluble anionic ID monomer with butyl sulfonate side chain was synthesised, and the monomer was converted to organic solvent-soluble monomer with organic tetra-phenylphosphonium group so that Stille-coupling polymerization could proceed in DMF solvent with this monomer. The final product of PIDBT will be further characterized to investigate its physical, optical and electrochemical properties to compare with its counterpart polymer with normal organic alkyl side chain and to be further applied in OPV applications.

Bibliography

(1) Cai, Y.; Huo, L.; Sun, Y. Recent Advances in Wide-Bandgap Photovoltaic Polymers. *Adv. Mater.* **2017**, *29* (22), 1605437. https://doi.org/10.1002/adma.201605437.

(2) Fu, H.; Wang, Z.; Sun, Y. Polymer Donors for High-Performance Non-Fullerene Organic Solar Cells. *Angew. Chem. Int. Ed.* **2019**, *58* (14), 4442–4453. https://doi.org/10.1002/anie.201806291.

(3) Li, Y. Molecular Design of Photovoltaic Materials for Polymer Solar Cells: Toward Suitable Electronic Energy Levels and Broad Absorption. *Acc. Chem. Res.* **2012**, *45* (5), 723–733. https://doi.org/10.1021/ar2002446.

(4) Wang, G.; Melkonyan, F. S.; Facchetti, A.; Marks, T. J. All-Polymer Solar Cells: Recent Progress, Challenges, and Prospects. *Angew. Chem. Int. Ed.* **2019**, *58* (13), 4129–4142. https://doi.org/10.1002/anie.201808976.

(5) Li, Z.; Jiang, K.; Yang, G.; Lai, J. Y. L.; Ma, T.; Zhao, J.; Ma, W.; Yan, H. Donor Polymer Design Enables Efficient Non-Fullerene Organic Solar Cells. *Nat Commun* **2016**, *7* (1), 13094. https://doi.org/10.1038/ncomms13094.

(6) Tang, C. W. Two-layer Organic Photovoltaic Cell. *Appl. Phys. Lett.* **1986**, *48* (2), 183–185. https://doi.org/10.1063/1.96937.

(7) Liang, Y.; Yu, L. A New Class of Semiconducting Polymers for Bulk Heterojunction Solar Cells with Exceptionally High Performance. *Acc. Chem. Res.* **2010**, *43* (9), 1227–1236. https://doi.org/10.1021/ar1000296.

(8) Xue, J.; Uchida, S.; Rand, B. P.; Forrest, S. R. 4.2% Efficient Organic Photovoltaic Cells with Low Series Resistances. *Appl. Phys. Lett.* **2004**, *84* (16), 3013–3015. https://doi.org/10.1063/1.1713036.

(9) Yu, G.; Gao, J.; Hummelen, J. C.; Wudl, F.; Heeger, A. J. Polymer Photovoltaic Cells: Enhanced Efficiencies via a Network of Internal Donor-Acceptor Heterojunctions. *Science* **1995**, *270* (5243), 1789–1791. https://doi.org/10.1126/science.270.5243.1789.

(10) Günes, S.; Neugebauer, H.; Sariciftci, N. S. Conjugated Polymer-Based Organic Solar Cells. *Chem. Rev.* **2007**, *107* (4), 1324–1338. https://doi.org/10.1021/cr050149z.

(11) Clarke, T. M.; Durrant, J. R. Charge Photogeneration in Organic Solar Cells. *Chem. Rev.* **2010**, *110* (11), 6736–6767. https://doi.org/10.1021/cr900271s.

(12) Zhou, H.; Yang, L.; You, W. Rational Design of High Performance Conjugated Polymers for Organic Solar Cells. *Macromolecules* **2012**, *45* (2), 607–632. https://doi.org/10.1021/ma201648t.

(13) Brabec, C. J.; Sariciftci, N. S.; Hummelen, J. C. Plastic Solar Cells. *Adv. Funct. Mater.* **2001**, No. 1, 12.

(14) Şahin, Y.; Alem, S.; de Bettignies, R.; Nunzi, J.-M. Development of Air Stable Polymer Solar Cells Using an Inverted Gold on Top Anode Structure. *Thin Solid Films* **2005**, *476* (2), 340–343. https://doi.org/10.1016/j.tsf.2004.10.018.

(15) Oseni, S. O.; Mola, G. T. Properties of Functional Layers in Inverted Thin Film Organic Solar Cells. *Solar Energy Materials and Solar Cells* **2017**, *160*, 241–256. https://doi.org/10.1016/j.solmat.2016.10.036.

(16) Shrotriya, V.; Li, G.; Yao, Y.; Chu, C.-W.; Yang, Y. Transition Metal Oxides as the Buffer Layer for Polymer Photovoltaic Cells. *Appl. Phys. Lett.* **2006**, *88* (7), 073508. https://doi.org/10.1063/1.2174093.

(17) Wadsworth, A.; Moser, M.; Marks, A.; Little, M. S.; Gasparini, N.; Brabec, C. J.; Baran, D.; McCulloch, I. Critical Review of the Molecular Design Progress in Non-Fullerene Electron Acceptors towards Commercially Viable Organic Solar Cells. *Chem. Soc. Rev.* **2019**, *48* (6), 1596–1625. https://doi.org/10.1039/C7CS00892A.

(18) Blom, P. W. M.; Mihailetchi, V. D.; Koster, L. J. A.; Markov, D. E. Device Physics of Polymer:Fullerene Bulk Heterojunction Solar Cells. *Adv. Mater.* **2007**, *19* (12), 1551–1566. https://doi.org/10.1002/adma.200601093.

(19) Stoltzfus, D. M.; Donaghey, J. E.; Armin, A.; Shaw, P. E.; Burn, P. L.; Meredith, P. Charge Generation Pathways in Organic Solar Cells: Assessing the Contribution from the Electron Acceptor. *Chem. Rev.* **2016**, *116* (21), 12920–12955. https://doi.org/10.1021/acs.chemrev.6b00126.

(20) Cheng, P.; Li, G.; Zhan, X.; Yang, Y. Next-Generation Organic Photovoltaics Based on Non-Fullerene Acceptors. *Nature Photon* **2018**, *12* (3), 131–142. https://doi.org/10.1038/s41566-018-0104-9.

(21) Elumalai, N. K.; Uddin, A. Open Circuit Voltage of Organic Solar Cells: An in-Depth Review. *Energy Environ. Sci.* **2016**, *9* (2), 391–410. https://doi.org/10.1039/C5EE02871J.

(22) Scharber, M. C.; Mühlbacher, D.; Koppe, M.; Denk, P.; Waldauf, C.; Heeger, A. J.; Brabec, C. J. Design Rules for Donors in Bulk-Heterojunction Solar Cells—Towards

10 % Energy-Conversion Efficiency. *Adv. Mater.* **2006**, *18* (6), 789–794. https://doi.org/10.1002/adma.200501717.

(23) Yeboah, D.; Singh, J. Study of the Contributions of Donor and Acceptor Photoexcitations to Open Circuit Voltage in Bulk Heterojunction Organic Solar Cells. *Electronics* **2017**, *6* (4), 75. https://doi.org/10.3390/electronics6040075.

(24) Hummelen, J. C.; Knight, B. W.; LePeq, F.; Wudl, F.; Yao, J.; Wilkins, C. L. Preparation and Characterization of Fulleroid and Methanofullerene Derivatives. *J. Org. Chem.* **1995**, *60* (3), 532–538. https://doi.org/10.1021/jo00108a012.

(25) Wienk, M. M.; Kroon, J. M.; Verhees, W. J. H.; Knol, J.; Hummelen, J. C.; van Hal, P. A.; Janssen, R. A. J. Efficient Methano[70]Fullerene/MDMO-PPV Bulk Heterojunction Photovoltaic Cells. *Angew. Chem. Int. Ed.* **2003**, *42* (29), 3371–3375. https://doi.org/10.1002/anie.200351647.

(26) Brunetti, F. G.; Kumar, R.; Wudl, F. Organic Electronics from Perylene to Organic Photovoltaics: Painting a Brief History with a Broad Brush. *J. Mater. Chem.* **2010**, *20* (15), 2934. https://doi.org/10.1039/b921677d.

(27) Zhao, J.; Li, Y.; Yang, G.; Jiang, K.; Lin, H.; Ade, H.; Ma, W.; Yan, H. Efficient Organic Solar Cells Processed from Hydrocarbon Solvents. *Nat Energy* **2016**, *1* (2), 15027. https://doi.org/10.1038/nenergy.2015.27.

(28) Zhan, X.; Tan, Z.; Domercq, B.; An, Z.; Zhang, X.; Barlow, S.; Li, Y.; Zhu, D.; Kippelen, B.; Marder, S. R. A High-Mobility Electron-Transport Polymer with Broad Absorption and Its Use in Field-Effect Transistors and All-Polymer Solar Cells. *J. Am. Chem. Soc.* **2007**, *129* (23), 7246–7247. https://doi.org/10.1021/ja071760d.

(29) Cheng, P.; Zhan, X. Stability of Organic Solar Cells: Challenges and Strategies. *Chem. Soc. Rev.* **2016**, *45* (9), 2544–2582. https://doi.org/10.1039/C5CS00593K.

(30) Jørgensen, M.; Norrman, K.; Gevorgyan, S. A.; Tromholt, T.; Andreasen, B.; Krebs, F. C. Stability of Polymer Solar Cells. *Adv. Mater.* **2012**, *24* (5), 580–612. https://doi.org/10.1002/adma.201104187.

(31) Speller, E. M.; Clarke, A. J.; Luke, J.; Lee, H. K. H.; Durrant, J. R.; Li, N.; Wang, T.; Wong, H. C.; Kim, J.-S.; Tsoi, W. C.; Li, Z. From Fullerene Acceptors to Non-Fullerene Acceptors: Prospects and Challenges in the Stability of Organic Solar Cells. *J. Mater. Chem. A* **2019**, *7* (41), 23361–23377. https://doi.org/10.1039/C9TA05235F.

(32) Xu, X.; Zhang, G.; Li, Y.; Peng, Q. The Recent Progress of Wide Bandgap Donor Polymers towards Non-Fullerene Organic Solar Cells. *Chinese Chemical Letters* **2019**, *30* (4), 809–825. https://doi.org/10.1016/j.cclet.2019.02.030.

(33) Duan, L.; Elumalai, N. K.; Zhang, Y.; Uddin, A. Progress in Non-Fullerene Acceptor Based Organic Solar Cells. *Solar Energy Materials and Solar Cells* **2019**, *193*, 22–65. https://doi.org/10.1016/j.solmat.2018.12.033.

(34) Meng, L.; Zhang, Y.; Wan, X.; Li, C.; Zhang, X.; Wang, Y.; Ke, X.; Xiao, Z.; Ding, L.; Xia, R.; Yip, H.-L.; Cao, Y.; Chen, Y. Organic and Solution-Processed Tandem Solar Cells with 17.3% Efficiency. *Science* **2018**, *361* (6407), 1094–1098. https://doi.org/10.1126/science.aat2612.

(35) Lin, Y.; Wang, J.; Zhang, Z.-G.; Bai, H.; Li, Y.; Zhu, D.; Zhan, X. An Electron Acceptor Challenging Fullerenes for Efficient Polymer Solar Cells. *Adv. Mater.* **2015**, *27* (7), 1170–1174. https://doi.org/10.1002/adma.201404317.

(36) Xie, Y.; Wu, H. Balancing Charge Generation and Voltage Loss toward Efficient Nonfullerene Organic Solar Cells. *Materials Today Advances* **2020**, *5*, 100048. https://doi.org/10.1016/j.mtadv.2019.100048.

(37) Li, X.; Huang, G.; Zheng, N.; Li, Y.; Kang, X.; Qiao, S.; Jiang, H.; Chen, W.; Yang, R. High-Efficiency Polymer Solar Cells Over 13.9% With a High VOC Beyond 1.0 V by Synergistic Effect of Fluorine and Sulfur. *Solar RRL* **2019**, *3* (4), 1900005. https://doi.org/10.1002/solr.201900005.

(38) Lin, Y.; Zhao, F.; He, Q.; Huo, L.; Wu, Y.; Parker, T. C.; Ma, W.; Sun, Y.; Wang, C.; Zhu, D.; Heeger, A. J.; Marder, S. R.; Zhan, X. High-Performance Electron Acceptor with Thienyl Side Chains for Organic Photovoltaics. *J. Am. Chem. Soc.* **2016**, *138* (14), 4955–4961. https://doi.org/10.1021/jacs.6b02004.

(39) Zhao, W.; Li, S.; Yao, H.; Zhang, S.; Zhang, Y.; Yang, B.; Hou, J. Molecular Optimization Enables over 13% Efficiency in Organic Solar Cells. *J. Am. Chem. Soc.* **2017**, *139* (21), 7148–7151. https://doi.org/10.1021/jacs.7b02677.

(40) Yuan, J.; Zhang, Y.; Zhou, L.; Zhang, G.; Yip, H.-L.; Lau, T.-K.; Lu, X.; Zhu, C.; Peng, H.; Johnson, P. A.; Leclerc, M.; Cao, Y.; Ulanski, J.; Li, Y.; Zou, Y. Single-Junction Organic Solar Cell with over 15% Efficiency Using Fused-Ring Acceptor with Electron-Deficient Core. *Joule* **2019**, *3* (4), 1140–1151. https://doi.org/10.1016/j.joule.2019.01.004.

(41) Lu, L.; Zheng, T.; Wu, Q.; Schneider, A. M.; Zhao, D.; Yu, L. Recent Advances in Bulk Heterojunction Polymer Solar Cells. *Chem. Rev.* **2015**, *115* (23), 12666–12731. https://doi.org/10.1021/acs.chemrev.5b00098.

(42) Hou, J.; Park, M.-H.; Zhang, S.; Yao, Y.; Chen, L.-M.; Li, J.-H.; Yang, Y. Bandgap and Molecular Energy Level Control of Conjugated Polymer Photovoltaic Materials Based on Benzo[1,2- *b* :4,5- *b* ′]Dithiophene. *Macromolecules* **2008**, *41* (16), 6012–6018. https://doi.org/10.1021/ma800820r.

(43) Firdaus, Y.; Maffei, L. P.; Cruciani, F.; Müller, M. A.; Liu, S.; Lopatin, S.; Wehbe, N.; Ndjawa, G. O. N.; Amassian, A.; Laquai, F.; Beaujuge, P. M. Polymer Main-Chain Substitution Effects on the Efficiency of Nonfullerene BHJ Solar Cells. *Advanced Energy Materials* **2017**, *7* (21), 1700834. https://doi.org/10.1002/aenm.201700834.

(44) Li, S.; Ye, L.; Zhao, W.; Yan, H.; Yang, B.; Liu, D.; Li, W.; Ade, H.; Hou, J. A Wide Band Gap Polymer with a Deep Highest Occupied Molecular Orbital Level Enables 14.2% Efficiency in Polymer Solar Cells. *J. Am. Chem. Soc.* **2018**, *140* (23), 7159–7167. https://doi.org/10.1021/jacs.8b02695.

(45) Campana, F.; Kim, C.; Marrocchi, A.; Vaccaro, L. Green Solvent-Processed Organic Electronic Devices. *J. Mater. Chem. C* **2020**, 10.1039.D0TC03610B. https://doi.org/10.1039/D0TC03610B.

(46) Kim, G.; Kang, S.-J.; Dutta, G. K.; Han, Y.-K.; Shin, T. J.; Noh, Y.-Y.; Yang, C. A Thienoisoindigo-Naphthalene Polymer with Ultrahigh Mobility of 14.4 $Cm^2/V{\cdot}s$ That Substantially Exceeds Benchmark Values for Amorphous Silicon Semiconductors. *J. Am. Chem. Soc.* **2014**, *136* (26), 9477–9483. https://doi.org/10.1021/ja504537v.

(47) Kang, I.; Yun, H.-J.; Chung, D. S.; Kwon, S.-K.; Kim, Y.-H. Record High Hole Mobility in Polymer Semiconductors via Side-Chain Engineering. *J. Am. Chem. Soc.* **2013**, *135* (40), 14896–14899. https://doi.org/10.1021/ja405112s.

(48) Ma, Z.; Zhao, B.; Gong, Y.; Deng, J.; Tan, Z. Green-Solvent-Processable Strategies for Achieving Large-Scale Manufacture of Organic Photovoltaics. *J. Mater. Chem. A* **2019**, *7* (40), 22826–22847. https://doi.org/10.1039/C9TA09277C.

(49) Ha, S.; Seidle, T.; Lim, K.-M. Act on the Registration and Evaluation of Chemicals (K-REACH) and Replacement, Reduction or Refinement Best Practices. *Environmental Health and Toxicology* 9.

(50) McDowell, C.; Bazan, G. C. Organic Solar Cells Processed from Green Solvents. *Current Opinion in Green and Sustainable Chemistry* **2017**, *5*, 49–54. https://doi.org/10.1016/j.cogsc.2017.03.007.

(51) Duan, C.; Zhang, K.; Zhong, C.; Huang, F.; Cao, Y. Recent Advances in Water/Alcohol-Soluble π-Conjugated Materials: New Materials and Growing Applications in Solar Cells. *Chem. Soc. Rev.* **2013**, *42* (23), 9071–9104. https://doi.org/10.1039/C3CS60200A.

(52) Zhao, Y.; Xie, Z.; Qin, C.; Qu, Y.; Geng, Y.; Wang, L. Enhanced Charge Collection in Polymer Photovoltaic Cells by Using an Ethanol-Soluble Conjugated Polyfluorene as Cathode Buffer Layer. *Solar Energy Materials and Solar Cells* **2009**, *93* (5), 604–608. https://doi.org/10.1016/j.solmat.2008.12.007.

(53) Meng, B.; Fu, Y.; Xie, Z.; Liu, J.; Wang, L. Phosphonated Conjugated Polymers for Polymer Solar Cells with a Non-Halogenated Solvent Process. *Polym. Chem.* **2015**, *6* (5), 805–812. https://doi.org/10.1039/C4PY01294A.

(54) Nguyen, T. L.; Lee, C.; Kim, H.; Kim, Y.; Lee, W.; Oh, J. H.; Kim, B. J.; Woo, H. Y. Ethanol-Processable, Highly Crystalline Conjugated Polymers for Eco-Friendly Fabrication of Organic Transistors and Solar Cells. *Macromolecules* **2017**, *50* (11), 4415–4424. https://doi.org/10.1021/acs.macromol.7b00452.

(55) Li, S.; Zhang, H.; Zhao, W.; Ye, L.; Yao, H.; Yang, B.; Zhang, S.; Hou, J. Green-Solvent-Processed All-Polymer Solar Cells Containing a Perylene Diimide-Based Acceptor with an Efficiency over 6.5%. *Advanced Energy Materials* **2016**, *6* (5), 1501991. https://doi.org/10.1002/aenm.201501991.

(56) Wang, G.-J. N.; Molina-Lopez, F.; Zhang, H.; Xu, J.; Wu, H.-C.; Lopez, J.; Shaw, L.; Mun, J.; Zhang, Q.; Wang, S.; Ehrlich, A.; Bao, Z. Nonhalogenated Solvent Processable and Printable High-Performance Polymer Semiconductor Enabled by Isomeric Nonconjugated Flexible Linkers. *Macromolecules* **2018**, *51* (13), 4976–4985. https://doi.org/10.1021/acs.macromol.8b00971.

(57) Teng, Q. Instrumentation. In *Structural Biology*; Springer US: Boston, MA, 2013; pp 65–101. https://doi.org/10.1007/978-1-4614-3964-6_2.

(58) Moore, J. C. Gel Permeation Chromatography. I. A New Method for Molecular Weight Distribution of High Polymers. *Journal of Polymer Science Part A: General Papers* **1964**, *2* (2), 835–843. https://doi.org/10.1002/pol.1964.100020220.

(59) Kasper, M. G.W.H. Höhne, W.F. Hemminger, H.-J. Flammersheim: Differential Scanning Calorimetry. *Anal Bioanal Chem* **2004**, *380* (3), 366–367. https://doi.org/10.1007/s00216-004-2814-8.

(60) Costa, J. C. S.; Taveira, R. J. S.; Lima, C. F. R. A. C.; Mendes, A.; Santos, L. M. N. B. F. Optical Band Gaps of Organic Semiconductor Materials. *Optical Materials* **2016**, *58*, 51–60. https://doi.org/10.1016/j.optmat.2016.03.041.

(61) Bard, A. J. *Electrochemical Methods: Fundamentals and Applications*, 2nd ed.; John Wiley: New York, 2001.

(62) Binnig, G.; Quate, C. F.; Gerber, Ch. Atomic Force Microscope. *Phys. Rev. Lett.* **1986**, *56* (9), 930–933. https://doi.org/10.1103/PhysRevLett.56.930.

(63) Birkholz, M.; Fewster, P. F.; Genzel, C. *Thin Film Analysis by X-Ray Scattering*; Wiley-VCH: Weinheim, 2006.

(64) Qin, Y.; Uddin, M. A.; Chen, Y.; Jang, B.; Zhao, K.; Zheng, Z.; Yu, R.; Shin, T. J.; Woo, H. Y.; Hou, J. Highly Efficient Fullerene-Free Polymer Solar Cells Fabricated with Polythiophene Derivative. *Advanced Materials* **2016**, *28* (42), 9416–9422. https://doi.org/10.1002/adma.201601803.

(65) Roncali, J. Synthetic Principles for Bandgap Control in Linear π-Conjugated Systems. *Chem. Rev.* **1997**, *97* (1), 173–206. https://doi.org/10.1021/cr950257t.

(66) He, K.; Li, X.; Liu, H.; Zhang, Z.; Kumar, P.; Ngai, J. H. L.; Wang, J.; Li, Y. D-A Polymer with a Donor Backbone - Acceptor-side-chain Structure for Organic Solar Cells. *Asian J. Org. Chem.* **2020**, ajoc.202000172. https://doi.org/10.1002/ajoc.202000172.

(67) Chen, H.; Hu, Z.; Wang, H.; Liu, L.; Chao, P.; Qu, J.; Chen, W.; Liu, A.; He, F. A Chlorinated π-Conjugated Polymer Donor for Efficient Organic Solar Cells. *Joule* **2018**, *2* (8), 1623–1634. https://doi.org/10.1016/j.joule.2018.05.010.

(68) Huo, L.; Zhang, S.; Guo, X.; Xu, F.; Li, Y.; Hou, J. Replacing Alkoxy Groups with Alkylthienyl Groups: A Feasible Approach To Improve the Properties of Photovoltaic Polymers. *Angew. Chem. Int. Ed.* **2011**, *50* (41), 9697–9702. https://doi.org/10.1002/anie.201103313.

(69) Li, Z.; Jiang, K.; Yang, G.; Lai, J. Y. L.; Ma, T.; Zhao, J.; Ma, W.; Yan, H. Donor Polymer Design Enables Efficient Non-Fullerene Organic Solar Cells. *Nat Commun* **2016**, *7* (1), 13094. https://doi.org/10.1038/ncomms13094.

(70) Firdaus, Y.; Maffei, L. P.; Cruciani, F.; Müller, M. A.; Liu, S.; Lopatin, S.; Wehbe, N.; Ndjawa, G. O. N.; Amassian, A.; Laquai, F.; Beaujuge, P. M. Polymer Main-Chain Substitution Effects on the Efficiency of Nonfullerene BHJ Solar Cells. *Adv. Energy Mater.* **2017**, *7* (21), 1700834. https://doi.org/10.1002/aenm.201700834.

(71) Bauer, N.; Zhang, Q.; Zhu, J.; Peng, Z.; Yan, L.; Zhu, C.; Ade, H.; Zhan, X.; You, W. Donor Polymer Fluorination Doubles the Efficiency in Non-Fullerene Organic Photovoltaics. *J. Mater. Chem. A* **2017**, *5* (43), 22536–22541. https://doi.org/10.1039/C7TA07882J.

(72) Do, K.; Saleem, Q.; Ravva, M. K.; Cruciani, F.; Kan, Z.; Wolf, J.; Hansen, M. R.; Beaujuge, P. M.; Brédas, J.-L. Impact of Fluorine Substituents on π-Conjugated Polymer Main-Chain Conformations, Packing, and Electronic Couplings. *Advanced Materials* **2016**, *28* (37), 8197–8205. https://doi.org/10.1002/adma.201601282.

(73) Li, Z.; Lin, H.; Jiang, K.; Carpenter, J.; Li, Y.; Liu, Y.; Hu, H.; Zhao, J.; Ma, W.; Ade, H.; Yan, H. Dramatic Performance Enhancement for Large Bandgap Thick-Film Polymer Solar Cells Introduced by a Difluorinated Donor Unit. *Nano Energy* **2015**, *15*, 607–615. https://doi.org/10.1016/j.nanoen.2015.05.016.

(74) Nguyen, T. L.; Choi, H.; Ko, S.-J.; Uddin, M. A.; Walker, B.; Yum, S.; Jeong, J.-E.; Yun, M. H.; Shin, T. J.; Hwang, S.; Kim, J. Y.; Woo, H. Y. Semi-Crystalline Photovoltaic Polymers with Efficiency Exceeding 9% in a ~300 Nm Thick Conventional

Single-Cell Device. *Energy Environ. Sci.* **2014**, *7* (9), 3040–3051. https://doi.org/10.1039/C4EE01529K.

(75) Liu, J.; Ma, L.-K.; Li, Z.; Hu, H.; Sheong, F. K.; Zhang, G.; Ade, H.; Yan, H. Donor Polymer Based on Alkylthiophene Side Chains for Efficient Non-Fullerene Organic Solar Cells: Insights into Fluorination and Side Chain Effects on Polymer Aggregation and Blend Morphology. *J. Mater. Chem. A* **2018**, *6* (46), 23270–23277. https://doi.org/10.1039/C8TA08769E.

(76) Zhang, M.; Guo, X.; Ma, W.; Ade, H.; Hou, J. A Large-Bandgap Conjugated Polymer for Versatile Photovoltaic Applications with High Performance. *Adv. Mater.* **2015**, *27* (31), 4655–4660. https://doi.org/10.1002/adma.201502110.

(77) Yang, J.; Uddin, M. A.; Tang, Y.; Wang, Y.; Wang, Y.; Su, H.; Gao, R.; Chen, Z.-K.; Dai, J.; Woo, H. Y.; Guo, X. Quinoxaline-Based Wide Band Gap Polymers for Efficient Nonfullerene Organic Solar Cells with Large Open-Circuit Voltages. *ACS Appl. Mater. Interfaces* **2018**, *10* (27), 23235–23246. https://doi.org/10.1021/acsami.8b04432.

(78) Li, S.; Yuan, Z.; Yuan, J.; Deng, P.; Zhang, Q.; Sun, B. An Expanded Isoindigo Unit as a New Building Block for a Conjugated Polymer Leading to High-Performance Solar Cells. *J. Mater. Chem. A* **2014**, *2* (15), 5427–5433. https://doi.org/10.1039/C3TA15291J.

(79) Wang, E.; Ma, Z.; Zhang, Z.; Henriksson, P.; Inganäs, O.; Zhang, F.; Andersson, M. R. An Isoindigo-Based Low Band Gap Polymer for Efficient Polymer Solar Cells with High Photo-Voltage. *Chem. Commun.* **2011**, *47* (17), 4908–4910. https://doi.org/10.1039/C1CC11053E.

(80) Kang, X.; Li, X.; Liu, H.; Liang, Z.; Chen, W.; Zheng, N.; Qiao, S.; Yang, R. Aggregation Tuning with Heavily Fluorinated Donor Polymer for Efficient Organic Solar Cells. *ACS Appl. Mater. Interfaces* **2020**. https://doi.org/10.1021/acsami.0c10658.

(81) Wang, N.; Zhang, S.; Zhao, R.; Feng, J.; Ding, Z.; Ma, W.; Hu, J.; Liu, J. Designed Polymer Donors to Match an Amorphous Polymer Acceptor in All-Polymer Solar Cells. *ACS Appl. Electron. Mater.* **2020**, *2* (7), 2274–2281. https://doi.org/10.1021/acsaelm.0c00451.

(82) Tran, D. K.; Kolhe, N. B.; Hwang, Y.; Kuzuhara, D.; Koganezawa, T.; Jenekhe, S. A. Effects of a Fluorinated Donor Polymer on the Morphology, Photophysics, and Performance of All-Polymer Solar Cells Based on Naphthalene Diimide–Arylene Copolymer Acceptors. *ACS Appl. Mater. Interfaces* **2020**, *12* (14), 16490–16502. https://doi.org/10.1021/acsami.0c01382.

(83) Wu, J.; Chen, J.; Huang, H.; Li, S.; Wu, H.; Hu, C.; Tang, J.; Zhang, Q. (*Z*)-(Thienylmethylene)Oxindole-Based Polymers for High-Performance Solar Cells. *Macromolecules* **2016**, *49* (6), 2145–2152. https://doi.org/10.1021/acs.macromol.5b02780.

(84) Kim, M.; Ryu, S. U.; Park, S. A.; Choi, K.; Kim, T.; Chung, D.; Park, T. Donor–Acceptor-Conjugated Polymer for High-Performance Organic Field-Effect Transistors: A Progress Report. *Advanced Functional Materials* **2020**, *30* (20), 1904545. https://doi.org/10.1002/adfm.201904545.

(85) Chen, J.-D.; Cui, C.; Li, Y.-Q.; Zhou, L.; Ou, Q.-D.; Li, C.; Li, Y.; Tang, J.-X. Polymer Solar Cells: Single-Junction Polymer Solar Cells Exceeding 10% Power Conversion

Efficiency (Adv. Mater. 6/2015). *Advanced Materials* **2015**, *27* (6), 1132–1132. https://doi.org/10.1002/adma.201570040.

(86) Vohra, V.; Kawashima, K.; Kakara, T.; Koganezawa, T.; Osaka, I.; Takimiya, K.; Murata, H. Efficient Inverted Polymer Solar Cells Employing Favourable Molecular Orientation. *Nature Photonics* **2015**, *9* (6), 403–408. https://doi.org/10.1038/nphoton.2015.84.

(87) Sun, C.; Qin, S.; Wang, R.; Chen, S.; Pan, F.; Qiu, B.; Shang, Z.; Meng, L.; Zhang, C.; Xiao, M.; Yang, C.; Li, Y. High Efficiency Polymer Solar Cells with Efficient Hole Transfer at Zero Highest Occupied Molecular Orbital Offset between Methylated Polymer Donor and Brominated Acceptor. *J. Am. Chem. Soc.* **2020**, *142* (3), 1465–1474. https://doi.org/10.1021/jacs.9b09939.

(88) Yao, H.; Cui, Y.; Qian, D.; Ponseca, C. S.; Honarfar, A.; Xu, Y.; Xin, J.; Chen, Z.; Hong, L.; Gao, B.; Yu, R.; Zu, Y.; Ma, W.; Chabera, P.; Pullerits, T.; Yartsev, A.; Gao, F.; Hou, J. 14.7% Efficiency Organic Photovoltaic Cells Enabled by Active Materials with a Large Electrostatic Potential Difference. *J. Am. Chem. Soc.* **2019**, *141* (19), 7743–7750. https://doi.org/10.1021/jacs.8b12937.

(89) Zhang, Z. Development of Low-cost Organic Solar Cells Using Polythiophenes as Donors. 112.

(90) Li, G.; Shrotriya, V.; Huang, J.; Yao, Y.; Moriarty, T.; Emery, K.; Yang, Y. High-Efficiency Solution Processable Polymer Photovoltaic Cells by Self-Organization of Polymer Blends. *Nature Materials* **2005**, *4* (11), 864–868. https://doi.org/10.1038/nmat1500.

(91) Li, Z.; Xu, X.; Zhang, G.; Yu, T.; Li, Y.; Peng, Q. Highly Efficient Non-Fullerene Polymer Solar Cells Enabled by Wide Bandgap Copolymers With Conjugated Selenyl Side Chains. *Solar RRL* **2018**, *2* (10), 1800186. https://doi.org/10.1002/solr.201800186.

(92) Su, W.; Fan, Q.; Guo, X.; Meng, X.; Bi, Z.; Ma, W.; Zhang, M.; Li, Y. Two Compatible Nonfullerene Acceptors with Similar Structures as Alloy for Efficient Ternary Polymer Solar Cells. *Nano Energy* **2017**, *38*, 510–517. https://doi.org/10.1016/j.nanoen.2017.05.060.

(93) Zhang, L.; Deng, W.; Wu, B.; Ye, L.; Sun, X.; Wang, Z.; Gao, K.; Wu, H.; Duan, C.; Huang, F.; Cao, Y. Reduced Energy Loss in Non-Fullerene Organic Solar Cells with Isomeric Donor Polymers Containing Thiazole π-Spacers. *ACS Appl. Mater. Interfaces* **2020**, *12* (1), 753–762. https://doi.org/10.1021/acsami.9b18048.

(94) Xu, X.; Feng, K.; Lee, Y. W.; Woo, H. Y.; Zhang, G.; Peng, Q. Subtle Polymer Donor and Molecular Acceptor Design Enable Efficient Polymer Solar Cells with a Very Small Energy Loss. *Advanced Functional Materials* **2020**, *30* (9), 1907570. https://doi.org/10.1002/adfm.201907570.

(95) Wang, Z.; Zhang, F.; Li, L.; An, Q.; Wang, J.; Zhang, J. The Underlying Reason of DIO Additive on the Improvement Polymer Solar Cells Performance. *Applied Surface Science* **2014**, *305*, 221–226. https://doi.org/10.1016/j.apsusc.2014.03.041.

(96) Hou, J.; Chen, H.-Y.; Zhang, S.; Chen, R. I.; Yang, Y.; Wu, Y.; Li, G. Synthesis of a Low Band Gap Polymer and Its Application in Highly Efficient Polymer Solar Cells. *J. Am. Chem. Soc.* **2009**, *131* (43), 15586–15587. https://doi.org/10.1021/ja9064975.

(97) Liang, Y.; Feng, D.; Wu, Y.; Tsai, S.-T.; Li, G.; Ray, C.; Yu, L. Highly Efficient Solar Cell Polymers Developed via Fine-Tuning of Structural and Electronic Properties. *J. Am. Chem. Soc.* **2009**, *131* (22), 7792–7799. https://doi.org/10.1021/ja901545q.

(98) Nugent, J.; Shire, B. R.; Caputo, D. F. J.; Pickford, H. D.; Nightingale, F.; Houlsby, I. T. T.; Mousseau, J. J.; Anderson, E. A. Synthesis of All-Carbon Disubstituted Bicyclo[1.1.1]Pentanes by Iron-Catalyzed Kumada Cross-Coupling. *Angewandte Chemie International Edition* **2020**, *59* (29), 11866–11870. https://doi.org/10.1002/anie.202004090.

(99) Tong, J.; An, L.; Li, J.; Lv, J.; Guo, P.; Li, L.; Zhang, P.; Yang, C.; Xia, Y.; Wang, C. Effects of Alkyl Side Chain Length of Low Bandgap Naphtho[1,2-c:5,6-C′]Bis[1,2,5]Thiadiazole-Based Copolymers on the Optoelectronic Properties of Polymer Solar Cells. *Journal of Polymer Science Part A: Polymer Chemistry* **2018**, *56* (18), 2059–2071. https://doi.org/10.1002/pola.29166.

(100) Beach, E. S.; Cui, Z.; Anastas, P. T. Green Chemistry: A Design Framework for Sustainability. *Energy Environ. Sci.* **2009**, *2* (10), 1038. https://doi.org/10.1039/b904997p.

(101) Huang, F.; Hou, L.; Wu, H.; Wang, X.; Shen, H.; Cao, W.; Yang, W.; Cao, Y. High-Efficiency, Environment-Friendly Electroluminescent Polymers with Stable High Work Function Metal as a Cathode: Green- and Yellow-Emitting Conjugated Polyfluorene Polyelectrolytes and Their Neutral Precursors. *J. Am. Chem. Soc.* **2004**, *126* (31), 9845–9853. https://doi.org/10.1021/ja0476765.

(102) Li, Y. Self-Doped n-Type Water/Alcohol-Soluble Conjugated Polymers ETL for High-Performance Polymer and Perovskite Solar Cells. *Sci. China Chem.* **2016**, *59* (11), 1430–1431. https://doi.org/10.1007/s11426-016-0152-y.

(103) Jo, J. W.; Jung, J. W.; Bae, S.; Ko, M. J.; Kim, H.; Jo, W. H.; Jen, A. K.-Y.; Son, H. J. Development of Self-Doped Conjugated Polyelectrolytes with Controlled Work Functions and Application to Hole Transport Layer Materials for High-Performance Organic Solar Cells. *Advanced Materials Interfaces* **2016**, *3* (12), 1500703. https://doi.org/10.1002/admi.201500703.

(104) Zhang, K.; Hu, Z.; Xu, R.; Jiang, X.-F.; Yip, H.-L.; Huang, F.; Cao, Y. High-Performance Polymer Solar Cells with Electrostatic Layer-by-Layer Self-Assembled Conjugated Polyelectrolytes as the Cathode Interlayer. *Advanced Materials* **2015**, *27* (24), 3607–3613. https://doi.org/10.1002/adma.201500972.

(105) Duan, C.; Zhang, K.; Guan, X.; Zhong, C.; Xie, H.; Huang, F.; Chen, J.; Peng, J.; Cao, Y. Conjugated Zwitterionic Polyelectrolyte-Based Interface Modification Materials for High Performance Polymer Optoelectronic Devices. *Chem. Sci.* **2013**, *4* (3), 1298–1307. https://doi.org/10.1039/C3SC22258F.

(106) Huang, F.; Wu, H.; Wang, D.; Yang, W.; Cao, Y. Novel Electroluminescent Conjugated Polyelectrolytes Based on Polyfluorene. *Chem. Mater.* **2004**, *16* (4), 708–716. https://doi.org/10.1021/cm034650o.

(107) Cutler, C. A.; Bouguettaya, M.; Kang, T.-S.; Reynolds, J. R. Alkoxysulfonate-Functionalized PEDOT Polyelectrolyte Multilayer Films: Electrochromic and Hole Transport Materials. **2005**, *38* (8), 7.

(108) Page, Z. A.; Liu, F.; Russell, T. P.; Emrick, T. Tuning the Energy Gap of Conjugated Polymer Zwitterions for Efficient Interlayers and Solar Cells. *Journal of Polymer Science Part A: Polymer Chemistry* **2015**, *53* (2), 327–336. https://doi.org/10.1002/pola.27349.

(109) Henson, Z. B.; Zhang, Y.; Nguyen, T.-Q.; Seo, J. H.; Bazan, G. C. Synthesis and Properties of Two Cationic Narrow Band Gap Conjugated Polyelectrolytes. *J. Am. Chem. Soc.* **2013**, *135* (11), 4163–4166. https://doi.org/10.1021/ja400140d.

(110) Leem, G.; Black, H. T.; Shan, B.; Bantang, J. P. O.; Meyer, T. J.; Reynolds, J. R.; Schanze, K. S. Photocathode Chromophore–Catalyst Assembly via Layer-By-Layer Deposition of a Low Band-Gap Isoindigo Conjugated Polyelectrolyte. *ACS Appl. Energy Mater.* **2018**, *1* (1), 62–67. https://doi.org/10.1021/acsaem.7b00223.

(111) Kou, C.; He, X.; Jiang, X.; Ni, Y.; Liu, L.; Huangfu, C.; Liu, K. Novel Isoindigo-Based Conjugated Polyelectrolytes: Synthesis and Fluorescence Quenching Behavior with Water-Soluble Poly(p-Phenylenevinylene)s. *Journal of Polymer Science Part A: Polymer Chemistry* **2015**, *53* (19), 2223–2237. https://doi.org/10.1002/pola.27711.

(112) Wang, E.; Ma, Z.; Zhang, Z.; Vandewal, K.; Henriksson, P.; Inganäs, O.; Zhang, F.; Andersson, M. R. An Easily Accessible Isoindigo-Based Polymer for High-Performance Polymer Solar Cells. *J. Am. Chem. Soc.* **2011**, *133* (36), 14244–14247. https://doi.org/10.1021/ja206610u.

(113) Elsawy, W.; Kang, H.; Yu, K.; Elbarbary, A.; Lee, K.; Lee, J.-S. Synthesis and Characterization of Isoindigo-Based Polymers Using CH-Arylation Polycondensation Reactions for Organic Photovoltaics. *Journal of Polymer Science Part A: Polymer Chemistry* **2014**, *52* (20), 2926–2933. https://doi.org/10.1002/pola.27328.

(114) Salvatori, P.; Mosconi, E.; Wang, E.; Andersson, M.; Muccini, M.; De Angelis, F. Computational Modeling of Isoindigo-Based Polymers Used in Organic Solar Cells. *J. Phys. Chem. C* **2013**, *117* (35), 17940–17954. https://doi.org/10.1021/jp404123x.

(115) Pho, T. V.; Zalar, P.; Garcia, A.; Nguyen, T.-Q.; Wudl, F. Electron Injection Barrier Reduction for Organic Light-Emitting Devices by Quinacridone Derivativesw. **2010**, 3.

(116) Jeon, S. J.; Han, Y. W.; Moon, D. K. Chlorine Effects of Heterocyclic Ring-Based Donor Polymer for Low-Cost and High-Performance Nonfullerene Polymer Solar Cells. *Solar RRL* **2019**, *3* (7), 1900094. https://doi.org/10.1002/solr.201900094.

Appendix

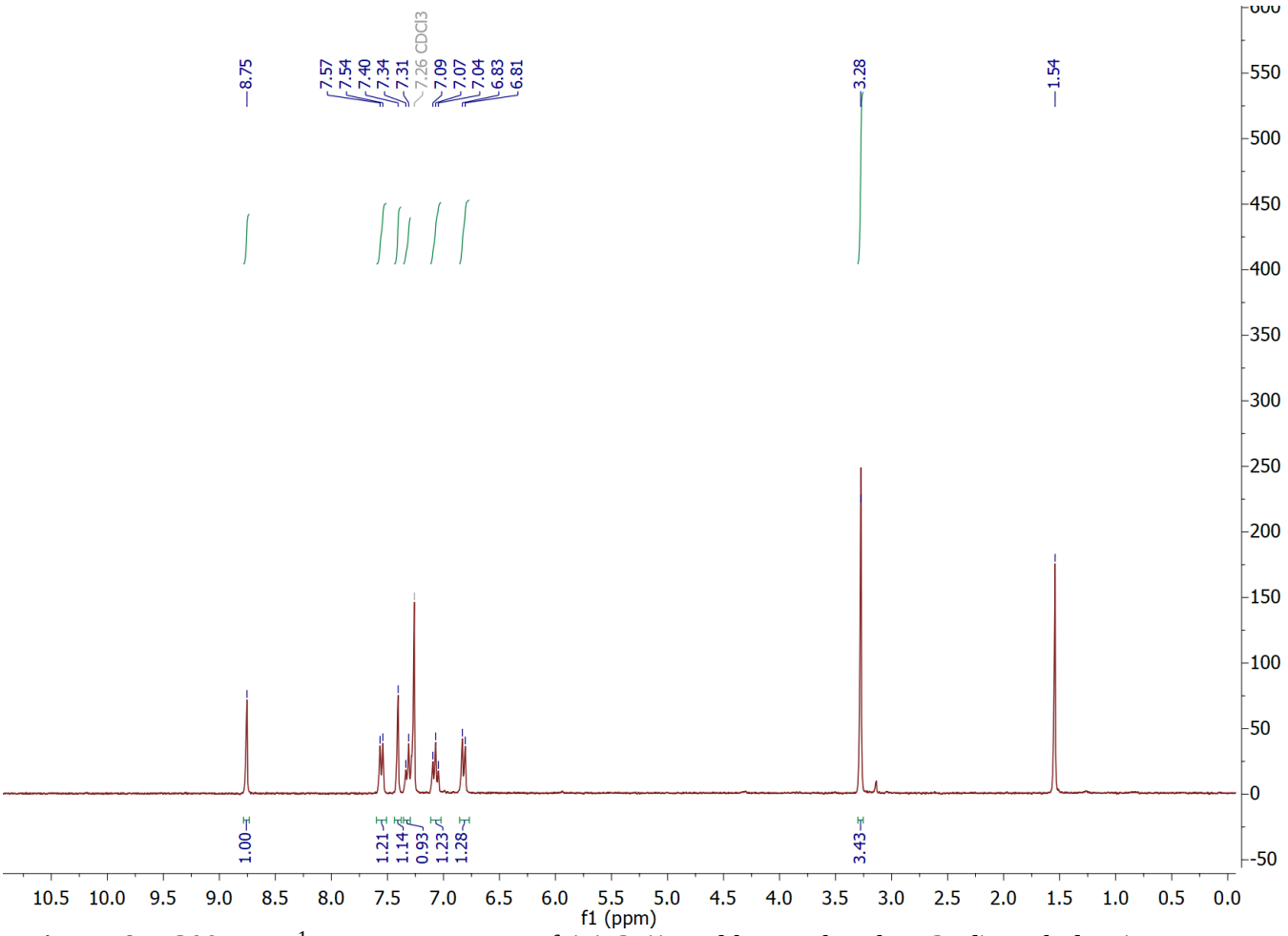

Figure A-1 300 MHz ^{1}H NMR spectrum of (Z)-3-((2,5-dibromothiophen-3-yl) methylene)-1-methylindolin-2-one in $CDCl_3$

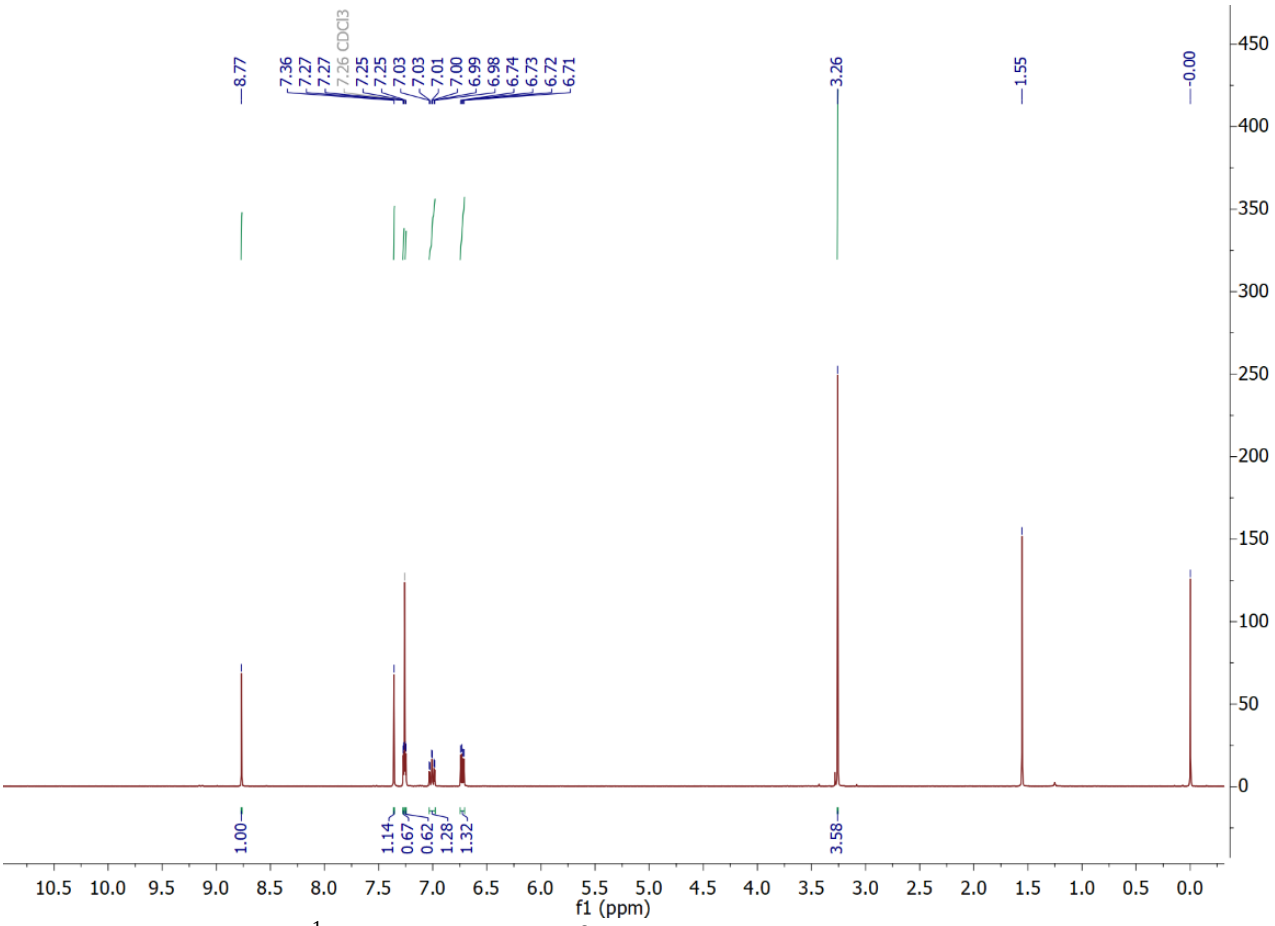

Figure A-2 300 MHz ^{1}H NMR spectrum of (Z)-3-((2,5-dibromothiophen-3-yl) methylene)-5-fluoro-1-methylindolin-2-one in CDCl3.

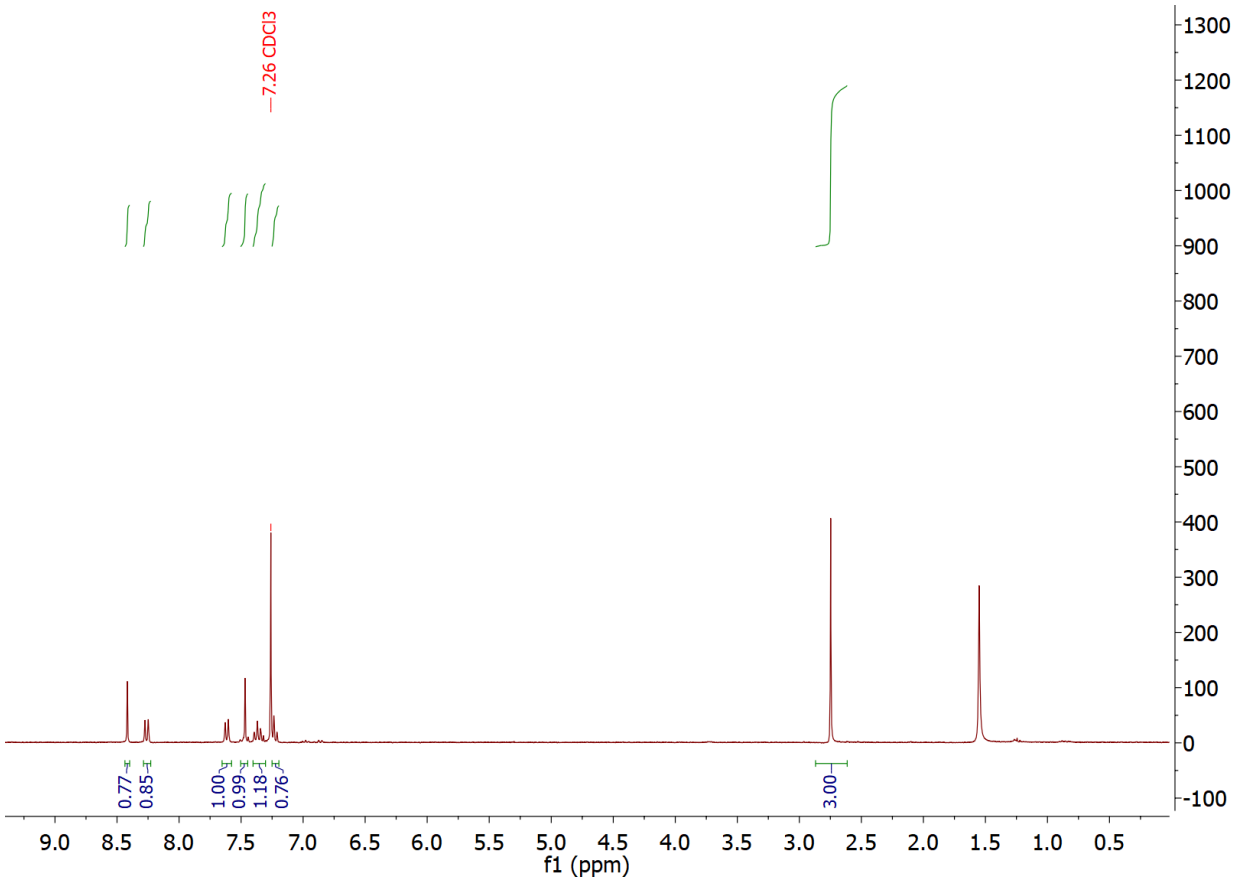

Figure A-3 300 MHz ^{1}H NMR spectrum of (Z)-1-acetyl-3-((2,5-dibromothiophen-3-yl)methylene)indolin-2-one in $CDCl_3$

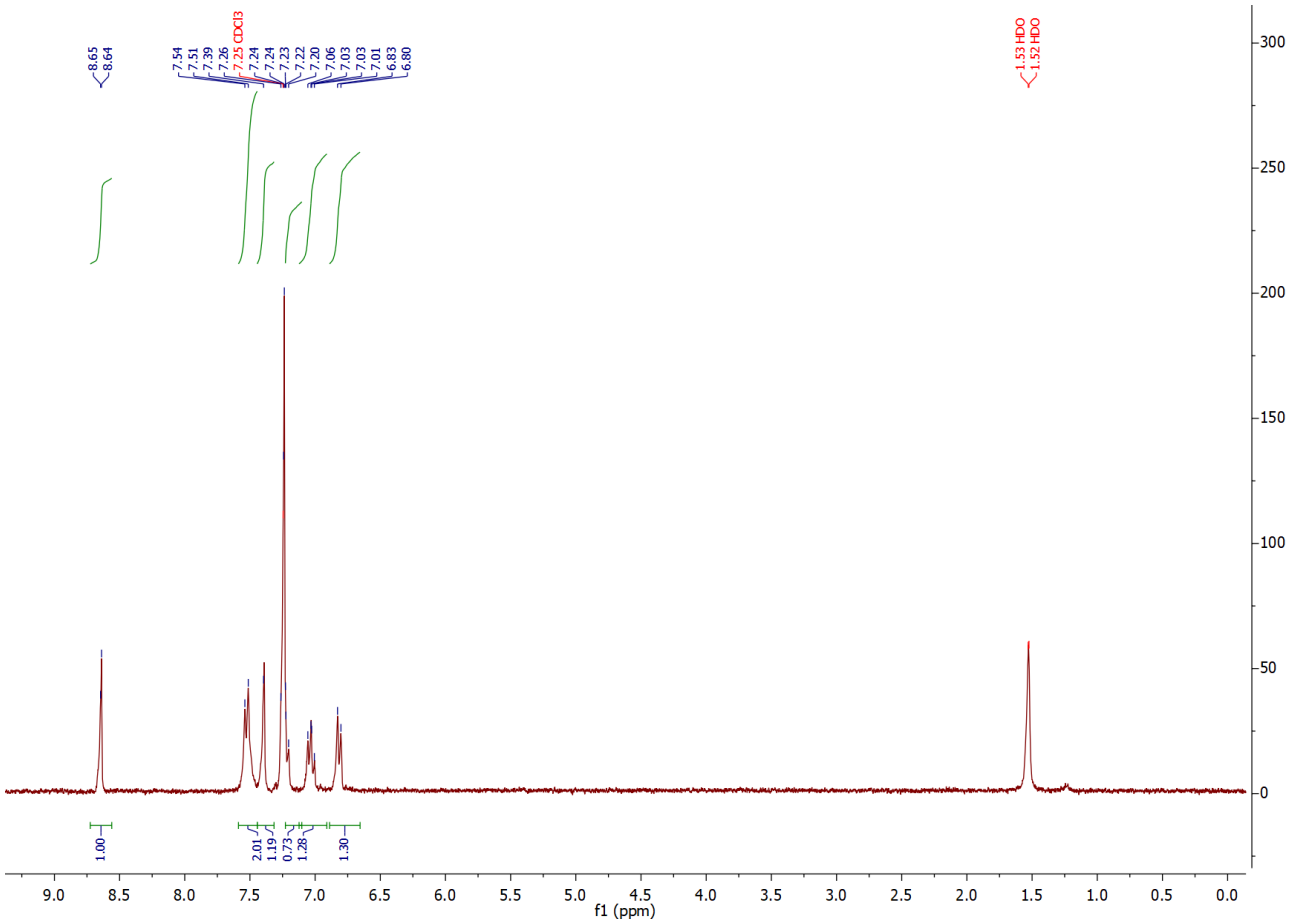

Figure A-4 300 MHz ^{1}H NMR spectrum of (Z) 3-((2,5-dibromothiophen-3-yl)methylene)-1-propionylindolin-2-one in $CDCl_3$

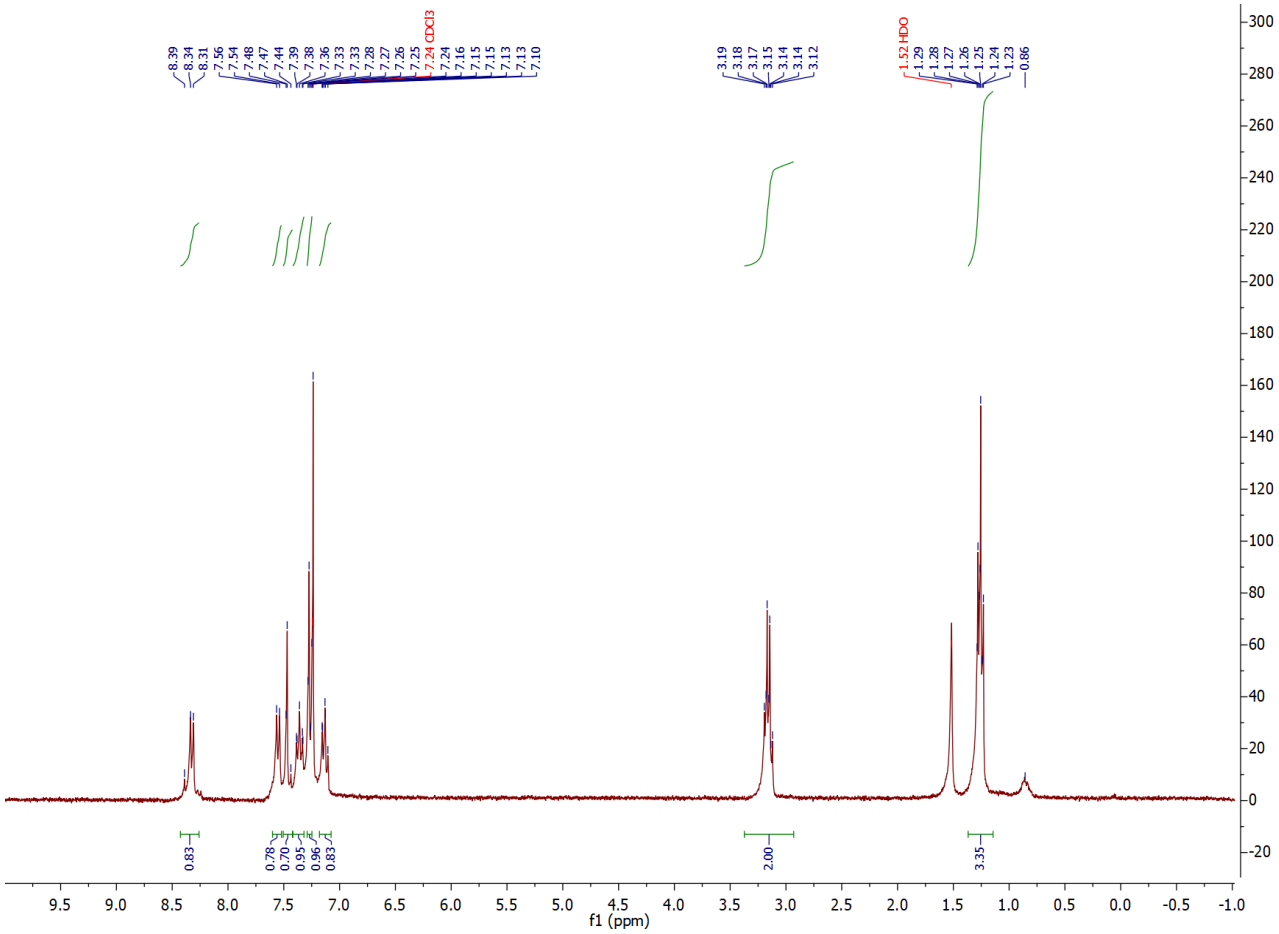

Figure A-5 300 MHz ^{1}H NMR spectrum of (E) 3-((2,5-dibromothiophen-3-yl)methylene)-1-propionylindolin-2-one $CDCl_3$

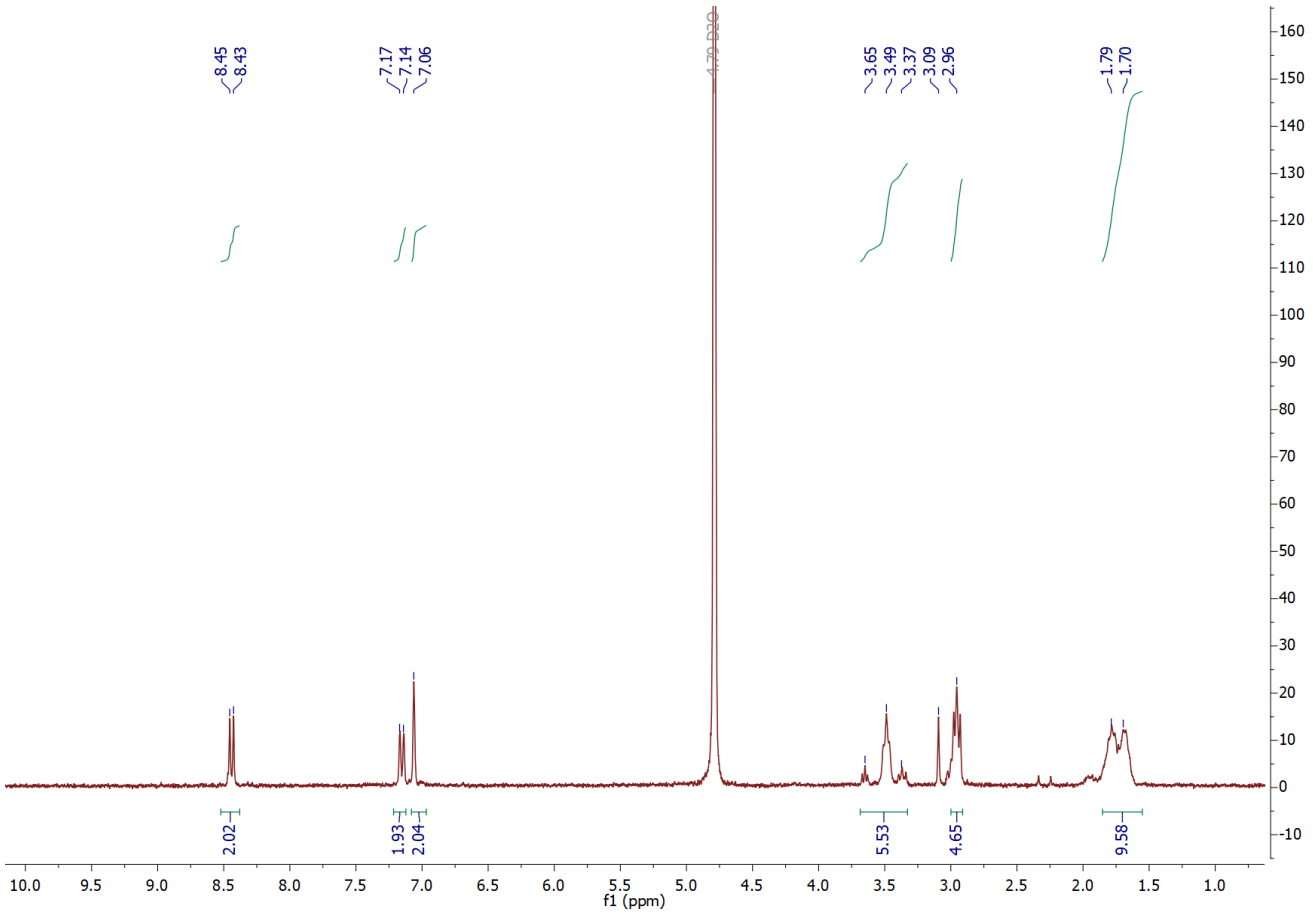

Figure A-6 300 MHz ^{1}H NMR spectrum of potassium (E)-4,4'-(6,6'-dibromo-2,2'-dioxo-[3,3'-biindolinylidene]-1,1'-diyl)bis(butane-1-sulfonate) in D_2O

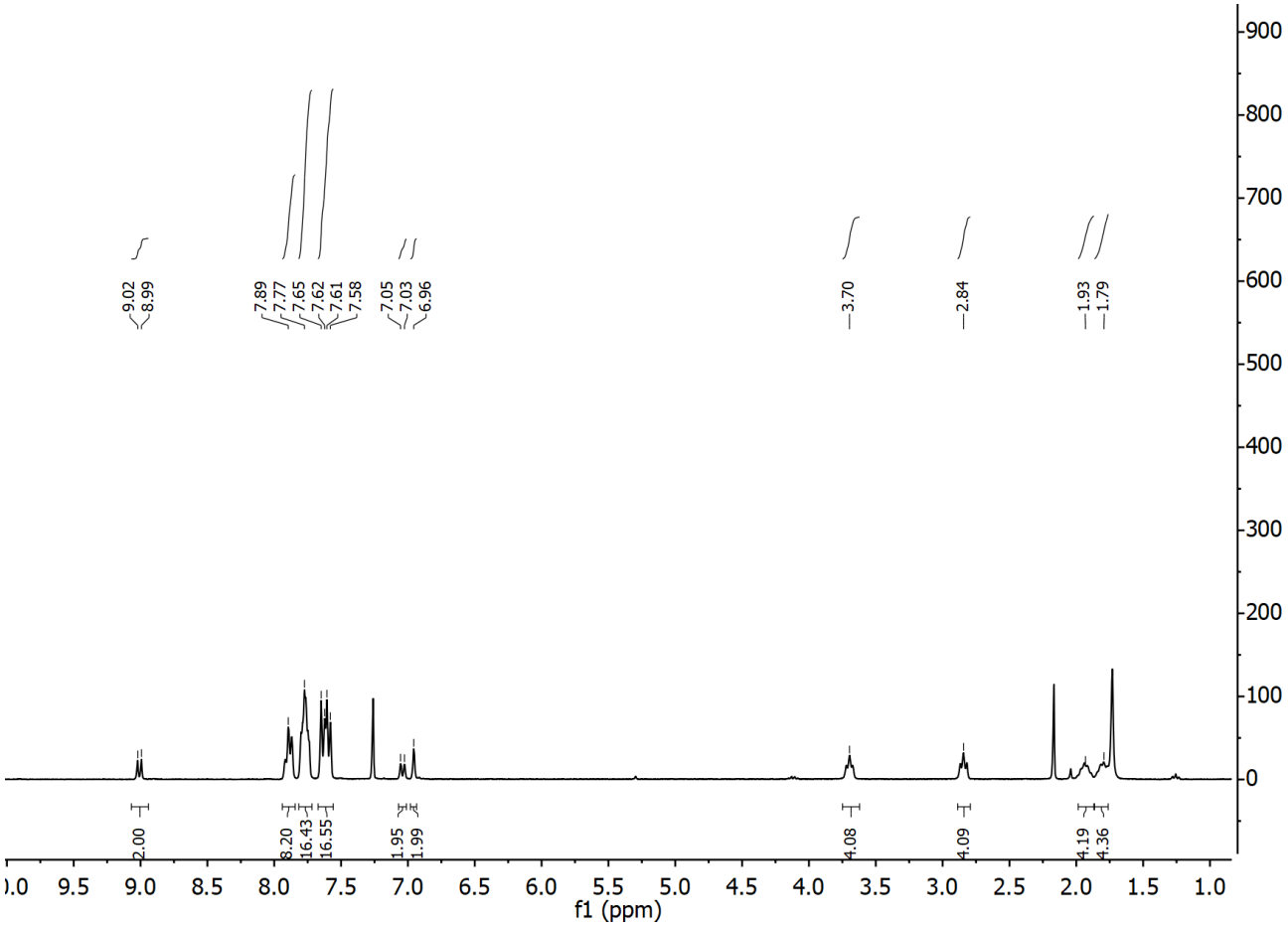

Figure A-7 300 MHz ^{1}H NMR spectrum of tetra-phenylphosphonium (E)-4,4'-(6,6'-dibromo-2,2'-dioxo-[3,3'-biindolinylidene]-1,1'-diyl)bis(butane-1-sulfonate) in $CDCl_3$